Joint Institute for Nuclear Research

FUNDAMENTAL INTERACTIONS & NEUTRONS, NUCLEAR STRUCTURE, ULTRACOLD NEUTRONS, RELATED TOPICS

XXXI International Seminar on Interaction of Neutrons with Nuclei

Dongguan, China, May 26-30, 2025

Proceedings of the Seminar

Organized by

Frank Laboratory of Neutron Physics, JINR, Dubna China Spallation Neutron Source Science Center (CSNS), China State Key Laboratory of Intense Pulsed Radiation Simulation and Effect, Northwest Institute of Nuclear Technology (NINT), China

The contributions are reproduced directly from the originals presented by the Organizing Committee.

Fundamental Interactions & Neutrons, Nuclear Structure, Ultracold Neutrons, Related Topics: Proceedings of the XXXI International Seminar on Interaction of Neutrons with Nuclei (Dongguan, China, May 26–30, 2025). — Dubna: JINR, 2025. — 92 p.

ISBN 978-5-9530-0652-1

This collection of papers reflects the present state of neutron-aided investigations of the properties of the nucleus, including fundamental symmetries, properties of the neutron itself, neutron-excited reactions, and the parameters of the nucleus that determine the reaction cross section, as well as the latest theoretical development of all these problems. The works on experimental investigations in the physics of fission by neutrons of various energies are presented in great detail. The present state of experiments on the physics of ultracold neutrons and facilities to obtain them is described at length. The status achieved by now of the latest (from the viewpoint of technique) experiments and environment studies is covered as well.

Фундаментальные взаимодействия и нейтроны, структура ядра, ультрахолодные нейтроны, связанные темы: Труды XXXI Международного семинара по взаимодействию нейтронов с ядрами (Дунгуань, Китай, 26–30 мая 2025 г.). — Лубна: ОИЯИ. 2025. — 92 с.

ISBN 978-5-9530-0652-1

В сборнике представлено современное состояние исследований свойств ядра с помощью нейтронов: фундаментальных симметрий и свойств самого нейтрона, возбуждаемых им реакций и параметров ядра, определяющих их сечения, а также последние теоретические разработки всех этих вопросов. Очень детально представлены работы по всем аспектам, связанным с экспериментальными исследованиями физики деления ядра нейтронами различных энергий. Достаточно полно описано современное состояние экспериментов по физике ультрахолодных нейтронов и установок для их получения, а также достигнутый к настоящему времени статус методически новейших экспериментов и результаты экологически исследований.

УДК 539.125.5(042) ББК 22.383.2я431+22.383.5я431+22.383.25я431

ORGANIZING COMMITTEE

Co-Chairmen

Egor Lychagin (JINR) Dongwei Hei (NINT) Sheng Wang (CSNS)

Directors of Local Organizing Committee

Walter Furman (JINR) Liang Sheng (NINT) Tianjiao Liang (CSNS)

Scientific Secretaries

Inga Zinicovscaia (JINR) Xiufeng Weng (NINT) Ruirui Fa (CSNS)

Committee Members

Yuri Kopatch (JINR) Alexander Nezvanov (JINR) Valery Shvetsov (JINR) Ludmila Mitsyna (JINR) Tatiana Pikelner (JINR) Liang Sheng (NINT) Wei Chen (NINT) Zhongming Wang (NINT) Xinjian Tan (NINT) Lei Yang (IMP) Tianjiao Liang (CSNS) Zhiming Li (NINT) Xin Tong (CSNS) Xiao Li (CSNS) Xinxin Lu (CAEP) Tao Ye (CIAE) Shilong Liu (CIAE) Xichao Ruan (CIAE) Meimei Wu (CIAE) Yuan He (IMP) Xiaohong Zhou (IMP) Sheng Wang (XJTU) Yigang Yang (THU) Liangzhi Cao (XJTU) Wenbao Jia (NUAA) Ze'en Yao (LZU) Dagian Hei (LZU) Bin Tang (ECUT) Wen Luo (USC) Guoqiang Zeng (CDUT) Jifeng Han (SCU) Jingen Chen (SINAP) Suyalatu Zhang (IMMU) Baohua Sun (BUAA) Hongwei Wang (SARI) Jianjun He (FDU) Tongpu Yu (NUDT) Wei Wang (SYSU)

Secretariat

Elena Kopach (JINR) Diana Al-Maaita (JINR) Zhanna Sorokina (JINR) Jianxin Zhang (NINT) Keqing Gao (NINT) Pengyu Sun (CSNS) Boyang Gu (CSNS) Yonghao Chen (CSNS) Wei Jiang (CSNS)

CONTENTS

Preface6
The "P olar Lights" and the Structural γ-Quanta in the Neutron Radiative Decay Experiments Khafizov R.U., Kolesnikov I.A., Nikolenko M.V., Tarnovitsky S.A., Tolokonnikov S.V.,
Torokhov V.D., Trifonov G.M., Solovei V.A., Kolkhidashvili M.R., Konorov I.V
Modeling the Neutron Whispering Gallery to Search for New Short Range Forces
Pioquinto J.A., Baeßler S., Cladé P., Nesvizhevsky V.V., Reynaud S., Schreiner K., Shi M., Voronin A.Yu., Zhao A
Investigation of the Inverse Leidenfrost Effect in the Production of Moderating Material for Cold Neutron Sources
Galushko A., <u>Litvak I.</u> , Bulavin M., Chepurchenko R35
Determination of Partial Neutron Widths of the 397.8 eV <i>p</i> -Wave Resonance of ³⁵ Cl Nucleus
<u>Kuznetsov V.L.</u> , Yergashov A., Kopatch Yu.N., Mitsyna L.V., Oprea A.I., Oprea C., Rebrova N.V., Hramko C., Sedyshev P.V.
Primary Gamma Transitions in ¹⁷⁶ Lu and ¹⁷⁷ Lu after Resonance Neutron Capture
Ahmadov G., Berikov D., Jiang W., Yang G., Furman W., Hramco C., Nuruyev S., Telezhnikov S., Madadzada A
Modelling of the Forward-Backward Effect in (n,p) Reaction with Slow and Resonance Neutrons on ³⁵ Cl
Gledenov Yu.M., Chuprakov I., Oprea A.I., Oprea C., Sansarbayar E50
Measuring the B^{nat}(n,tot) Reaction as an International Standard <i>Durán I.</i>
Assessment of Toxic Elements in Atmospheric Deposition in Azerbaijan Using Moss Biomonitoring Methods
Nuhuyeva Sh.S., Madadzada A.I., Mammadov E.A., Frontasyeva M.V64

rompt Fission Neutron Spectra and Angular Distributions Measured	
Narrow Windows of Fragment Masses and Total Kinetic Energies:	
Puzzling Result	
arjan N., Göök A., Oberstedt S	.71
pgrade Plan of Intra-Nuclear Cascade Model for ADS Simulation	
rudies	
ong Wang, Han Zhang, Han-Jie Cai, Xun-Chao Zhang, Huan Jia,	
d Yuan He	84

Preface

The annual International Seminar on Interactions of Neutrons with Nuclei (ISINN-31) was held from May 26 to 30 in Dongguan, China. This year, ISINN was jointly organized by its founder and long-term organizer – the Frank Laboratory of Neutron Physics (FLNP) of JINR, the China Spallation Neutron Source Science Center (CSNS), and State Key Laboratory of Intense Pulsed Radiation Simulation and Effect of NINT. The Seminar brought together around 230 participants from FLNP, BVLHEP, FLNR, Chinese scientific institutions, JINR member states as well as from Bangladesh, France, Japan, Iran, Spain, and USA. The scientific program of the Seminar included 117 talks and 37 posters (for more details, see https://indico.ihep.ac.cn/event/23550/timetable/#20250526).

Opening the Conference, the co-chairman of the Organizing Committee, CSNS Director Prof. Sheng Wang pointed out that he was very pleased to see the participants of ISINN-31 in Dongguan. The co-chairman of the Seminar, FLNP Director E.V. Lychagin, thanked his colleagues from China for the work done on the organization of ISINN-31 – a conference that has been gathering scientists from around the world every year for 31 years. The participants of the Seminar were greeted by the member of the Academic and Technical Committee of NINT, Prof. Quanlin Shi and the member of the Chinese Academy of Sciences Academician Huanqiao Zhang, who expressed the hope that the traditional exchange of knowledge between experienced and young researchers will continue. And the fact that the conference attracted a large number of young people means that neutron research has a future.

The first plenary sessions were opened with plenary talks by Sheng Wang "The Status of CSNS", Egor Lychagin "Experimental Infrastructure of the Frank Laboratory of Neutron Physics for Research", and invited talks by Zhigang Ge "Progress on Neutron-Induced Nuclear Fission", Hirohiko M. Shimizu "Experimental Study of Parity and Time-Reversal Symmetries in Polarized Epithermal Neutron Optics", Guohui Zhang "Recent Advances of the (n, cp) Reaction Measurements", Yuri Kopatch "Review of Recent Activities on the Tagged Neutron Method at FLNP JINR", Alexander Frank "Two-Wave Acceleration Effect and Ultra-Sensitive UCN Spectrometry", Jason Pioquinto "Modeling the Neutron Whispering Gallery to Search for New Short Range Forces", Stefan Baessler "The Neutrino Electron Correlation Coefficient in Neutron Beta Decay", Inga Zinicovscaia "Introduction to Neutron Activation Analysis at the IBR-2 Reactor, FLNP JINR", Lipeng Wang "Neutronic Characteristics of Metal Hydride Moderators and Their Applications in Microreactors", and Chao Qi "Energetic Dependence of Neutron-Induced Single Event Upsets, and Its Impact on Atmospheric Neutron SER Prediction".

The second and fourth days of the Seminar were held in the form of two parallel sessions and a joint 3-hour poster session. They covered traditional Seminar's topics: from the fundamental properties of the neutron to modern neutron sources, from promising experiments in the field of nuclear fission and nuclear reactions induced by fast neutrons to the physics of reactors and experimental methodology. As usual, investigations using nuclear and related analytical techniques in the environmental and materials sciences were widely represented.

The last day of the Seminar also included only plenary sessions with invited talks by Tianjiao Liang "Progress of DBNCT", Yuan He "Progress in Advanced Accelerator Driven Nuclear Energy System", Tongpu Yu "Laser-Driven Compact High-Flux Ultrafast Neutron Sources", German Kulin "Project of High-Brilliance UCN Source at FLNP JINR", Haitao Hu "Development of In Situ Sample Environment Technology for Neutron Scattering at CSNS",

Tianhao Wang "Setting Up High-Energy Polarized Neutron at the China Spallation Neutron Source", and Ruirui Fan "Current Status and Experiments of the Back-n White Neutron Facility". They were devoted both to problems of fundamental nuclear physics and to purely practical problems.

This year, the Organizing Committee proposed to publish the conference proceedings as original scientific papers in *Physics of Elementary Particles and Atomic Nuclei, Letters* (PEPAN Letters) and *Natural Science Review*. Therefore, only proceedings that went beyond the journals' topics or were sent directly for publishing in this book are featured in it. Nevertheless, we greatly appreciate each participant's valuable contribution to the 31st ISINN Seminar!

Co-chairman of ISINN-31 E.V. Lychagin



The «Polar Lights» and the Structural γ-Quanta in the Neutron Radiative Decay Experiments

Khafizov R.U.^a, Kolesnikov I.A.^a, Nikolenko M.V.^a, Tarnovitsky S.A.^a, Tolokonnikov S.V.^a, Torokhov V.D.^a, Trifonov G.M.^a, Solovei V.A.^a, Kolkhidashvili M.R.^a, Konorov I.V.^b

^aNRC «Kurchatov Institute», Russia ^bTechnical University of Munich, Munich, Germany

khafizov ru@nrcki.ru

Abstract. The report considers the time spectra of double and triple coincidences of the neutron radiation decay products - electron, recoil proton, and γ -ray. The peak in the spectrum of triple coincidences is used to identify radiative neutron decay events. However, there is an effect that competes with the sought-after radiative neutron decay effect, which is the emission of γ -quanta caused by β -decay electrons in the residual chamber atmosphere. This phenomenon can be observed in the form of polar lights caused also by ionization of the air at the edge of the atmosphere, the density of which is comparable to the density of the residual gas in the experimental chamber. Both radiative neutron decay and y-quanta produced by the ionization should give comparable two peaks on the spectrum of triple coincidences. However, whereas the radiative γ -quanta are formed at the moment of decay, the γ -quanta emitted by the inertial process of ionization of the rarefied atmosphere molecules should be delayed on 1 µs, which we have found on the spectrum of triple coincidences. The value of one time channel was 25 ns, which allow separating the two peaks from each other and excluding their mutual influence. This allowed us to identify radiative decay events and to measure for the first time the relative intensity of radiative neutron decay B.R.= $(3.2\pm1.6)\cdot10^{-3}$ (where C.L. = 99.7% and γ -energy more 35 KeV). But the Standard Model calculations give a one-and-a-half times smaller value B.R.= 2.1-10⁻³, thus we have registered additional γ-quanta, which are structural γ-quanta emitted by the neutron structure. It follows from the above that at registration of only double coincidences of an electron and a γ-quantum only one peak of the "polar light" will appear, and the radiative peak of triple coincidences of an electron, a y-quantum and a recoil proton will merge with fluctuations of the background since it appears only when the third particle - a recoil proton - is also registered. The spectrum of double e-y coincidences with a single "polar light" peak is presented by Byrne and others, and they positioned this peak not after but before electron registration. The authors placed peak 1 µs before the registration of the electron and are now trying to "sell" the well-studied phenomenon of ionization for quite another rare effect of the gamma radiation in the neutron decay, where structural gamma-quanta can be emitted. The placement of the peak looks extremely ridiculous because for 1µs gamma-quantum passes several hundred meters, whereas the size of their entire experimental setup is only 0.5 meters, and for this peak there is simply no room to emerge from!

Introduction

The study of neutron radiative decay is essential for the further development of the atomic project as it creates a new basis for advancing the controlled nuclear fusion. In our recent experiment to measure the relative intensity B.R. of neutron radiative decay we discovered extra gamma quanta produced during neutron decay with the bremsstrahlung gamma quanta emitted from the regular beta decay products. These extra gamma quanta are structural gamma quanta; they carry information about the quark structure of the neutron and are formed during the u and d quarks transition.

Below (see Fig. 1) follow the Feynman diagrams describing neutron decay. The first diagram describes the usual beta decay of the neutron, which produces three particles: a beta electron, a proton, and an antineutrino. This diagram describes the main mode of neutron decay. In the experiment we recorded the number of such decays by the number of double coincidences of the electron and the proton N_D. However, in any decay with the formation of charged particles there is a so-called radiative decay mode, in which, in addition to the regular decay products, an additional particle, a gamma-quantum, is recorded. This additional radiative gamma quantum is a bremsstrahlung gamma quantum emitted from a charged particle which is flying in the bremsstrahlung electric field of another charged particle. In case of neutron beta decay, bremsstrahlung gamma quanta can be emitted from proton (second diagram in Fig. 1) and beta electron (third diagram in Fig. 1). However, there is still a possibility of gamma emission, which occurs when the structure itself of the elementary particle changes. In the case of neutron decay this process is shown in the fourth diagram in Fig. 1, when gamma-quantum is emitted from the very top of the decay at the transition of u and d quarks included in the structure of neutron and proton. In the experiment, we recorded the number of radiative decay events of the neutron by triple coincidences of electron, proton, and gamma-quantum N_T.

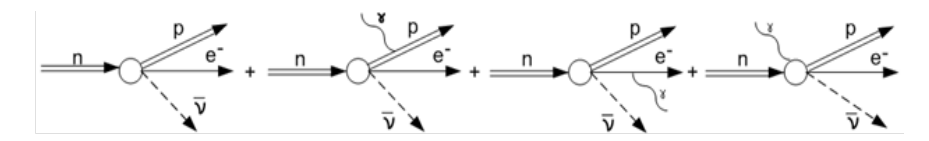


Fig. 1. The diagrams describing ordinary beta decay and neutron decay with gamma-quantum emission.

The main characteristic of elementary particle decay is its relative intensity, branching ratio (BR):

$$BR = I(radiative \ decay) \ / \ I(ordinary \ decay) = N(e,p,\gamma) \ / \ N(e,p)/k = N_T \ / \ N_D/k,$$

where the numbers of triple N_T and double N_D coincidences should be taken directly from the experimental spectra of triple and double coincidences, so that a determination BR indeed reduces to measuring the spectrum of e-p double coincidences and the spectrum of e-p- γ triple coincidences. Without performing an analysis of these spectra, it is impossible to evaluate the branching ratio BR. An additional coefficient k is the so-called geometric factor. It takes into account the geometry of the experimental facility used. The geometric factor k is determined

by means of a Monte Carlo simulation of the experiment using the package of CERN programs GEANT IV.

Until recently, the rare radiative mode of neutron decay was not discovered and was considered only theoretically [1–4]. Our first attempt at detecting events of radiative neutron decay was undertaken at the Institut Laue-Langevine (ILL) in employing an intense coldneutron beam [5]. The experiment that our group performed in 2005 at the FRMII reactor of the Technische Universität München became the first experiment that resulted in observing this process [6]. We were the first to identify events of radiative neutron decay by means of triple coincidences in which an emitted gamma-quantum was recorded as a third particle in addition to the electron and recoil proton. Thus, we were able to measure the branching ratio for the radiative mode of neutron decay. The result was BR = $(3.2\pm1.6)\cdot10^{-3}$ at a coincidence level of C.L.= 99.7%, the gamma energy being in excess of 35 keV. In the experiments performed earlier at ILL [6] our group was able to measure only the upper limit on this branching ratio. A year later, a group of experimentalists from the National Institute of Standards and Technology (NIST) published in Nature the results of their experiment devoted to studying radiative neutron decay [7]. Their result was BR = $(3.13\pm0.34)\cdot10^{-3}$ at C.L. = 68%, the gamma energy there ranging between 15 and 340 keV. However, there were no triple coincidences in this experiment but only the spectra of double coincidences of electron gamma-quantum and electron - ion. Obviously, without registering exactly the triple coincidence of electron, gamma-quantum, and proton, it is impossible to talk about registering the events of neutron radiative decay. Such double coincidences occur during the well-studied process of ordinary ionization of the residual gas by electrons in the chamber, as a result of which a glow appears. For example, in nature such a phenomenon is observed as the polar lights at the edge of the atmosphere. The authors of this [7] and later work [8] recorded this radiation of gamma quanta in the hard and invisible area of the spectrum, they had created the ideal conditions for this. There, as will be shown below, was a strong magnetic field, and highly rarefied residual air in the chamber, and ionizing particles (beta-electrons). In addition, the authors of this work recorded ions instead of protons, because due to the strong magnetic field they were not able to distinguish protons and the large ionic background occurring in the experimental facility. Thus, the BR value given by the authors of [7] is the ratio of the intensity of gamma emission during the ionization of rarefied air molecules to the total number of ionization acts by beta-electrons.

Experimental facility

The layout of the proposed experimental facility is shown in Fig. 2. Passing along a rather long neutron guide equipped with a collimating system formed by LiF diaphragms, an intense beam of cold neutrons enters a vacuum chamber (1) through the last LiF diaphragms (9) positioned immediately in front of the decay zone being studied. The decay zone is viewed by detectors of three types simultaneously. These are a proton detector (3) formed by microchannel plates (MCP), an electron detector (13) formed by photomultiplier tubes 7 cm in diameter covered with a scintillator plastic 3 mm thick, and six gamma detectors (11). These six detectors surround the electron detector (see the lower panel in Fig. 2) at an angle of 35° and are formed by photomultiplier tubes covered with a sensitive CsI layer. The layer thickness is 4 mm. It is chosen in such a way that the gamma-quantum detection efficiency is equal to unity. Six gamma detectors (11) surround the electron detector (13) (see the lower panel in Fig. 2) are arranged at an angle of 35° and are protected by a cup (12) made of 6-mm lead. In principle, coincidences between the electron detector and any of the six gamma

detectors can completely suppress the background of bremsstrahlung, which arises only in that section where electrons are detected. From Fig. 2, it can be seen that, in this case, part of the data is lost. However, the neutron-beam intensity of 10^{12} n/c/cm² in our chamber is quite sufficient in order to compensate for this loss and to retain an acceptable data-accumulation rate. Recoil protons produced in the decay zone travel through the space surrounded by a cylindrical time-of-flight electrode (7) toward the proton detector (3). After that, they are focused on this detector by means of spherical focusing electrodes (2). The focusing electrostatic field is generated between high-voltage spherical (2) and cylindrical (7) electrodes and grids (6 and 5), on one hand, and the underground proton-detector grid (4), on the other hand. It is noteworthy that recoil protons fly isotropically out of the decay vertex. An additional grid (10) is positioned on the opposite side of the decay zone in order to avoid the loss of protons that go toward the electron detector.

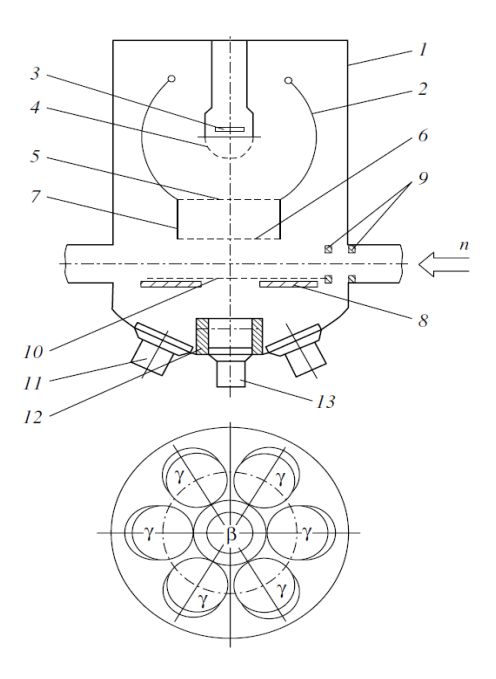


Fig. 2. Layout of the experimental facility: (1) vacuum chamber, (2) high-voltage (18 to 20 kV) spherical electrodes for focusing recoil protons, (3) proton detector, (4) grid of the proton detector (underground), (5, 6) grids of the time-of-flight electrodes, (7) time-of-flight backward direction (at a voltage of 22 to 26 kV), (11) six photomultiplier tubes for CsI(Tl) gamma detectors, (12) lead cup, and (13) photomultiplier tube equipped with a plastic scintillator for detecting electrons.

A signal from an electron detected in the scintillator plastic of the electron detector (13) serves a start signal that opens all time windows for all detectors. A pulse from one of the gamma detectors (11) is recorded simultaneously with this signal, but only in the case where a signal from the proton detector (3) is generated within a reasonably short time interval will this electron- gamma-quantum coincidence be recorded by an electronic system for data acquisition and data processing as an event of radiative neutron decay. Along with these triple coincidences, our electronic system records ordinary electron-proton coincidences. It should be noted that, in the case of radiative decay, the emitted gamma-quantum is detected in our facility by the gamma detectors (11), which are placed around the electron detector (13), earlier than the electron is detected by the electron detector (13). In other words, the electron should be delayed with respect to the emitted gamma-quantum in the time spectrum of triple coincidences but by an extremely small amount, e.g., a nanosecond. It is precisely this fact that will enable us to identify the peak associated with radiative gamma quanta in the spectrum of triple coincidences. In addition to triple coincidences, our setup also collects double coincidences corresponding to ordinary neutron decay. Here, it is worth noting that a very high quality of the system of diaphragms from LiF ceramics is necessary to obtain an acceptable low level of the background in gamma quanta from an intense cold-neutron beam while passing this beam through the whole facility from the entrance window to the thick LiF ceramic target absorbing it. The entrance window and the absorbing target are the main sources of gamma background in the facility, therefore the neutron guide must be long enough and its axis must coincide with the beam axis as precisely as possible. In our case, the entrance window for the beam was at a distance of 7 meters from the area viewed by the detectors, and the absorbing target was 3 meters. In the next section we will use the time spectra of double and triple coincidences to obtain the experimental value of the main characteristic of the radiative neutron decay (BR).

Let us now consider the flowchart of our electronic system for collecting and processing information obtained from detectors of three types - electron detector, proton detector and gamma-ray detector. The flowchart is given in Fig. 3. The signal coming from the electron detector opens time windows 150 channels forward and 100 channels backwards; the scale division value of each channel is 25 nanoseconds. Then the electron-proton double coincidences scheme receives a signal from the proton detector into the corresponding channel opened by a signal from the electronic window detector. As a result, firstly, the spectrum of double time coincidences is formed, and secondly, the windows of double coincidences are selected and fed to the triple coincidences scheme. It should be noted here that the proton detector registers not only protons from beta decay proper but also a great number of ions formed in the experimental chamber and captured by the electrostatic field of the focusing electrodes. As a result, the beta-decaying proton peak must be observed on a significant ion background forming a horizontal substrate under this peak. The height of this substrate is comparable to the height of the proton peak itself. In addition, a high and narrow electron registration response peak should form in the starting channel on the triple coincidences spectrum; the nature of this peak is not physical and is related to the electronic scheme of the double coincidences. Thus, the double coincidences spectrum is a horizontal substrate of background ions with two peaks; the electron registration response peak and the beta decay peak consisting of neutron beta decay protons. The triple coincidences scheme is then fed with signals from six gamma detectors, which in turn are registered in their channels in the time windows selected by the double coincidences scheme, open for 150 channels forward and 100 channels backwards. As a result, a spectrum of triple coincidences is formed where the gamma background is even more significant in its magnitude than the ion

background. Due to this uncorrelated background, all the peaks that are observed in the double coincidences spectrum will be displayed, and these two peaks, the electron registration response peak and the beta decay peak, will appear in the triple coincidences spectrum.

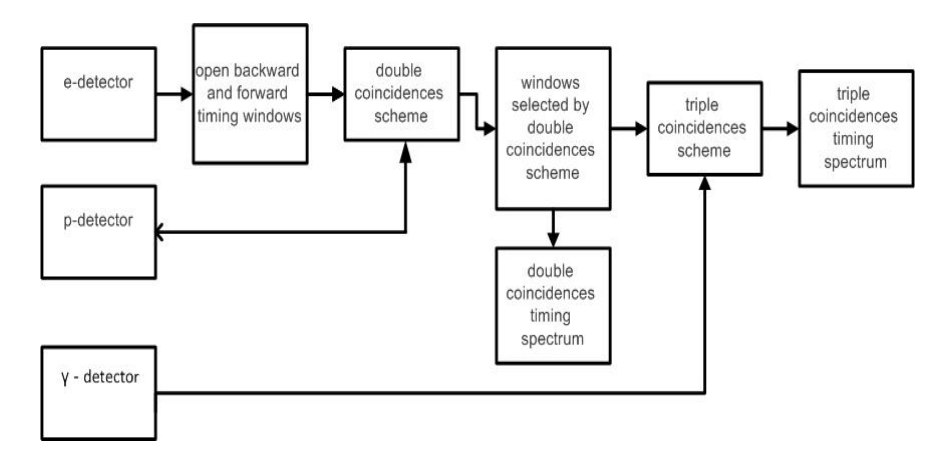


Fig. 3. Flowchart of the electronic system of information collection and processing.

Besides, additional peaks from the electron-gamma coincidence spectrum will be added to these two peaks. There are also two such peaks and both of them have a physical nature. The first narrow peak is the peak of radiation gamma quanta, it should be located to the left of all other peaks because radiation gamma quanta are registered before all other particles. The second broad peak comes with a delay of 1 µs and it is formed by gamma quanta from ionising radiation caused by beta-electrons. It is to be noted that there is residual air in the experimental chamber, the density of which is comparable to the air density at the edge of the earth's atmosphere, where the well-known aurora borealis occurs. Thus, the radiation peak will be observed against an inhomogeneous background in which, in addition to the horizontal substrate, there are three peaks: the peak response to electron registration, the response to the beta decay peak, and the response to the broad peak of the "aurora borealis". In this case, the radiation peak should be located the very first, which is what we observed in the experiment. Looking ahead, we will say that on the real spectrum in channel 116, we observed one more peak, the nature of which is purely electronic, it has nothing to do with physics. The point is that gamma signals have very long "tails", which were "cut off" by the electronic system to reduce the load on them. Below we will consider in detail the obtained spectra of double and triple coincidences.

Timing spectra of double and triple coincidences

Here we will analyze the spectra of double coincidences between beta-electron and proton, and also the spectra of triple coincidences between beta-electron, proton and gamma-quantum. We will compare our results with the results obtained by two other groups from NIST.

Fig.4 demonstrates the summary statistics on double e-p coincidences (coincidences of a light beta-electron moving at a speed comparable to the speed of light and a delayed heavy proton, whose speed is much lower and is determined by the potential of the accelerating electrostatic field). Therefore, Fig.4 clearly shows two major peaks: one peak with a maximum in channels 99-100, which is the response to electron registration by the electronic registration and recording system [5, 6] of the experimental facility. The position of this peak determines the arrival time of the signal from the electron detector, which consists of PMTs and is coated with scintillation plastic. This peak is not physics-related in its nature. Instead, it is a response to the registration of the electron. As soon as the electronic system registers an electron, it opens a time window of one hundred channels forward and backward in time. Thus, the 100th channel is the master channel, and each channel corresponds to 25 nanoseconds, so the spectra can view all events in 2.5 µs before and after the arrival of the electron. The next peak visible in Fig. 4 has a maximum in channel 120, it is physics-related in its nature and is a proton peak, i.e. the peak of e-p coincidences of beta-electron with delayed proton. Its position determines the time of proton registration by the electronic system, and the distance between these two peaks determines the proton delay time.

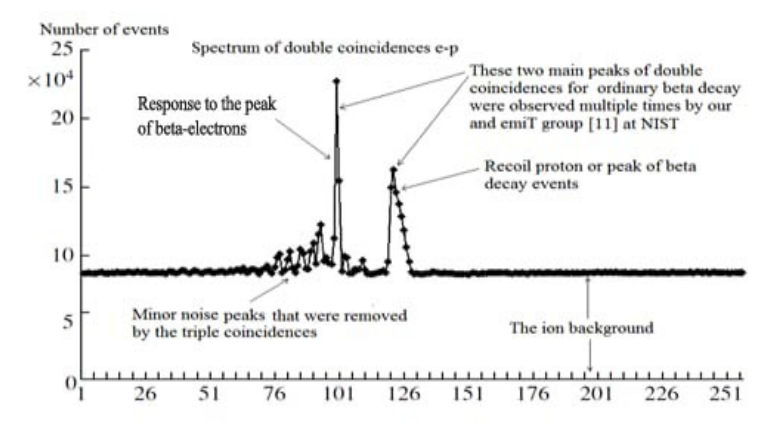


Fig. 4. Timing spectrum for e-p coincidences. Each channel corresponds to 25 ns. The peak at channels 99-100 corresponds to electron registration by the electronic system. The coincidences between the decay electrons and delayed protons (e-p coincidences) are contained in the wide peak centered at channel 120.

An analogous situation was first noted in [9], then it was observed during the experiment on the measurement of the correlation coefficients by the group at ILL [5, 10] and emiT group at NIST [11], and it was also mentioned at [12]. We would especially like to emphasize the correspondence of our spectrum of double coincidences with an analogous spectrum from the result obtained by the emiT group from NIST [11]. In Fig. 5 we present their spectrum and diagram for the registration of the beta electron and the recoil proton. A comparison of our results with the results of the emiT group shows their unquestionable similarity. Moreover, the position of the second proton peak in Fig. 4 (emiT group), like in

Fig. 3 (our result), corresponds well to the simple estimate obtained by dividing the length of a proton trajectory by its average speed.

Here we will also note the presence of a significant homogenous ionic background in Figs.4 and 5. However, in both cases this background allows to easily distinguish the neutron decay peak, and, thus, we can easily determine the number of N_D double coincidence events, i.e. the number of registered neutron beta decays. Note the most important point in the methodology of the experiment: this large ionic background cannot be distinguished from the small number of neutron decay protons (i.e. from beta decay events) in the presence of strong magnetic fields, and thus N_D cannot be determined

Following Avogadro's law, even in the case of a very deep vacuum under pressure of $10^{-6} - 10^{-8}$ mbar air molecule concentration remains very high. In fact, it is sufficient for betaelectrons produced in neutron decay to create a significantly high ionic background in the chamber, exceeding the number of decay protons by many orders of magnitude. These ions create a homogeneous background in the absence of strong magnetic fields, throughout the whole spectrum of double coincidences. It should also be noted that the concentration of ions in the chamber does not fall in proportion to the pressure, but much more gradually, as the cubic root of the pressure. Here one must note that the probability of ion creation along the trajectory of beta-electron is in inverse proportion to the average distance between neighboring ions, i.e. is proportional not to the molecule concentration but to the cubic root of this value. This fact means that the ionic background remains significant even when the pressure is reduced by a factor of 100, which is observed when comparing our results with those of the emiT group. The emiT group's vacuum was two orders of magnitude greater, but the ionic background dropped only 4-6 times compared to ours. This estimate is confirmed when one compares the spectra in Figs. 3 and 4. Our spectrum, presented in Fig.3, has a 1:1 ratio of the value of e-p coincidences peak and the value of the background. The emiT group (Fig.4) spectrum has a ratio of 4:1-5:1, i.e. only 4-5 times our number, that is equal to the cubic root of 100.

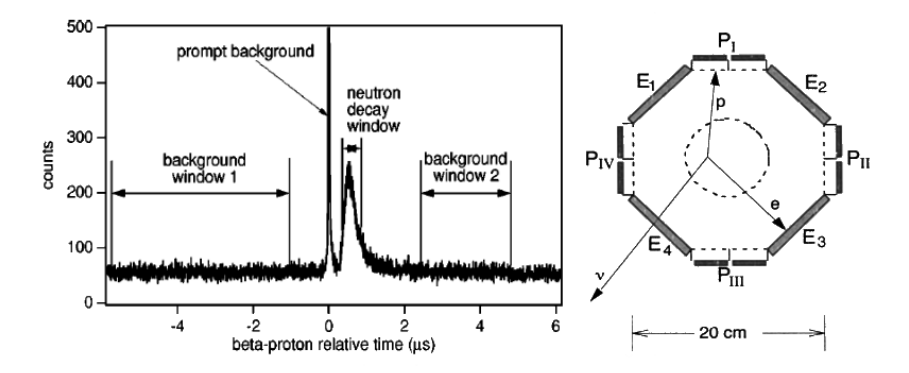


Fig. 5. On the left: spectrum of double electron-proton coincidences obtained by emiT Group [11] with two peaks and a significant ion background value comparable to the neutron decay peak; on the right: emiT group scheme for registering beta electron and recoil proton.

Fig.4 shows that the total number of events in e-p coincidences peak in our experiment equals N_D =3.75·10⁵. This value significantly exceeds the value we obtained in our previous experiment conducted in ILL. At that time, due to the low statistics volume we could not identify the B.R. itself and instead defined only the upper B.R. limit [5]. So, in both cases Figs. 4 and 5 show not one but two peaks above the homogeneous ionic background.

The remaining peaks in Fig. 4 are small, with just seven peaks distinct from the statistical fluctuations. These occurred because of the noise in the electric circuits of the FRMII neutron guide hall. There are no other physics-related reasons for their occurrence. The fact is that our experiment was the first at the newly opened FRMII reactor, and the neutron guide hall was still undergoing intensive commissioning work. These peaks were appearing during the working days and disappearing over the weekends. Such behavior was observed as we collected statistics.

Now we will compare our results and the results obtained by the emiT group with the third result, that is the spectrum of double coincidences obtained by another NIST group [12]. Unfortunately, the authors did not publish the spectrum of double coincidences in their original article [7], but published it much later [12]. Fig. 6 displays the spectrum on the left and the diagram of NIST experimental facility on the right. Fig. 6 clearly shows one single and a very wide peak with a long tail, which has nothing in common with either our peak or the emiT group peak.

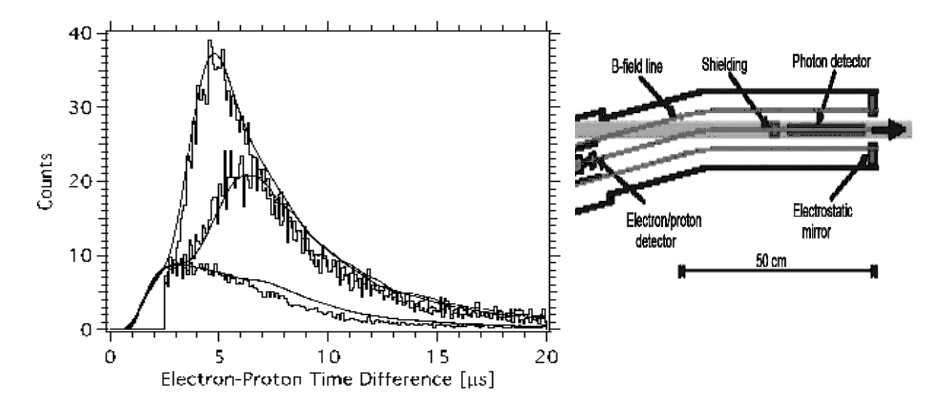


Fig. 6. On the right: the facility diagram. On the left: spectrum of double coincidences published in [12]. The lower curve corresponds to 0 volts, the middle curve corresponds to 300 volts and the highest curve corresponds to 500 volts in an electrostatic mirror. The location of the peak and its width differ from our and the emiT's results by one and two orders of magnitude. The location and the width of the peak also deviate by one and two orders of magnitude from the elementary estimates of the proton decay delay times.

The significant deviation obtained is explained by the fact that the peak in the NIST experiment consists not of protons but rather of ions. The density of gas molecules inside the experimental chamber is proportional to pressure and according to the Avogadro's Law is of the order 10^7 mol/cm³ even at the pressure of 10^{-8} – 10^{-9} mbar. This is a very significant number, quite sufficient for creation of the large ionic background in the presence of ionizing

radiation created in the chamber by beta-electrons of neutron decay. The energy of betaelectrons significantly exceeds the energy of ionization. Besides, as mentioned above, the probability of ionization is inverse proportional not to volume taken up by one molecule but to the average distance between molecules. It is precisely due to this reason that the ionic background falls much more gradually, proportionally to the cubic root of the pressure and not proportionally to the pressure. We observed a similar behavior of the ion background many times during our experiment; roughly speaking, if the pressure in the chamber dropped by an order of magnitude, the background decreased by only a factor of two or more. As mentioned above, comparing our results with those of the emiT group gives a drop in the ionic background of only 4-5 times, not two orders of magnitude. In the emiT group experiment the conditions were the same as in the second NIST group experiment, therefore the ionic background should be the same too. The light ions, together with the beta decay protons, should have a delay time comparable to 1 µs. The pulses from these particles are simply not visible in the spectrum due to the second NIST group's use of combined electronproton detector in order to register both electrons and protons with ions. Figure 6 shows a huge pulse from an electron, which simply "blinds" the detector for the time the small pulse from the proton and light ions arrives. The maximum of the ion peak in this group experiment, according to the delay times estimations (delay time is proportional to square root of ion mass), falls exactly to the 4-6 µs on the air ions consisting of nitrogen and oxygen.

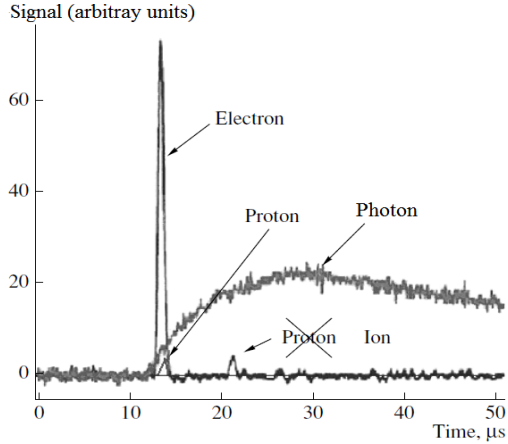


Fig. 7. The signal from the proton has to be delayed by less than one microsecond, which is why it is located at the base of the strong electron signal and so cannot be registered by the combined electron-proton detector. The pulses that are delayed by longer than 1 microsecond are pulses not from protons, as it was indicated in ref. [7], but rather from ions, formed in the viewed decay zone. A pulse from a photon has a front of about 15 μs.

Fig. 7 presents the pulse forms from the electron, ion, and gamma-quantum published by the second experimental group from NIST [7]. Firstly we should note the exceptionally long and flat front from the gamma pulse of $15~\mu s$, which arises because of the extremely slow detectors on avalanche diodes. The authors used them because they used strong

magnetic fields of several tesla, in which fast PECs do not work. As was pointed out above, a strong pulse from an electron makes weak pulses from ions and protons invisible during the first microseconds after its arrival. Namely this fact explains the dead zone around zero of the diagram in Fig. 6 which is where the pulses from the decay protons should come.

Let us now proceed to analysing of our triple coincidences spectra presented in Fig.7. As it was mentioned above, both double coincidences spectra obtained by our (Fig.4) and the emiT (Fig. 5) groups present two main peaks located on the horizontal ionic background. As for the spectrum of triple coincidences, we should observe not two but three peaks: one radiative peak and two peaks similar to the ones in the double coincidence diagram. Let us review this similarity in more detail: the peaks on the spectrum of double coincidences are as if transferred to the spectrum of triple coincidences.

We have two channels carrying background noise with some average signal frequency f_1 and f_2 . Then the probabilities for the signal hitting the time window of value T are equal for both channels $p_1 = f_1 T$ and $p_2 = f_2 T$ respectively. If we now apply the electronic coincidence scheme, then the probability of random coincidence p_c of signals on the first and second channel in the coincidence scheme with the same value of time window T is equal to product of two independent events probabilities $p_c = p_1 p_2 = f_1 T f_2 T$ and frequency of coincidence respectively is equal to $f_c = f_1 f_2 T$. Suppose now on the first channel there is not a homogeneous horizontal background of pulses with mean frequency f_1 , but some input spectrum with its peaks S_{in} – then after the coincidence scheme an output spectrum proportional to the input $S_{out} = S_{in} f_2 T$ with a ratio $f_2 T$ appears, note that the higher the homogeneous background on the second channel f_2 , the more frequent the coincidence and the higher this ratio. Thus, all the peaks in the input spectrum also appear in the output spectrum from the coincidence scheme.

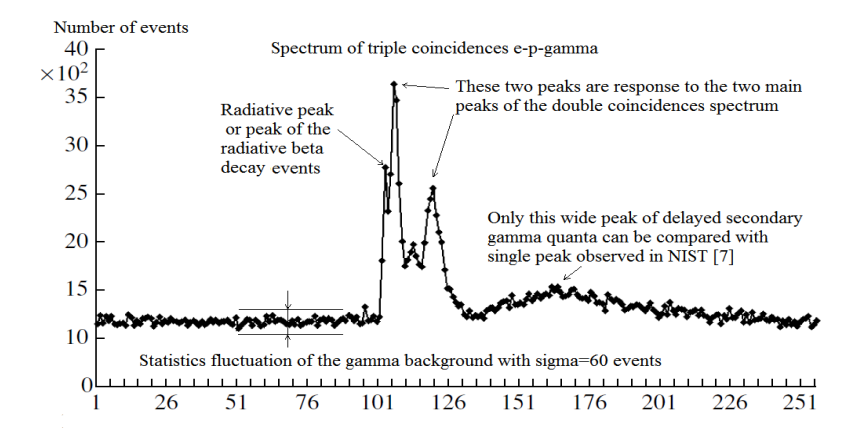


Fig. 8. Timing spectrum for triple e-p-γ coincidences. Each channel corresponds to 25 ns. In this spectrum, three main peaks in channels 103, 106 and 120 can be distinguished. The leftmost peak in 103 channel among these three main peaks is connected with the peak of radiative decay events.

However, simply multiplying the input spectrum by number changes the height of the peak only, but both its width and its position remain unchanged. The real electronic coincidence circuit with the detector unit also makes hardware changes to the shape of the spectrum itself. Let us review these changes in more detail on our triple coincidence spectrum shown in Figure 8. The figure shows three peaks: the leftmost peak of triple coincidences located in channel 103, which consists of the supposed number of neutron radiative decay events we measure; two peaks from the input spectrum of double coincidences. These are the response peaks to the registration peak of electrons and delayed protons, respectively, but both response peaks on the spectrum of triple coincidences are significantly wider and located closer to each other than in the original spectrum of double coincidences (Fig. 4). These two wide peaks in channels 106 and 120 converge so that there is a rather high jumper between them. In addition, there is a small parasitic electron peak, the nature of which is related to the electronic circuitry of the registration of gamma-quantum pulses.

Such distortions of the output spectrum are controlled by a standard procedure, introducing a response function for gamma channel $R_{\gamma}(t,t')$ [6], which is also necessary for calculating the number of triple coincidences N_T in radiative peak:

$$S_{out}(t) = \int S_{in}(t')R_{\nu}(t,t')dt'$$
.

This functional multiplication instead of simple multiplication of the input spectrum by a number takes into account all the distortions of the real spectrum. Namely, the response function method is able to consider both the change of the peak width and the convergence of two response peaks located around channels 106 and 120. In a particular case, if we use the local response function with zero width as a δ -function with some coefficient, it becomes a simple multiplication of the input spectrum by the number mentioned above. If we use the non-local response function then its width will lead to an increase in the widths of the response peaks, roughly speaking, by the width of the response function, and its tails will lead to a convergence of the peaks in the output spectrum compared to the original spectrum. This is exactly the picture we observe when comparing our double and triple coincidence spectra in Figs. 4 and 8. Thus, using the method of nonlocal response function we can distinguish the peak of radiative gammas on inhomogeneous double-humped background.

As for the wide peak in channel 165, it has a physical nature, has nothing in common with the peak of radiative decay and is well distinguished from it delaying at a considerable distance of 1 µs from it. This peak is created by the radioactive gamma quanta and emitted during ionization of rare atmosphere within our experimental chamber. The molecular of this medium is ionized by registered beta-electrons. This event is well studied and does not have anything in common with the new event of radiative neutron decay but happens due to the ionization of highly rarefied air by charged particles. It is this phenomenon that was observed by the second NIST group, who published a single peak shown in Fig. 9 (see [7]). Let us note that the spectrum published by these authors is not a spectrum of triple coincidences; otherwise, as mentioned above, it would have had additional response peaks from the spectrum of double coincidences of the electron with the recoil proton, or, as in their case, with the ions. In fact, this experiment used everything needed to investigate the phenomenon known as polar lights. Firstly, it is the residual rarefied air, whose density just corresponds to the density of air at heights of 150-200 km, where natural polar lights occur; secondly, it is the presence of ionizing radiation in the form of beta electrons, flying from an intense beam of cold neutrons; and thirdly, it is the presence of magnetic fields. Thus, the authors of this experiment measured the relative intensity as the ratio of gamma-quanta produced by the

ionization of air molecules to the total number of ions flying out of the same viewed decay zone under the influence of the electrostatic field. This ratio is also proportional to the fine structure constant $\alpha = 1/137$ and thus has the same order of magnitude as the BR in the case of neutron radiative decay.

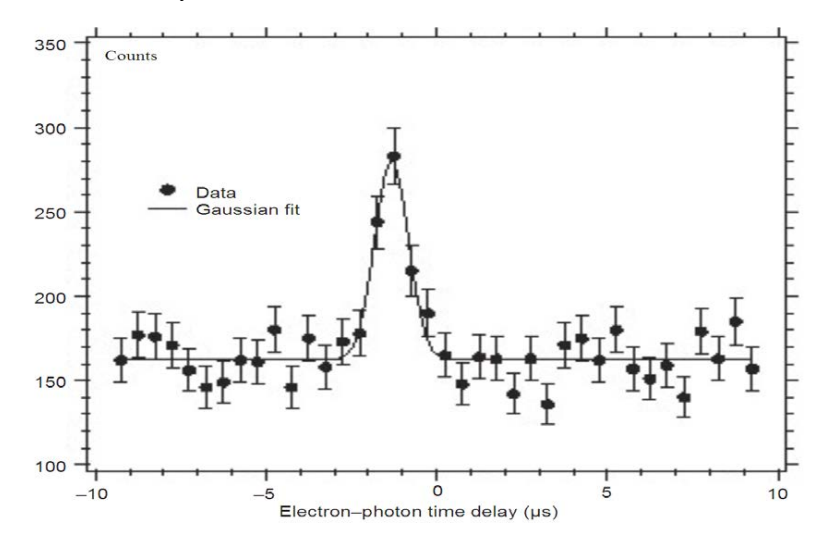


Fig. 9. The single peak of "electron-photon" coincidences, shifted to the left of 0 – the time of electron registration – by 1 μ s, published in [7, 8]. On the spectrum of triple coincidences (see Fig. 8) in our experiment a similar wide peak is located after the electron registration and there are no wide peaks before the beta-electron registration.

After analysis of triple coincidences spectra with the help of the non-local response function $R_{\gamma}(t,t')$ we finalize the number of radiative neutron decays N_T =360 with a statistics fluctuation of 60 events. B.R. can be expressed as a ratio of N_T to N_D as BR = N_T / N_D /k, where coefficient k=0.3 is the geometrical factor that we can calculate by using geometry of the facility as well as anisotropic emission of radiative gamma-quanta during neutron decay [4]. With the number of observed double e-p coincidences N_D = 3.75·10⁵ and triple e-p- γ coincidences N_T = 360, one can deduce the value for the main characteristics of neutron decay, branching ratio B.R.= $(3.2 \pm 1.6) \cdot 10^{-3}$ (99.7 % C.L.) with the threshold gamma energy ω =35 keV. In this case we chose C.L.= 99.7%, which corresponds to an error of 3 σ , and the resulting error was 50% of the mean B.R. If, however, we choose the standard confidence limit C.L.= 68% with an error of 1 σ , the error is only 15% of the mean value. On the other hand, this experimental mean of B.R. = 3.2 is 1.5 times higher than that calculated by the standard model of electroweak interaction. This means that approximately one-third of the gamma quanta we recorded are structural.

At least let us consider double electron-gamma coincidences in Fig. 10. As mentioned above, the spectrum of double coincidences should have two peaks, i.e. the peak that represents the response to the electron registration. It has no physical nature but represents the

response of the electronic system of the data acquisition and processing to the electron registration; and the second peak has a physical nature. This is the form of the time spectrum for the double electron-proton coincidences that we and the emiT group from NIST obtained during the beta decay experiments when the spectrum for the double electron-proton coincidences was obtained, where the second physical peak is associated with the registration of the beta decay event. If we and the emiT group had the task to obtain a spectrum of the double electron-gamma coincidences, then we would have also obtained a spectrum of two peaks, where the second peak, having a physical nature, would have lagged in time from the moment of electron registration by 1 µs and would have been associated with the emission of secondary gamma quanta arising at ionization of rarefied air in the experimental chamber. The authors of the "Nature letters" paper placed peak 1 µs before the registration of the electron and are now trying to "sell" the well-studied phenomenon of ionization for quite another rare effect of radiation decay of the neutron, where structural gamma-quanta can be emitted. The placement of the peak looks extremely ridiculous because for lus gammaquantum passes several hundred metres, whereas the size of their entire experimental setup is only 0.5 meters, and for this peak there is simply no room to emerge from! The peak of interest to us comes from a rare mode of neutron radiation decay, which can be detected only at registration of triple electron-proton-gamma coincidences, otherwise it simply 'sinks' in a significant gamma background.

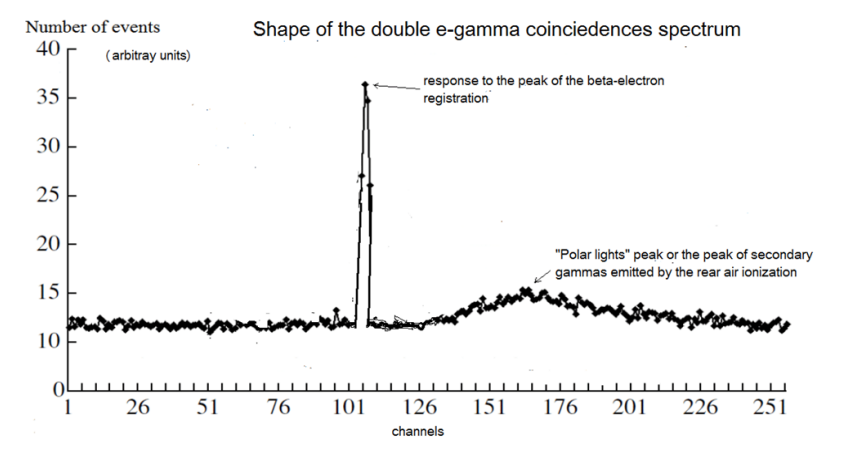


Fig. 10. The shape of the time spectrum for the double e-gamma coincidences based on the time spectrum of the triple e-p-gamma coincidences that we obtained (see Fig. 8).

To conclude our review of the time coincidence spectra, it is appropriate to note again that it would be extremely naive to expect to see one single isolated peak of triple coincidences on the spectrum, Fig. 8, the value of which determines the number of registered neutron radiation decays. As can be seen in the block diagram of our data acquisition and processing system, Fig. 3, the signals from the gamma-ray detector are fed to the triple coincidence circuit directly. It is obvious that such an ideal picture of one single isolated peak is possible only in the ideal case where the gamma background is absent. In the real

experiment, however, the gamma background is not only significant but also has its own peaks. Given its presence on the final spectrum of triple coincidences, all peaks of double coincidence spectra should appear, in our case the spectrum of double electron-proton coincidences and the spectrum of double electron-gamma coincidences – we see these peak responses on the real spectrum of triple coincidences of electron, proton and gamma-quantum.

Conclusions

The main result of our experiment is the identification of neutron radiative decay events. The location and the width of the radiative peak correspond both to the estimates and the detailed Monte Carlo simulation of the experiment. We measured the relative intensity of rare neutron decay mode, B.R. = $(3.2\pm0.53)\cdot10^{-3}$ (with C.L.= 68% and gamma quanta energy over 35 keV). It means that the average experimental B.R. value exceeds the theoretical one calculated within the standard electroweak model by 1.5 times. At the same time, the deviation of the theoretical and experimental relative intensities exceeds the standard error of 1σ . This fact means that the experiment detected additional structural gamma quanta, which are now emitted by the quark structure of the neutron during the transition of d quark to u quark. As follows from the comparison of experimental and theoretical values of the relative intensity of radiative gammas emitted during neutron decay, every third registered radiative gamma-quantum is a structural one.

In order to confirm and more accurately determine the intensity of structural gamma quanta emission, it is necessary to conduct a new experiment with a larger volume of collected statistics and with a lower threshold of energies of registered gamma quanta. We prepared such experiment several years ago, however, due to the lack of a PIK research neutron reactor, we cannot conduct it on an intense beam of cold neutrons.

The comparison of our results with the emiT group's results on the spectra for regular neutron decay shows a complete coincidence. Both we and the emiT group obtained identical double-coincidence spectra with two peaks on the horizontal ionic background. We are very pleased to state this fact. Unfortunately, we cannot say same for another NIST group which claims to measure the relative intensity of neutron radiative decay.

Not only do they not register triple coincidences, without which it is impossible to talk about the measurement of B.R., but they also cannot register neutron radiative decay events at all. Instead, the authors of the experiment study the emission of gamma quanta by residual air molecules in the chamber when they are ionized by beta electrons from neutron decay. This process is well studied and has nothing to do with neutron radiative decay. In nature, this effect of ionization of rarefied air by electrons is observed in the form of polar lights. At the same time, as can be seen from our triple coincidence spectrum in Fig. 8, this peak of delayed gamma quanta is located after electron registration with a considerable delay of the order of 1µs and is well distinguished from the peak of neutron radiative decay. This result is in a sharp contradiction with the result of NIST group which published their only peak of double electron-gamma coincidence also for 1 microsecond, however not after, but before electron registration (see Fig. 9). That is in a sharp contradiction with results of elementary evaluations, this peak simply could not appear, if it is located at such a large distance before the electron registration. We consider the location of the peak of the double electron-gamma coincidences as suggested by the authors of the contribution to Nature [7] as a sheer misrepresentation, and we understand how it happened [13]. We strongly recommend that the NIST researches withdraw their contribution to Nature and submit a new one where the only peak of the double electron-gamma coincidences is located where they actually observe it in the same 1 microsecond - not before but after the electron registration.

We express our sincere gratitude to Academician E.P. Velikhov for his support, without which we would not have been able to conduct our experiments on neutron radiative decay, neither in France at ILL, nor in Germany at TUM. We would like to thank Academician S.S. Gerstein and Professor P. Depomier of Montreal University for their interest and discussions of our work.

References

- 1. Gaponov Yu.V., Khafizov R.U. Phys. Lett. B 379 (1996) 7-12.
- Radiative neutron beta-decay and experimental neutron anomaly problem. By Yu.V. Gaponov, R.U. Khafizov, Weak and electromagnetic interactions in nuclei (WEIN '95): proceedings. Edited by H. Ejiri, T. Kishimoto, T. Sato, River Edge, NJ, World Scientific, 1995. 745p.
- About the possibility of conducting an experiment on radiative neutron beta decay, R.U. Khafizov, N. Severijns, in Proceedings of VIII International Seminar on Interaction of Neutrons with Nuclei (ISINN-8) Dubna, May 17–20, 2000, E3-2000-192, 185–195.
- 4. Khafizov R.U., Physics of Particles and Nuclei, Letters 108 (2001) 45-53.
- 5. M. Beck, J. Byrne, R.U. Khafizov, et al., JETP Letters 76, 2002, p. 332.
- 6. R.U. Khafizov, N. Severijns, O. Zimmer et al., JETP Letters, 83 (2006) p. 5.
- 7. J.S. Nico, et al., Nature, v. 444 (2006) 1059-1062.
- 8. M. J. Bales, R. Alarcon, C. D. Bass, et al., Phys. Rev. Lett. 116 (2016), 242501.
- B.G. Yerozolimsky, Yu.A. Mostovoi, V.P. Fedunin, et al., Yad. Fiz. 28, 98 (1978);
 [Sov. J. Nucl. Phys. 28, 48 (1978)].
- 10. I.A. Kuznetsov, A.P. Serebrov, I.V. Stepanenko, et al., Phys. Rev. Lett., 75 (1995)
- 11. L.J. Lising, S.R. Hwang, J.M. Adams, et al., Phys. Rev. C., v.6, 2000, p. 055501.
- 12. R.L. Cooper, T. E. Chupp, M. S. Dewey, et al, Phys. Rev. C 81, 2010, p. 035503.
- 13. N. Severijns, Nature, v. 444 (2006), 1014-1015.

Modeling the Neutron Whispering Gallery to Search for New Short Range Forces

J.A. Pioquinto^{1,2}, S. Baeßler¹, P. Cladé³, V.V. Nesvizhevsky², S. Reynaud³, K. Schreiner^{2,3,4}, M. Shi⁵, A.Yu. Voronin⁶, A. Zhao¹

¹University of Virginia, Charlottesville, VA 22904, USA
²Institut Max von Laue - Paul Langevin, 71 avenue des Martyrs, Grenoble, 38042, France
³Laboratoire Kastler Brossel, Sorbonne Université, CNRS, ENS-PSL Université, Collège
de France, Paris, 75252, Prance

⁴University of Vienna, Vienna Doctoral School in Physics, Universitätsring 1, Vienna, 1010, Austria

⁵Institute for Quantum Electronics, Eidgenössische Technische Hochschule (ETH) Zürich, CH-8093 Zürich, Switzerland

⁶P.N. Lebedev Physical Institute, 53 Leninsky prospect, Moscow, 119991, Russia

New short-range forces (SRFs) caused by weakly interacting scalar or pseudo-scalar bosons are predicted in many theories beyond the Standard Model of particle physics. For example, dark matter could be explained by the existence of a weakly interacting boson, and some theories with extra spatial dimensions predict such a particle. Neutrons are useful tools in searches for these SRFs due to their neutrality and small electric polarizability. These properties minimize false effects in experimental searches for new interactions. Precision studies of the neutron whispering gallery effect, which is the confinement of neutron matter waves along a smooth curved surface, is a particularly promising method to search for these new forces.

By sending a cold neutron beam with a grazing incidence angle into a cylindrical cut of a MgF_2 single crystal, intricate interference patterns have been observed during recent experiments at the Institut Laue Langevin. If new SRFs exist and interact with the neutrons in the whispering gallery through the nuclei in the crystal, these interference patterns will be perturbed. To look for those perturbations in the latest measurements, a theoretical model was developed to describe the observed interference patterns as a superposition of quasi-stationary states in a finite potential well. The potential well is formed by the neutron optical potential of the crystal and the centrifugal force experienced in the co-rotating reference frame of the neutron as it propagates along the surface of the cylinder. To incorporate the effects of the roughness of the mirror and the SRFs on the quasi-stationary states and their energies, logarithmic perturbation theory was used. A description of this model will be presented as well as the first analysis of the most recent experimental campaign.

Introduction

There are theories beyond the Standard Model which predict new short-range forces. These are motivated by the existence of dark matter, which could be explained by a new particle; in the framework of quantum field theory, a new particle could mediate a new force. Theories predicting the existence of extra-spatial dimensions may predict such a force as well. These SRFs can be modeled most simply as the exchange of massive spin zero bosons with

either scalar or pseudo scalar couplings to nucleons. They have scattering amplitudes in the non-relativistic limit corresponding to the tree-level diagrams in Fig. 1.

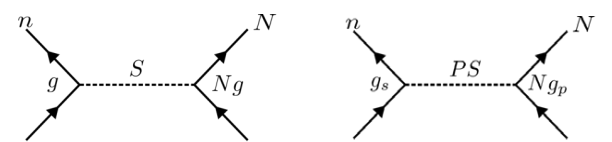


Fig. 1. Feynman diagrams of scalar (S) and pseudo scalar (PS) interactions.

In the Born approximation, these amplitudes can be associated with the Fourier transform of position space potential energies. It can be shown [1] that the scalar interaction produces a spin-independent Yukawa potential (V_S) and the pseudo-scalar interaction produces a spin-dependent potential (V_{PS}).

$$V_S \propto Ng^2 \frac{1}{r} e^{-\frac{r}{\lambda_5}}, \qquad V_{PS} \propto Ng_S g_p \left(\frac{1}{r\lambda_5} + \frac{1}{r^2}\right) e^{-\frac{r}{\lambda_5}} \vec{\sigma} \cdot \hat{r}.$$
 (1)

The range $\lambda_5 = \frac{h}{Mc}$ is the Compton wavelength of the new boson of mass M. The strength of the new potential depends on the yet unknown coupling constants, as well as the number of nucleons N being interacted with. Since this force has not been found thus far, it must be weak. To have any hope of measuring such a feeble interaction, it would be ideal to reflect a probe particle, say a neutron, off a system of many nucleons.

Neutrons are useful as probes for new SRFs since they are electrically neutral and have a weak polarizability. This makes their sensitivity to stray electric fields small compared to other particles and minimizes false effects in experiments. A simple experiment one could imagine is to let a neutron interact with many nucleons via a SRF by reflecting it from a material slab [2]. To calculate the effect of SRFs from a slab on a neutron, one can integrate over the displacement between an incident neutron and the potential energies in (1) generated by nucleons in the slab. This integration results in the potential seen in Fig. 2 which adds (or subtracts, depending on the spin if the force is spin-dependent) to the optical potential deep inside the slab, creates a diffuse potential step near the surface, and goes to zero far above the surface.

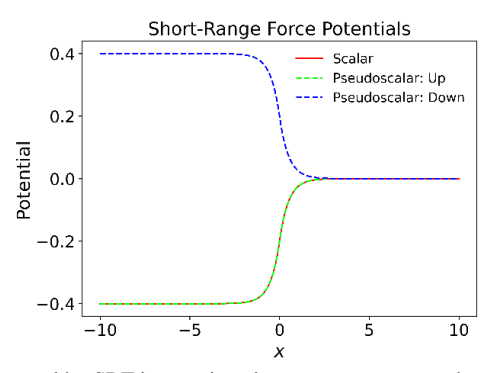


Fig. 2. Potential generated by SRF interactions between a neutron and a material slab. The slab is in the region x < 0.

To enhance the experiment's sensitivity to the diffuse potential generated by SRFs, one could imagine trying to reflect the neutron off the slab many times. This can be practically achieved if the slab is curved rather than flat. Neutrons propagating along the curved surface will then experience two potentials. First, from the surface of the mirror, which can most simply be modeled as a potential step where the height of the potential is the mirror's neutron optical potential. The second, from the centrifugal force experienced by a neutron in its rotating frame of reference as it moves along the mirror surface. In this frame, the neutron looks as if it is propagating in a gravitational field with an effective gravitational constant of $g = v^2/R$, where v is the neutron's velocity and R is the radius of curvature of the mirror. Combined, the surface and centrifugal potentials form a finite potential barrier which neutrons can form quasi-bound quantum states in, these can be seen in Fig. 6. The confinement of neutrons waves along a curved surface, or in this potential well, is the neutron whispering gallery (WG) effect and was first observed at the Institute Laue Langevin (ILL) in 2010 [3].

In the following, we will describe a recent neutron WG experiment conducted at ILL in March 2024. Then we will discuss how to efficiently model the WG using a quasi-stationary state expansion of the neutron wave function. First, in the simplest way with a perfectly smooth surface. Then, with a more realistic model, which includes perturbations from the mirror's roughness as well as the new SRFs we are searching for. Finally, preliminary results of this modeling work will be shown as a fit to experimental data.

PSD: Position 2 PSD: Position 1 Long-Lived WG Modes Short-Lived WG Modes Collimators Spin Flipperr Polarizer Chopper

Fig. 3. A scheme of the WG experiment performed at D17.

In March 2024, the neutron WG effect was measured at the D17 reflectometer at the ILL. There, cold neutrons enter the experimental area and pass through a double disk chopper to record the velocity of neutrons entering the gallery. From the chopper, neutrons enter a solid-state polarizer to filter out a spin state and a spin flipper downstream from the polarizer selects the neutrons' spin. The beam then enters a collimation system which selects the allowed beam divergence and beam size incident upon the whispering gallery mirror. The mirror itself is a single crystal of MgF₂ with a cylindrical cut of radius $R \approx 30$ mm and angular size $\Theta \approx 40^\circ$. The mirror is 100 mm long in the axial direction of the cylinder, half of that length is bare MgF₂ and the other half has a 300 nm thick Au coating. Neutrons which get trapped in the WG propagate along the surface of the mirror and exit towards a position sensitive detector which records their scattering angle and velocity.

There were two kinds of measurements during the experiment. In the first, the MgF_2 side was used, and a strong magnet was placed above it to produce a large field gradient at the surface. This gradient couples to the neutron's magnetic moment and generates a force which adds or subtracts, depending on the neutron's spin, to the centrifugal force and results in shifts of WG pattern which can be used to extract the strength of the applied gradient. This is a new effect which could be the basis of experiments which measure the gravitational acceleration of anti-atoms. The other experiment used the Au side of the mirror and had a weak magnetic field perpendicular to the surface to search for spin-dependent SRFs. This magnetic field aligns the spins perpendicular to the surface to enhance the effect of potential spin-dependent SRFs. The data that will be shown and the modeling done thus far is only for the first measurement.

Theoretical Description

For the remainder of this paper, all quantities will be represented with the dimensionless variables x, ϵ and t. These correspond to the real position $X=xl_0$, energy $E=\epsilon E_0$ and time $T=tT_0$, where $l_0=\left(\frac{\hbar^2}{2m^2}\frac{R}{v^2}\right)^{\frac{1}{3}}$, $E_0=\frac{\hbar^2}{2ml_0^2}$, and $T_0=\frac{\hbar}{E_0}$ are the characteristic length, energy, and time scales, respectively, of the WG states. To simulate the measured interference patterns generated in the gallery, the wave function of neutrons incident upon the mirror is propagated along the gallery and to the detector, see the diagram in Fig. 4.

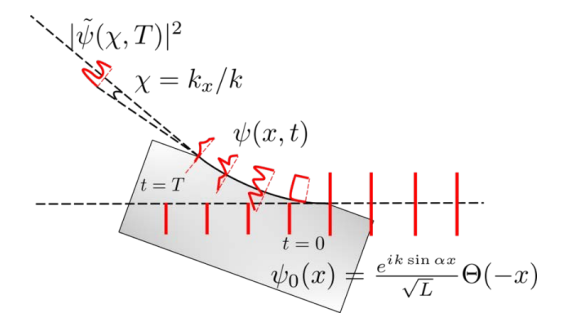


Fig. 4. A diagram of the different simulation regions. A plane wave is used as an initial state that's propagated along the mirror surface. At the end of the mirror, the final wave packet's Fourier transform is taken to determine the measured flux distribution.

The initial wave function is modeled as a plane wave. This is motivated by the choice to make the incident beam size ~100 μ m, which is much larger than the characteristic sizes l_0 of the WG states populated in the experiment, which are about 30-130 nm, depending on the wavelength. The plane wave is propagated along the mirror surface by treating the azimuthal direction semi-classically, and the radial wave function is calculated by solving the Schrödinger equation for the linear potential step model found in Fig. 6. After reaching the other end of the mirror, the final wave packet propagates in free space towards a detector. In the far field limit, the shape of the exiting wave packet evolves into the shape of its Fourier transform, or velocity distribution.

The eigenstates ψ_{ϵ} of the potential seen in Fig. 6 are part of a continuous energy spectrum, and the wave function at any time (or azimuthal position) can be described as a superposition of those states with

$$\psi(x,t) = \int_{-\infty}^{\infty} c_{\epsilon} \psi_{\epsilon}(x) e^{-i\epsilon t} d\epsilon, \qquad c_{\epsilon} = \int_{-\infty}^{\infty} \psi_{0}(x') \psi_{\epsilon}^{*}(x') dx'. \tag{2}$$

The eigenstates are constructed with the airy functions Ai and Bi and have the form

$$\psi_{\epsilon} \propto \begin{cases} f_{\epsilon} \operatorname{Ai}(x - \epsilon) & x > 0 \\ \operatorname{Ci}^{+}(x + u - \epsilon) - S_{\epsilon} \operatorname{Ci}^{-}(x + u - \epsilon) & x \leq 0 \end{cases}$$
 (3)

where $\operatorname{Ci}^\pm(z) = \operatorname{Ai}(z) \pm i \operatorname{Bi}(z)$ are incoming (+) and outgoing (-) waves in the sense that their probability currents are positive and negative, respectively. The amplitudes f_ϵ and S_ϵ are determined by the condition of continuity of ψ_ϵ and its derivative at x=0. The above integrals prove quite difficult to calculate in the case of larger potential steps u due to the presence of sharp poles that approach the real energy line in the scattering amplitude S_ϵ , as seen in Fig. 5.

Rather than doing this integration directly, the poles can be used by integrating over a contour which follows the real energy axis and encloses the poles beneath it. Then, by the residue theorem, one can write

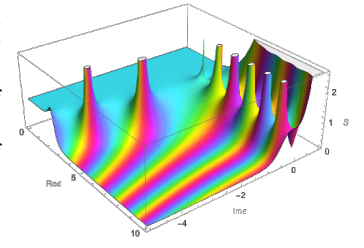


Fig. 5. Magnitude of S_{ϵ} plotted on the complex energy plane. Colors denote the phase.

$$\psi(x,t) = \sum_{n} c_n \psi_n(x) e^{-i\epsilon_n t} + E(x,t), \qquad (4)$$

where E(x,t) is an error term generated by the integral closing the contour beneath the poles. These poles are associated with so-called quasi-stationary states ψ_n which, unlike stationary states, decay with time since they are trapped in a potential well with a finite barrier that can be traversed by tunneling or transmission. They can be seen in Fig. 6. Mathematically, the decay of these states comes from their complex energy levels ϵ_n , which have negative imaginary parts. The sum in the above expression is the quasi-stationary state expansion (QSE) and is a computationally more efficient way of calculating the wave function's time evolution.

However, the validity of the QSE is not obvious due to the presence of the error term E. To check how it performs, a numerical simulation was developed to calculate the propagation of the wave function along the mirror surface. Since neutrons that tunnel into the mirror should disappear from the triangular well, as seen in Fig. 6, the simulation is implemented with transparent boundary conditions [4]. This allows wave packets incident upon the edge of the computational region to exit without unphysical reflections back into the potential well. When comparing the numerical simulation to the QSE, we find that for short times they disagree significantly, but in the large t limit there's good agreement, see Fig. 7.

Neutrons which traverse the gallery satisfy this long-time condition, so we find the QSE satisfactory for modeling our measurements.

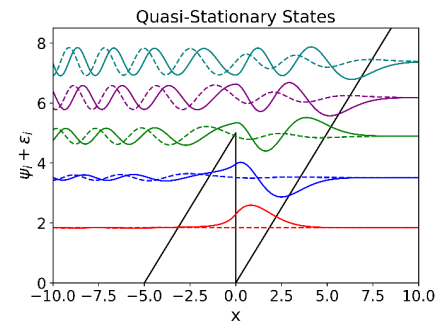


Fig. 6. The first 5 quasi-stationary states in a WG potential with a sharp step. The solid lines are the real parts and the dashed lines are the imaginary parts of the eigenstates. The solid black line is the potential energy. For clarity, each state is vertically displaced by its dimensionless energy.

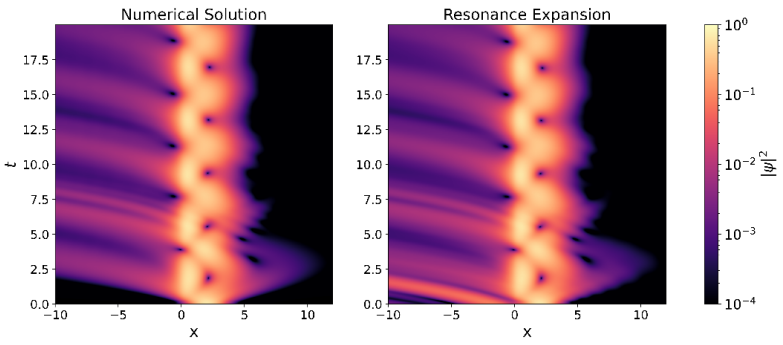


Fig. 7. A comparison of the numerical simulation and the QSE of the evolution of a Gaussian wave packet.

Unfortunately, the step potential model of the mirror used thus far may be an oversimplification. The mirror has a rough surface which must be considered. To do so, we smoothen out the potential step and model the mirror surface with a Woods-Saxon potential. This model is chosen since it has exact solutions in the absence of external fields, which make approximating WG solutions with a rough potential more mathematically tractable. We are also trying to measure the effect of new short-range forces on the whispering gallery, so their potential contribution must also be considered. Fig. 8 shows the effect of these two potentials, where the new force is assumed to be the Scalar interaction.

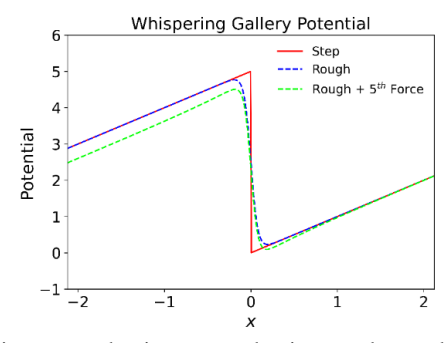


Fig. 8. WG models assuming a smooth mirror, a rough mirror, and a rough mirror with SRFs.

To consider these perturbations, one could try to use the standard Rayleigh-Schrödinger perturbation theory (RSPT) of bound states on the quasi-stationary states to extract corrections to their energies and wave functions. However, this fails since RSPT demands that the states form a complete basis, and quasi-stationary states do not necessarily satisfy this condition. An alternative which does not depend on this condition is logarithmic perturbation theory (LPT) [5]. Instead of expanding an eigenstate and its energy directly into a perturbation series and inserting them into the perturbed Schrödinger equation, as is done in RSPT, one can instead expand the logarithm of the state $G = \log \psi$ and its eigenenergy as a perturbation series. We can write the Schrödinger equation in terms of G with an unperturbed potential V_0 and a perturbed potential V_1 as

$$-\psi'' + (V_0 + \lambda V_1)\psi = \epsilon \psi \to G'' + G'^2 = V_0 + \lambda V_1 - \epsilon.$$
 (5)

The λ factor is simply a bookkeeping device to be set to 1. The perturbation series to be calculated is then

$$G = G_0 + \lambda G_1 + \lambda^2 G_2 + \cdots \quad \epsilon = \epsilon_0 + \lambda \epsilon_1 + \lambda^2 \epsilon_2 + \cdots, \tag{6}$$

the terms of which can be found by inserting these series into the Schrödinger equation and matching terms with the same order of λ to yield

$$G_0'' + G'^2 = V_0 - E_0$$

$$G_1'' + 2G_0'G_1' = V_1 - E_1$$

$$G_2'' + 2G_2'G_0' = -E_2 - {G_1'}^2$$
(7)

To make the problem tractable, we only consider perturbations of finite range. This way, when we solve the above equations, we can take advantage of the boundary condition that outside the range of the potential, $G \propto G_0$, which is the unperturbed solution. Up to first and second order, it can be shown that

$$\epsilon_{1} = \frac{\int_{a}^{b} V_{1}(x) \psi_{0}^{2} dx}{\int_{a}^{b} \psi_{0}^{2} dx + \dot{G}_{0}' \psi_{0}^{2} \Big|_{a}^{b}}, \quad \epsilon_{2} = -\frac{\int_{a}^{b} G_{1}^{2} \psi_{0}^{2} dx + \frac{1}{2} \varepsilon_{1}^{2} \ddot{G}_{0}' \psi_{0}^{2} \Big|_{a}^{b}}{\int_{a}^{b} \psi_{0}^{2} dx + \dot{G}_{0}' \psi_{0}^{2} \Big|_{a}^{b}}, \tag{8}$$

$$G_{1}(x) = \int_{x}^{\infty} \frac{1}{\psi_{0}^{2}(x')} \int_{x'}^{\infty} (V_{1}(x'') - \epsilon_{1}) \psi_{0}^{2} dx'' dx',$$

$$G_{2}(x) = -\int_{x}^{\infty} \frac{1}{\psi_{0}^{2}(x')} \int_{x'}^{\infty} (G_{1}^{\prime 2}(x'') + \epsilon_{2}) \psi_{0}^{2} dx'' dx',$$
(9)

where a, b are outside the potential range. The notation \dot{G} should be interpreted as $\frac{\partial G}{\partial \epsilon}$. To extract corrections to the wave function, we expand the function

$$\psi = e^G = \psi_0 \left(1 + \lambda G_1 + \lambda^2 \left(\frac{1}{2} G_1^2 + G_2 \right) \right) = \psi_0 + \lambda \psi_1 + \lambda^2 \psi_2 + \cdots.$$
 (10)

To verify that this perturbation theory works for our purposes, we compared it to an exactly solvable problem. We can model the roughness model of the WG using the linear potential with a step, as before, but now in the region surrounding the step, we replace the potential with only the Woods-Saxon potential. [6] In this model, the linear portions of the potential are exactly solved with Airy functions, and the Woods-Saxon section is solved with Hypergeometric functions [7]. For small roughness (or the size of the diffusiveness of the potential), our model potential and this approximate potential are nearly indistinguishable, as seen in Fig. 9.

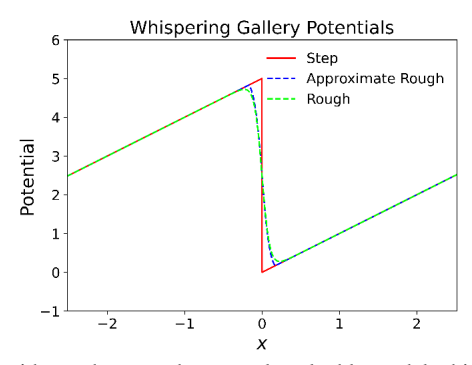
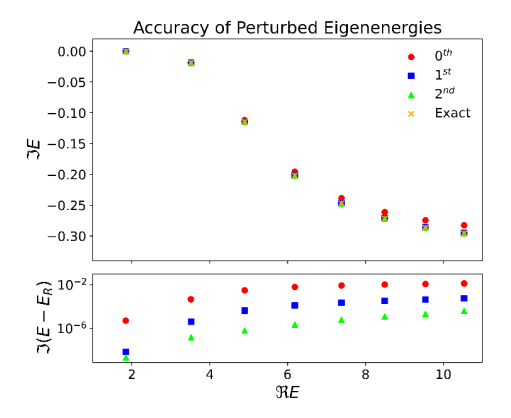


Fig. 9. WG model with roughness and an exactly solvable model which approximates it.

The eigenenergies and eigenstates for the solvable model were found and compared to a perturbation series which tries to solve the same model. Fig. 10 shows that agreement between the eigenenergies calculated with LPT and those found with the exact model consistently improves with each additional order of perturbation, and the same is true for the eigenstates, validating this approach.



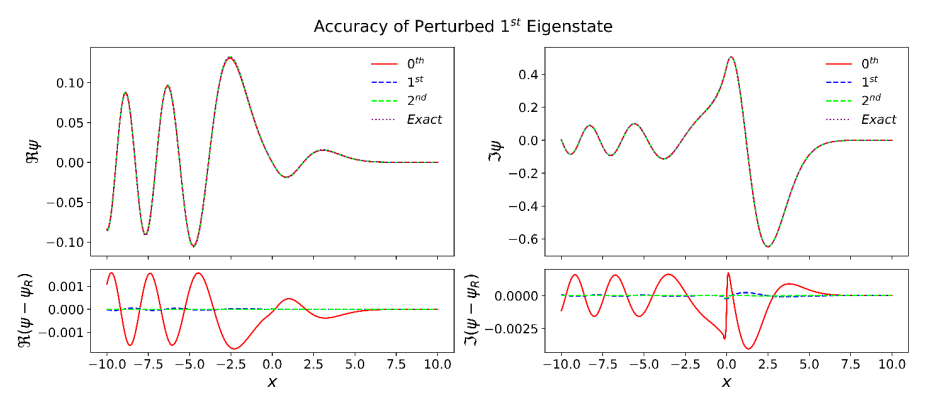


Fig. 10. The top row of each plot shows the results of the perturbation series with the unperturbed and exact solutions to the approximate roughness model. The bottom row shows the difference between each order of perturbation and the exactly solvable model. The difference between the exact solution and the perturbation series becomes smaller with each successive order of correction.

Using the formalism developed, experimental data was fit with maximum likelihood estimation. The initial fit only considers parameters of the instrument, i.e., the detector distance, timing offset of time-of-flight system, time-of-flight distance. The parameters pertaining to the mirror, like its average roughness size, angular size, and radius of curvature are not yet fit. Although, separate measurements using neutrons, x-rays, and optical microscopy were done to characterize these parameters and are used as inputs into the simulation. The results can be seen in Fig. 11 and show good qualitative agreement between theory and experiment.

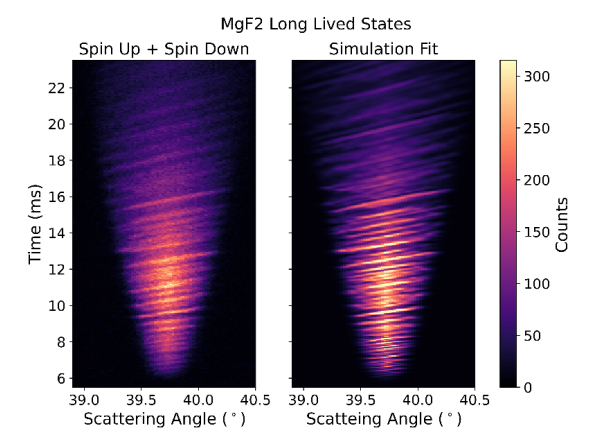


Fig. 11. The pattern on the left is experimental data collected at D17 during the measurement with the MgF_2 surface. The measurement was spin averaged to simplify the analysis and reduce the effect of the applied magnetic field. The color indicates the number of counts. The image on the right is a simulation with the instrument parameters fit to the data on the left.

Conclusion

A model of the neutron whispering gallery effect is developed using a quasi-stationary state expansion and logarithmic perturbation theory. These techniques were validated by numerical simulations and comparison to an exactly solvable model and are now being used to simulate data. Simulations using these techniques qualitatively reproduced recently measured data, but more analysis work is to be done. With this formalism, we are also equipped to calculate the effect of new short-range forces and work is now being done to place constraints on spin-dependent and spin-independent SRFs.

Acknowledgments

This work was supported by the National Science Foundation under grant PHY-2412782 as well as the James G. Beitchman award for Innovative Graduate Student Research in Physics.

References

- 1. Moody, J. E. & Wilczek, F. New macroscopic forces? Phys. Rev. D 30, 130–138 (1984).
- Leeb, H. & Schmiedmayer, J. Constraint on hypothetical light interacting bosons from low-energy neutron experiments. *Phys. Rev. Lett.* 68, 1472–1475 (1992).
- 3. Nesvizhevsky, V. V., Voronin, A. Y., Cubitt, R. & Protasov, K. V. Neutron whispering gallery. *Nature Phys* **6**, 114–117 (2010).
- 4. C. A. Moyer, Am. J. Phys. 72, 351 (2004).
- 5. PT Leung et al J. Phys. A: Math. Gen. 31 3271 (1998).
- 6. S Reynaud, Whispering Gallery with a Rounded Step (Unpublished, 2023).
- Landau, L. D. & Lifshitz, L. M. Quantum Mechanics: Non-Relativistic Theory. (Butterworth-Heinemann, Singapore, 1981).

Investigation of the Inverse Leidenfrost Effect in the Production of Moderating Material for Cold Neutron Sources

Alexey Galushko, <u>Ivan Litvak</u>, Maxim Bulavin, Roman Chepurchenko

Joint Institute for Nuclear Research, FLNP, Dubna

Introduction

Cryogenic neutron moderators are an important part of the IBR-2M research pulsed reactor located at the Joint Institute for Nuclear Research (JINR) in Dubna. Their main task is to slow down neutrons to low energies, which is necessary for conducting various experiments. For this purpose, frozen beads made from a mixture of mesitylene and m-xylene are used. These beads, due to their properties at extremely low temperatures, effectively reduce the speed of neutrons. The production of such beads requires strict control to ensure their quality and safety of use in the cryogenic moderator at the reactor. The article presents a device that applies the reverse Leidenfrost effect to create a dispersed moderating substance, which improves both the efficiency and safety of the process.

Reverse Leidenfrost Effect

The reverse Leidenfrost effect occurs when a drop of liquid, such as a mixture of mesitylene and m-xylene, falls onto a surface with a temperature significantly below its boiling point, in this case, liquid nitrogen. Upon contact of the drop with liquid nitrogen, intense evaporation of nitrogen occurs at the point of contact. This creates a thin vapor cushion under the drop, isolating it from direct contact with the liquid. This isolation slows down heat exchange, allowing the drop to "hover" above the surface. This effect plays a key role in the freezing process, as it ensures uniform cooling of the drops and prevents them from sticking together, which is critical for obtaining homogeneous and high-quality beads.

Device and Production Process of Beads

A special device has been developed for the production of frozen beads, consisting of a cryostat and a dropper. The cryostat is a vertical vessel filled with liquid nitrogen, insulated with a vacuum jacket to minimize heat inflows. Inside the cryostat, there are cells that separate the drops, preventing them from merging during freezing. The dropper forms drops of the mixture of mesitylene and m-xylene, which then fall into the cryostat. In liquid nitrogen, the drops turn into solid beads with a diameter of 3.6 to 3.9 mm, which accumulate at the bottom of the vessel. This process ensures high uniformity of the beads and minimizes defects, which is important for their application in neutron moderation.

Analytical Approach to Calculating the Formation Time of Beads

To determine the time required for the formation of the beads, the authors applied an analytical model based on the concept of a vapor cushion. The model assumes that the freezing process is quasi-static, the drops are spherical, and crystallization occurs uniformly. The calculations take into account parameters such as the radius of the drop, the melting

temperature of the mixture, the Leidenfrost temperature, and the thermophysical characteristics of the materials. For example, for a drop with a radius of 1.875 mm, the model predicts a cooling time to the melting temperature of about 3 seconds. This approach not only allows calculating the duration of the process but also optimizing production conditions to increase efficiency.

Formation of Solid Frozen Beads

The process of forming the beads goes through several stages. First, the drop, upon entering liquid nitrogen, levitates above the surface due to the vapor cushion, which ensures its gradual and uniform cooling. Then, crystallization begins, and the drop turns into a solid bead. The levitation time depends on the size of the drop and the Leidenfrost temperature: for example, for a bead with a radius of 1.8 mm, it is about 10 seconds. When the temperature of the bead drops below the Leidenfrost temperature, the vapor cushion disappears, the bead sinks into the liquid nitrogen and completely freezes. This mechanism ensures the correct shape and structure of the beads.

Results and Their Significance

The applied analytical model demonstrates good agreement with experimental results, confirming its accuracy and practical value. It allows predicting the formation time of the beads depending on their size and other conditions. However, about 5% of the beads turn out to be defective due to the heterogeneity of their sizes, which is associated with random fluctuations during the detachment of drops from the dropper. Despite this, the study lays the foundation for further improvement of the technology, which can enhance the safety and performance of cryogenic moderators in the future.

Conclusions and Prospects

The authors plan to continue working on accelerating the bead production process and creating an automated device with high productivity, which exceeds the existing one by 20 times. It is also expected to eliminate the influence of random factors, such as the instability of drop formation, by accumulating additional experimental data. The developed methods and model open up opportunities for creating more reliable systems for producing moderating substances, which is of great importance for the operation of cold neutron sources and ensuring their safety.

Determination of Partial Neutron Widths of the 397.8 eV p-Wave Resonance of ³⁵Cl Nucleus

V.L. Kuznetsov^{1,3}, A. Yergashov^{1,2}, Yu.N. Kopatch¹, L.V. Mitsyna¹, A.I. Oprea^{1,4}, C. Oprea⁵, N.V. Rebrova¹, C. Hramko¹, P.V. Sedyshev¹

¹Frank Laboratory of Neutron Physics, Joint Institute for Nuclear Research, Dubna
²Institute for Nuclear Physics, Almaty, Republic of Kazakhstan
³Institute for Nuclear Research of the Russian Academy of Sciences,
Moscow, Russian Federation

⁴Technical College "Alexandru Roman", Alesd, Bihor County, Romania

⁵High School "Lucian Blaga", Oradea, Bihor County, Romania

Angular distributions of gamma quanta emitted in radiative neutron capture process were measured in the neutron energy region of the p-wave resonance of ^{35}Cl nucleus. The expressions of the effect of forward-backward asymmetry and anisotropy in the angular distribution of gamma quanta for investigated nucleus were obtained in a frame of the mixing states of compound nucleus with the same spin I=3/2 and opposite parities formalism. The partial neutron widths, $\Gamma^n_{p,1/2}$ and $\Gamma^n_{p,3/2}$, were obtained using both the experimental data and theoretical evaluations of the effects of forward-backward asymmetry and anisotropy of gamma quanta.

An investigation of a ratio of the partial neutron widths in the two-component neutron resonance of an excited nucleus was initiated by F.L. Shapiro in 1967 [1]. At the Frank Laboratory of Neutron Physics, JINR a bundle of experiments for determination of angular dependence of scattered neutrons as well as of the partial neutron widths ratio were carried out in 1964–1993 by G.S. Samosvat group [2]. A discovery of spatial parity violation in nuclear fission in 1977 stimulated theoretical [3] and experimental works [4–6] for a search of the effects of such violation in neutron-nuclear interactions. As was shown in ref. [7], the $\Gamma_{p,1/2}^n$ value supports an important role in P-odd asymmetry in transmission of neutrons. In this connection, in FLNP, JINR experimental investigations of forward-backward asymmetry and right-left asymmetry of gammas from (n,γ) reaction were started in order to discover P-even $(\vec{k}_n\vec{k}_{\gamma})$ and $(\vec{s}_n[\vec{k}_n\vec{k}_{\gamma}])$ correlations, correspondingly. At that a sizeable P-odd asymmetry in neutron transmission was discovered on ¹¹⁷Sn and ¹¹³Cd nuclei [8]. The experimental results presented in [8] was analyzed according to developed formulae from paper [9], in which (n,γ) reaction at nuclei with spin $\frac{1}{2}$ is considered. Moreover, the limit for a value of P-even and T- noninvariant amplitude in (n,γ) reaction was assigned in [10].

Recently, investigation series [11–16] was published, in which angular distributions of γ -quanta were measured from (n,γ) reaction on ^{139}La , 117 Sn, 113 Cd, ^{81}Br and ^{131}Xe nuclei using germanium detectors of high-resolution permitted an effective isolation of γ -transmissions. These experiments were carried out in a framework of training for a search of T-invariance violation. In the significant work [17] the neutron partial widths $\Gamma^n_{p,1/2}$ and $\Gamma^n_{p,3/2}$ were determined with the use of polarized neutrons on ^{139}La polarized nuclei.

In connection with an accepted decision to continue in PLNP, JINR the research program for a study of p-wave resonances offered in refs. [2,8], a prototype of "Gamma" installation was created at 11-meter flight-path of 4th channel of the source of resonance

neutrons (IREN) for investigation of P-even angular correlations in nuclear p-wave resonances of (n,γ) reactions.

According to papers [2,8,9] differential cross section of (n,γ) reaction for a flux of unpolarized neutrons can be presented as:

$$\frac{d^2\sigma_{\gamma}(E_n,\theta)}{dE_n}d\theta = A(a_0 + a_1(E_n)P_1(\theta) + a_2(E_n)P_2(\theta)). \tag{1}$$

Here A is a constant, $a_0 = A\left(|U_s|^2 + \left|U_p\right|^2\right)$ is a cross section of the (n,γ) reaction, $a_1 = Re\left(U_sU_p^*\right) \cdot f_1(x,y), \quad a_2 = \left|U_p\right|^2 \cdot f_2(x,y), \quad U_s \text{ and } U_p \text{ are reaction amplitudes, } P_1(\theta)$ and $P_2(\theta)$ are Legendre polynomial terms at neutron orbital moments l=1 and l=2, $x^2 = \Gamma_{p,1/2}^n$ and $y^2 = \Gamma_{p,3/2}^n$. Suppose for a simplicity that both multiplicity of γ -quanta, ν , and detection efficiency of gammas, ε , are equal to 1.

In any case, a number of recorded gammas, N_{γ} , can be written as:

$$N_{\gamma} = \nu \cdot \varepsilon \cdot N_0 \left(1 - exp(-\sum_t (E_n) L) \right) \cdot \sum_{\gamma} \frac{(E_n, \theta)}{\sum_t (E_n)}. \tag{2}$$

Here N_0 is a number of incident neutrons with energy E_n , $\sum_t (E_n)$ is a total macroscopic cross section, L is a thickness of the investigated sample, $\sum_y (E_n)$ is a macroscopic cross section of (n,γ) reaction. If to choose θ angles in such a way that $\cos^2(\theta) = 1/3$, so a term with a_2 in (1) disappears, and a difference of γ -quanta emitted forward and backward is:

$$N_{\gamma}^{F} - N_{\gamma}^{B} = \frac{2}{\sqrt{3}} \nu \cdot \varepsilon \cdot N_{0} \left(1 - exp(-\sum_{t} (E_{n}) L) \right) \cdot \sum_{\gamma} (E_{n}) a_{1} / \sum_{t} (E_{n})$$
 (3)

and a sum of γ -quanta emitted forward and backward in this case is:

$$N_{\gamma}^{F} + N_{\gamma}^{B} = \frac{2}{\sqrt{3}} v \cdot \varepsilon \cdot N_{0} \left(1 - exp(-\sum_{t} (E_{n})L) \right) \cdot \sum_{\gamma} (E_{n}) / \sum_{t} (E_{n}). \tag{4}$$

The ratio of equations (3) and (4) defines a_1 coefficient [8]:

$$a_1 = \left(N_{\gamma}^F - N_{\gamma}^B\right) / \left(N_{\gamma}^F + N_{\gamma}^B\right). \tag{5}$$

As is shown in [8,9], energy dependence of a_1 coefficient near p-wave resonance have the following form:

$$a_1(E_n) \approx (2(E - E_0)/\Gamma)/(4(E - E_0)^2/\Gamma^2 + 1)$$
 (6)

and the a_1 value decreases more than a hundred times by integration of equation (6) within the range from $(E_0 - 10\Gamma)$ to $(E_0 + 10\Gamma)$. Such approach was used in [2] for determination of a_2 coefficient.

This work aim was an exploring of ability for the prototype of the "Gamma" installation to operate in the region of neutron energies up to 400 eV. The granular CaCl₂

sample was taken as a target to investigate $^{35}\text{Cl}(n,\gamma)$ -reaction. P-odd and P-even correlations were earlier investigated at the ^{35}Cl nuclei both in (n,γ) -reaction and in (n,p)-reaction with thermal neutrons [19,20], and there was an attempt to measure forward-backward asymmetry of the reaction products near p-wave resonance with E_n =398 eV [21].

An average power of electron beam of the IREN installation at the time of our experiment was 1.5 kW, pulse repetition frequency – 50 Hz, electron pulse duration – 100 ns. Electron pulse was focused at tungsten target as a spot with 35 mm in diameter. A density of resonance neutron flux measured using gold foils activation was $f_{res} \approx 6 \cdot 10^3 \text{n/(s} \cdot \text{cm}^2)$ [18].

Total measuring time for $^{35}\text{Cl}(n,\gamma)$ -reaction with cylindrical target of CaCl₂ (granules in glass container with a height of 20 mm and diameter of 80 mm) was 25 hours $(4.5\times10^6$ electron pulses). A gammas angular distribution was registered by six BGO scintillation detectors, which were installed under 55^0 , 90^0 , 125^0 , 235^0 , 270^0 , and 305^0 angles relative to neutron flux direction. Registration efficiency of γ -quanta with the energy 1.1 MeV and 1.3 MeV amounted to $5\cdot10^{-3}$. A typical parabolic dependence of γ -quanta energy on amplitude channel of analyzer was shown in Fig.1.

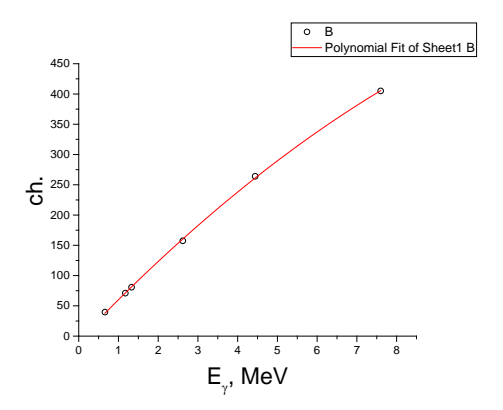


Fig. 1. Energy calibration of amplitude analyzer.

All detectors were calibrated by lines of 137 Cs (661 keV), 60 Co (1173 keV and 1330 keV), 228 Th (2620 keV), as well as by 4430 keV and 7600 keV κ 3B lines of 56 Fe(n, γ) 57 Fe reaction in such a way as to make measured γ -spectra practically identical for all detectors.

Fig.2 presents amplitude γ -spectra measured by one of detectors, where black line shows γ -spectrum in the neutron energy region of p-wave resonance (corresponded to the 390–404 eV interval of the time-of-flight γ -spectrum), and background γ -spectra at the energies lower (interval of 378–389 eV of the time-of-flight spectrum) and higher (403–413 eV) than p-wave resonance location is shown by red line.

A difference of these amplitude γ -spectra is evident. The hydrogen line 2.23 MeV is especially prominent, and γ -spectra of all detectors were normalized just by this line in order to have the same size of integral of total capture for hydrogen line in both "under peak" and "background" intervals.

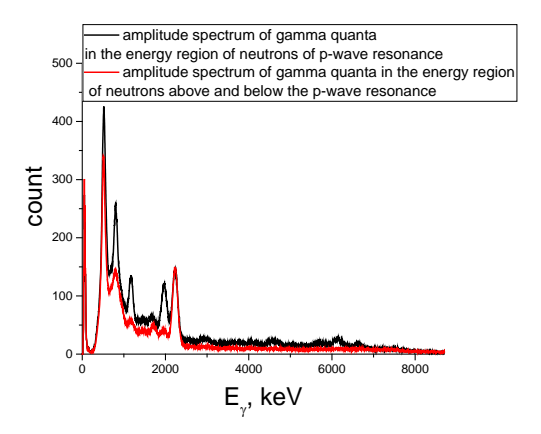


Fig. 2. Amplitude spectra of γ -quanta: black line – γ -spectrum in the neutron energy region of p-wave resonance; red line – background γ -spectrum at the energies lower and higher than p-wave resonance location.

Fig.3 presents an amplitude spectrum of γ -quanta from $^{35}Cl(n,\gamma)$ -reaction connected with neutron capture in the 398-eV p-wave resonance ("background" spectrum is extracted here) for one of the detectors.

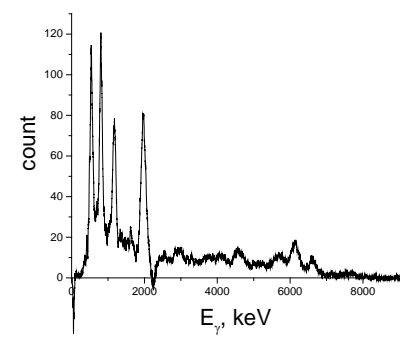


Fig.3. Amplitude spectrum of γ -quanta from 35 Cl(n, γ)-reaction corresponded to the 390–404 eV interval of the time-of-flight spectrum (in the region of the 398-eV p-wave resonance).

In contrast to measurements of forward-backward and right-left asymmetries in (n,γ) -reaction at 117 Sn and 113 Cd nuclei [8], where the line of high-energy E1-transition predominates, in (n,γ) -reaction on 35 Cl there is no any strongly dominated line. And as was shown in [9], in γ -quanta cascade a nulling of forward-backward asymmetry, in principle, is possible, as its value randomly depends on final state of the cascade.

Time-of-flight spectra of neutrons in the region, which concludes the investigated presonance, for all detectors, installed under indicated forward and backward angles relative to neutron beam, were divided into 7 energy parts (2 eV each). In the amplitude spectra of each 2 eV-interval for each detector the line of 1959 keV transition was selected, and its areas were calculated after background extracting in all intervals of all detectors.

In the upper picture of Fig.4 the summarized counts of the peaks of "forward" (black points) and "backward" (open points) detectors depending on middle neutron energy of 2 eV-intervals are presented. The lower picture of Fig.4 shows the energy dependence of the coefficient of forward-backward asymmetry, which is a ratio of difference of the summarized counts of "forward" and "backward" detectors to their sum:

$$\frac{N_{forward}(E) - N_{backward}(E)}{N_{forward}(E) + N_{backward}(E)}$$

The uncertainties are statistical ones with taking into account extracted backgrounds.

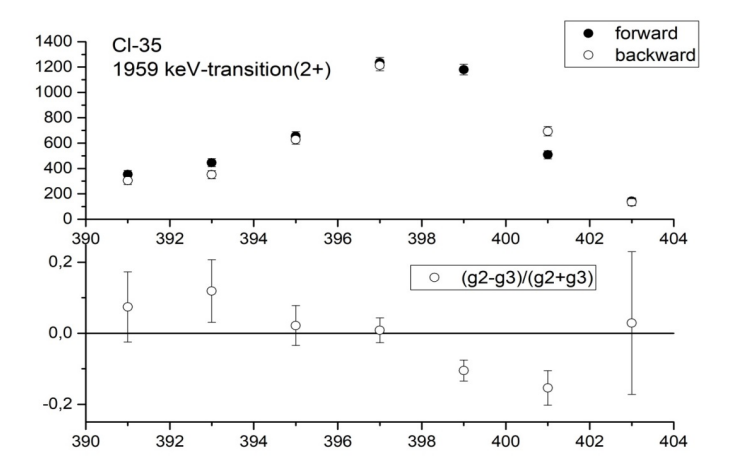


Fig.4. Dependences on the incident neuron energy (X-axis: middle energy of 2 eV-intervals in eV) of summarized counts of "forward" (black points) and "backward" (open points) detectors – upper picture and of the forward-backward asymmetry of gammas – lower picture.

Conclusion

In summary we can say that in the process of experimental studying of 35 Cl(n, γ)-reaction near two-component p-wave resonance, the procedure was constructed for measuring P-even correlations. In spite of insufficiently high resolution of used BGO-detectors the measured experimental amplitude γ -spectra allowed obtaining of the coefficient of forward-backward asymmetry in the 1959 keV primary transition of the cascade decay of the p-wave resonance of 398 eV.

References

- 1. Shapiro F.L., Collection of lectures of All-Union summer school on nuclear spectroscopy at nuclear reactions. Obninsk, ΦЭИ (Physico-Energy Institute), 1967, p.239 (in Russian).
- 2. Samosyat G.S., Investigation of p-wave scattering of neutrons by nuclei. PEPAN, 1995, v.26, iss.6, p.1567 (in Russian).
- 3. Sushkov O.P., Flambaum V.V. Pis'ma v ZhETF, 1980, v.32, p.377 (in Russian).
- 4. Forte M. et al. Phys. Rev. Lett., 1980, v.45, p. 2088.
- 5. Kolomensky E.A. et al. Phys. Lett. Ser. B, 1981, v.107, p.272.
- 6. Alfimenkov V.P. et al. Pis'ma v ZhETF, 1981, v.34, p.308 (in Russian).
- 7. Bunakov V.E., Gudkov V.P., Parity nonconservation effects in neutron elastic scattering reactions. Zs. Phys. A, 1981, v.303, 1981, p. 285–291.
- 8. Skoy V.R., Sharapov E.I. PEPAN, 1991, v.22, iss.6, p.1400 (in Russian).
- 9. Flambaum V.V., Sushkov O.P. Nucl. Phys., A435, 1985, p.352.
- 10. Barabanov A.L., Sharapov E.I., Skoy V.R., Frankle C.M., Testing T-odd, P-even interactions with gamma rays from neutron p-wave resonances. Phys. Rev. Lett., 1993, v. 70, iss. 9, p. 1216.
- 11. Okudaira T., Takada S., Hirota K. et al., Angular distribution of gamma-rays from neutron-induced compound states of ¹⁴⁰La. Phys. Rev. C, 2018, v. 97, 034622.
- 12. Okudaira T., Shimizu H.M., Kitaguchi M., Hirota K., Haddock C.C. et al., Measurement of the angular distribution of γ -rays after neutron capture by ^{139}La for a T-violation search. EPJ Web Conf., 2019, v. 219, 09001.
- 13. Endo S., Shimizu H.M., Kitaguchi M., Katsuya H., Yamamoto T. et al., Measurement of the angular distribution of γ-rays emitted from the compound state after neutron capture by ⁸¹Br for a search of T-violation. EPJ Web Conf., 2019, v. 219, 09003.
- 14. Koga J., Takada S., Yoshioka T., Shimizu H.M., Hirota K. et al., Measurement of the angular distribution of prompt gamma-rays emitted in the 117 Sn(n, γ) reaction for a Tviolation search. EPJ Web Conf., 2019, v. 219, 09004.
- 15. Yamamotto T., Okudaira T., Endo S. et al., Transverse asymmetry of γ rays from neutron-induced compound states of ¹⁴⁰La. Phys. Rev. C 101, 064624 (2020).
- 16. Okudaira T., Endo S., Fujioka H. et al., Energy-dependent angular distribution of individual γ- rays in the ¹³⁹La(n,γ)¹⁴⁰La* reaction. Phys. Rev. C **104**, 014601 (2021).
 Okudaira T., Nakabe R., Auton C.J. et al., Spin dependence in the p-wave resonance
- of ¹³⁹La + n. Phys. Rev. C **109**, 044606 (2024).
- 18. Yergashov A., Kopach Yu.N., Kuznetsov V.L. et al., Investigations of low-energy presonances in (n,γ) Reaction on ⁹³Nb. PEPAN Letters, Vol. 22, No. 2, 2025, 284–288.
- 19. Vesna V.A., Kolomensky E.A., Lobashev V.M. et al. Pis'ma v ZhETF, v. 36, iss.5. p.169 (in Russian).
- 20. Antonov A., Vesna V.A., Gledenov Yu.M. et al. Pis'ma v ZhETF, v.40, iss. 5, p.209 (in Russian).
- 21. Gledenov Yu.M., Machrafi R., Oprea A.I. et al., Determination of the forward backward asymmetry coefficient in ³⁵Cl(n,p)³⁵S. VII International Seminar on Interaction of Neutron with Nuclei, Dubna, E3-98-212, 1999, p. 295.

Primary Gamma Transitions in ¹⁷⁶Lu and ¹⁷⁷Lu after Resonance Neutron Capture

G. Ahmadov^{1,2,3}, D. Berikov^{1,4}, W. Jiang⁵, G. Yang^{6,7}, W. Furman¹, C. Hramco¹, S. Nuruyev^{1,3}, S. Telezhnikov¹, A. Madadzada^{1,2}

¹Joint Institute for Nuclear Research, 141980, Dubna, Russia
²Department of Nuclear Research of IDDA, AZ0100, Baku, Azerbaijan
³ Institute of Radiation Problems- MSE, AZ1143, Baku, Azerbaijan
⁴Institute of Nuclear Physics, Ministry of Energy of the Republic of Kazakhstan, 050032, Almaty, Kazakhstan
⁵Institute of High Energy Physics, CAS, 100049, Beijing, China

³Institute of High Energy Physics, CAS, 100049, Beijing, China ⁶Institute of Modern Physics, Chinese Academy of Sciences, 730000, Lanzhou, China ⁷School of Physics and Astronomy, Sun Yat-sen University, 519082, Zhuhai, China

^{175,176}Lu (n,γ)^{176,177}Lu reactions were studied via radiative capture of resonance neutrons at the CSNS Back-n White Neutron Source. Using the time-of-flight (ToF) technique, γ-ray spectra for isolated resonances were measured. The experiment was conducted with a coaxial HPGe gamma detector equipped with an anti-Compton system, positioned 20 cm from the target. A 60 g sample of metallic natural lutetium (nat Lu) with 99.9% purity (dimensions: 60×2.2 mm) was used as the target, located 76 m from the spallation target in the ES#2 experimental hall. The ToF spectrum was measured in the 1–700 eV energy range, with sufficient γ-ray statistics up to 100 eV. The measurement time was approximately 200 hours. The ToF resolution enabled the extraction of γ-ray spectra from 16 neutron resonances for the 175 Lu(n,γ) 176 Lu reaction. Due to the low natural abundance of 176 Lu (2.6 %), γ-ray spectra were obtained from 10 resonances for 176 Lu (n,γ) 177 Lu reaction. This work focused mainly on the identification and analysis of primary gamma transitions in 176 Lu.

Introduction

Understanding primary gamma transitions following resonance neutron capture is fundamental for exploring the nuclear structure and decay dynamics of deformed nuclei such as 176 Lu and 177 Lu. Early benchmark studies provided important measurements of E1 and M1 gamma-transition intensities for the 175 Lu(n, γ) 176 Lu reaction [1–3]. These pioneering works revealed how γ -rays populate low-lying excited states belonging to different rotational and vibrational bands, and offered initial insights into phenomena like K-mixing.

However, despite these valuable contributions, the available experimental data have remained limited for decades. Previous measurements typically covered only a small number of neutron resonances – four and seven resonances for $J^{\pi}=4^+$ and $J^{\pi}=3^+$, respectively – and were mainly restricted to the 0–50 eV neutron energy range. Furthermore, the low natural abundance of ¹⁷⁶Lu (2.6 %) has historically posed challenges for obtaining sufficiently detailed spectra, resulting in significant gaps in the available information on partial gamma widths and the detailed decay pathways of the compound nuclei [4].

With the advent of modern neutron sources and advanced detection technologies, it has become possible to revisit these reactions with higher precision and over broader energy ranges. One of this modern neutron sources is China Spallation Neutron Source (CSNS) [5]. This facility provides high-intensity pulsed neutron beams suitable for time-of-flight measurements, allowing us to resolve isolated resonances up to several mega electron volts [6]. Motivated by this, we have carried out new measurements of the $^{175,176}Lu(n,\gamma)^{176,177}Lu$ reactions at the CSNS Back-n White Neutron Source [7].

In this paper, we focus in particular on the identification and analysis of primary gamma transitions in ¹⁷⁶Lu following resonance neutron capture and on their detailed comparison with evaluated data from the existing literature. This work demonstrates how the new experimental results are consistent with previous datasets and how further improvements on event statistics can be made.

Experimental details

Fig. 1 shows a photograph of the experimental setup used at the ES#2 station of the Back-n White Neutron Source at CSNS. The setup consists of four main components: the target holder with the ^{nat}Lu target, the coaxial HPGe detector with its anti-Compton system, the surrounding passive shielding, and the data acquisition system. As the target, it was used a 60 g ^{nat}Lu sample with 99.9% purity and with dimensions of 60×2.2 mm to minimize neutron self-shielding while maximizing capture yield. Key experimental conditions included a 76 m flight path, 160 kW beam power, 200 hours of measurement time, a neutron energy range of 1-700 eV, and an average neutron flux at the sample position of approximately $2\times10^4 \text{ neutrons/cm}^2/\text{s}$ [6].

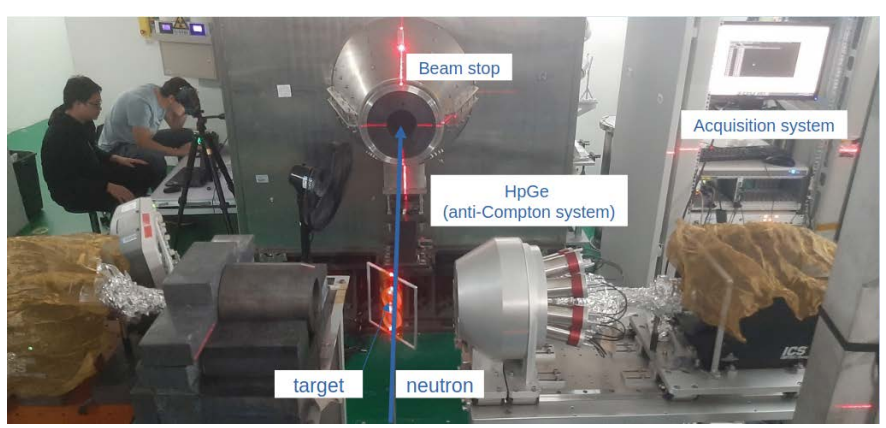


Fig. 1. Experimental setup at the ES#2 station of the CSNS Back-n White Neutron Source.

The HPGe detector was positioned at a distance of 20 cm from the target at an angle optimized to maximize the solid-angle coverage while minimizing scattering contributions from the surrounding environment. The detector was surrounded by a BGO (bismuth germanate) anti-Compton suppression system, which effectively reduced the Compton continuum and enhanced the peak-to-total ratio of the measured γ -ray spectra. A newly integrated low-noise preamplifier ensured high-resolution performance in comparison to

previous experimental results (4.4 keV for 1173 keV) and stable energy calibration throughout the extended measurement runs. The data acquisition system employed digital signal processing electronics capable of high-speed event-by-event recording and time stamping, allowing for accurate resonance assignment, background subtraction, and coincidence analysis. Data processing was performed offline using a C++-based ROOT framework. Signals from the HPGe detector were shaped, analyzed, and recorded event-by-event for further spectrum reconstruction.

γ-ray energy calibration

 γ -ray energies were determined using a combination of point source calibrations and neutron-induced reactions within the experimental setup. Calibration was performed with standard radioactive sources including ¹³⁷Cs, ²²Na, ⁶⁰Co, and ¹⁵²Eu, which provided well-characterized γ -ray energies for accurate detector calibration. These sources were measured before the experiment to establish the energy response of detector and to verify the ADC channel conversion. Neutron-induced reactions in a NaCl sample were used to cross-check the calibration under experimental conditions and increase calibration range up to 9000 keV (Fig. 2). As shown in Fig. 2, the background (blue) is significantly lower than the sample-plus-background (black), and that the net spectrum (red) clearly resolves prominent photopeaks and single-escape peaks associated with ³⁵Cl and ²³Na. Prominent gamma peaks from neutron activation of the NaCl sample were identified and matched to their known energies to validate the calibration curve. This measurement also ensured consistency between the laboratory calibration and in-beam conditions. The calibrated energy scale was then applied to identify γ -ray peaks observed during the measurement of the ^{nat}Lu target.

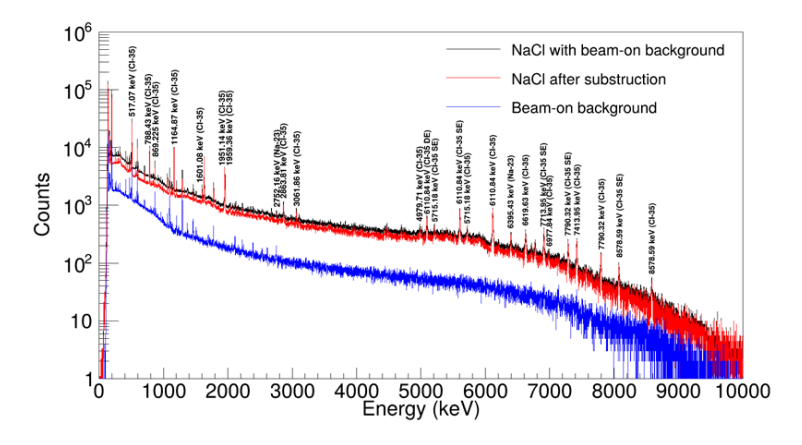


Fig. 2. Energy spectrum of the NaCl sample for energy calibration of the HpGe detector.

Fig. 3 shows the neutron energy spectra measured using HpGe detector, which recorded γ -ray energies resulting from neutron interactions with the target. γ -ray spectra for isolated neutron resonances was measured in the 1–700 eV neutron energy range, achieving sufficient γ -ray statistics up to 100 eV. The resonances corresponding to the Lu isotopes were identified using ENDF/B-VII [7], EXFOR libraries [8] and other experimental results [9–10].

In the results, it was possible to the extraction of gamma spectra from 16 resonances for the 175 Lu(n, γ) 176 Lu reaction and 10 resonances for the 176 Lu(n, γ) 177 Lu reaction, despite the low natural abundance (2.6%) of 176 Lu.

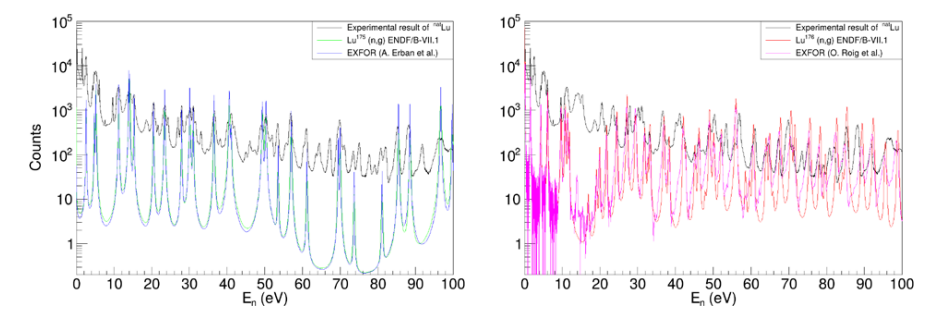


Fig. 3. Measured resonance spectrum from 1 eV to 100 eV for both isotopes, compared with the (n,γ) cross-sections of 175 Lu and 176 Lu from ENDF/B-VII and EXFOR libraries.

Full γ -ray energy spectrum of investigated region over all resonances was shown in Fig. 4. Well-resolved primary transitions attributed to 176 Lu and 177 Lu is shown in Fig. 2. The spectrum was accumulated over approximately 200 hours of beam time with neutron energies in the range 1–700 eV. The energy resolution of 6000 γ -ray was obtained to be 6.6 keV full width at half maximum.

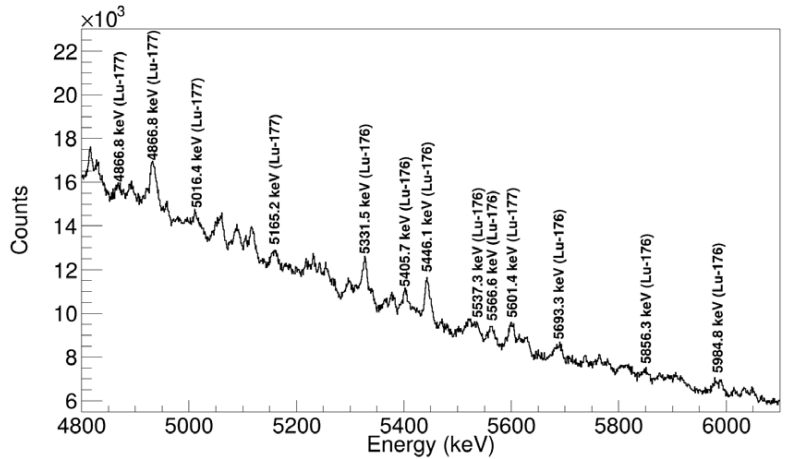


Fig. 4. Full γ-ray energy spectrum measured for the ^{nat}Lu target at the CSNS Back-n ES#2 experimental station. The spectrum was given for energy region of interest.

To analyze individual resonances, a gating method was used to isolate the relevant γ -ray energies. Fig. 5 shows the γ -ray energy spectra measured for the $^{175}Lu(n,\gamma)^{176}Lu$ reaction at six isolated neutron resonances: 2.6, 4.8, 5.2, 20.7, 23.7, and 88.5 eV.

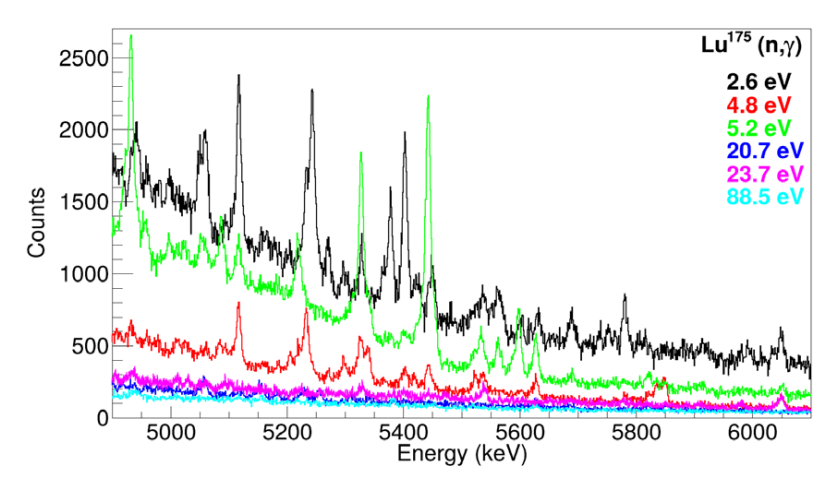


Fig. 5. γ -ray energy spectra measured for the $^{175}Lu(n,\gamma)^{176}Lu$ reaction at six isolated neutron resonances.

The spectra clearly demonstrate the variation in peak intensities from resonance to resonance in the region of interest. The prominent high-energy peaks correspond to direct transitions to low-lying levels in 176 Lu.

Discussion

Table 1 summarizes the experimental results for the energies of only 13 prominent primary gamma transitions (E_{γ}) observed for 15 neutron resonances in the $^{175}Lu(n,\gamma)^{176}Lu$ reaction.

Table 1. Measured energies of primary γ - rays (E_{γ}) and corresponding neutron resonance energies (E_n) . Values in parentheses indicate uncertainties.

E _γ (keV)	E _n (eV)			
6053.927(329)	2.6, 4.8, 13.8, 20.7, 23.7, 36, 40.6, 57			
5982.199(799)	2.6, 4.8, 5.2, 15.4, 23.7, 31, 40.6, 57			
5851.520(191)	2.6, 4.8, 5.2, 14.1, 15.4, 53.2			
5838.954(673)	4.8, 5.2, 11.2, 20.7, 36, 40.6			
5824.802(456)	4.8, 5.2, 11.2, 20.7, 27.9, 36, 40.6, 57, 73.6			
5783.612(685)	2.6, 4.8, 5.2, 11.2, 13.8, 14.1, 23.7, 27.9			
5692.059(341)	2.6, 5.2, 13.8, 15.4, 23.7, 27.9			
5573.021(587)	2.6, 11.2, 13.8, 27.9			
5418.824(762)	4.8, 15.4, 36, 40.6, 53.5			
5331.521(326)	2.6, 4.8, 5.2, 11.2, 13.8, 15.4,23.7, 27.9, 36, 40.6, 57			
5301.760(731)	2.6, 4.8, 11.2, 15.4, 31, 76.3			
5120.283(348)	2.6, 4.8, 11.2, 13.8, 15.4, 23.7, 27.9, 31, 57, 73.6			
5053.612(929)	2.6, 4.8, 13.8, 15.4, 36, 40.6, 57, 81			

The table also lists the corresponding neutron resonance energies (E_n) for each transition. These results demonstrate that the same primary gamma transitions can be populated by multiple neutron resonances and that the present measurements contribute additional data on primary transitions within this energy range.

To explain the decay pathways and the nuclear structure information contained in this measurement, the results were compared with the established level scheme for ¹⁷⁶Lu, which is shown separately in Fig. 6. The level scheme is taken from [3] and represents the evaluated low-lying states and band structure of ¹⁷⁶Lu.

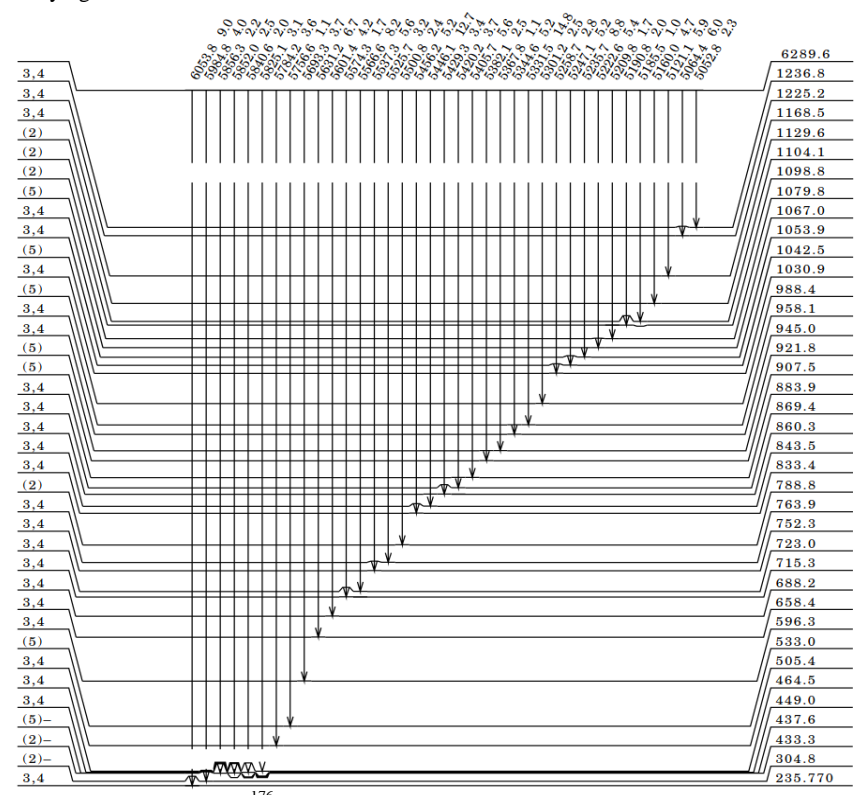


Fig. 6. Level scheme for ¹⁷⁶Lu adapted from [3] showing known low-lying states and band structure.

By mapping the measured primary gamma transitions onto this level scheme, it is possible to identify the final states populated by each transition and understand how the decay proceeds through the rotational bands. As shown in Fig. 6, most of the measured primary gamma transitions feed levels that belong to well-established rotational bands, consistent with the deformed structure of this nucleus [2]. This indicates that the compound nucleus formed through resonance neutron capture couples efficiently to the rotational degrees of freedom, in agreement with the statistical compound nucleus model. The fact that multiple resonances

populate the same final states further supports the statistical nature of the decay, where different spin-parity configurations can decay via E1 and M1 transitions to the same collective levels. Compared to earlier works which were generally limited to just a few resonances below 50 eV [1, 2] the broader resonance coverage obtained here provides datasets for examining how partial radiation widths change from resonance to resonance. This is particularly relevant for studying effects such as K-mixing [2], which can define affect transition probabilities in deformed nuclei.

Conclusion

In this work, new experimental data on primary gamma transitions in ¹⁷⁶Lu and ¹⁷⁷Lu following resonance neutron capture have been obtained using the CSNS Back-n White Neutron Source. The measurements extend the resonance energy range studied to 73.6 eV, compared to earlier experiments. The comparison with the evaluated level scheme confirms that the observed transitions are consistent with known decay pathways and the rotational band structure of this deformed nucleus. Interpretation of the full dataset, including detailed statistical analyses of partial gamma widths and possible K-mixing effects, is ongoing. Despite the low natural abundance of ¹⁷⁶Lu (2.6%), clear resonances were successfully resolved and analysis is ongoing. To further enhance the accuracy and statistical reliability of such measurements, future experiments could benefit from employing additional HPGe detectors and more advanced digital signal processing techniques. Moreover, increasing the target mass would improve counting statistics, especially for weakly populated higher-energy resonances, and such improvements can be even more effective when combined with continued development of detection systems, beam intensity upgrades, and analysis methods.

Acknowledgments

We thank the staff members of the Back-n white neutron facility (https://cstr.cn/31113.02.CSNS.Back-n) at the China Spallation Neutron Source (CSNS) (https://cstr.cn/31113.02.CSNS), for providing technical support and assistance in data collection and analysis. This work has received funding from Azerbaijan Science Foundation under grant agreement No [AEF-MGC-2024-2(50)-16/03/1-M-03].

References

- 1. O.A. Wasson, R.E. Chrien, Phys. Rev. C 2, 675–689 (1970).
- 2. F. Becvar, Ya. Gonzatko, M.E. Monte-Cabrero, S.A. Telezhnikov and Huynh Thuong Hiep, Journal of Nuclear Physics **46**, p. 392 399 (1987).
- 3. M.S. Basunia, Nucl. Data Sheets 107, 2323–2504 (2006).
- 4. F.G. Kondev, Nuclear Data Sheets 159, 1 (2019).
- H. Chen, Y. Chen, S. Fu, L. Ma et al., Nucl. Instrum. Methods Phys. Res. A 1078, 170431 (2025).
- 6. Kang Sun et al 2023 JINST 18 P04004.
- 7. https://www.nndc.bnl.gov/endf-b7.1/
- 8. https://www-nds.iaea.org/exfor/
- 9. O. Roig, M. Jandel, V. Méot, E. M. Bond et al., Phys. Rev. C 93, 034602 (2016).
- 10. A. Ebran, O. Roig, V. Méot, M. Jandel et al., Phys. Rev. C 99, 064603 (2019).

Modelling of the Forward-Backward Effect in (n,p) Reaction with Slow and Resonance Neutrons on ³⁵Cl

Yu.M. Gledenov¹, <u>I. Chuprakov</u>^{1,*}, A.I. Oprea^{1,2}, C. Oprea^{1,3}, E. Sansarbayar¹

¹Joint Institute for Nuclear Research, Dubna, Russian Federation ²Technical College "Alexandru Roman", Alesd, Bihor county, Romania ³High School "Lucian Blaga", Oradea, Bihor county, Romania

*nitro-chupa@jinr.ru

Abstract. In the nuclear reaction induced by slow and resonant neutrons on ³⁵Cl nucleus, followed by proton emission, the forward–backward effect was investigated. In the frame of the model of mixing states of compound nucleus with the same spin and opposite parities, cross sections, angular correlations and asymmetry coefficients, were evaluated. Using theoretical calculations, measurement of forward–backward effects were simulated, taking into account target properties like dimensions, temperature and proton energy loss in the target. From proton spectra, the modeled forward–backward coefficient was obtained and compared with the experimental data. From theory, the highest value of the forward–backward effect is about 0.3, but the measured one is about 30–50% lower than expected. The difference should come from the influence of temperature, target properties, background produced by a pulsed neutron source, and other factors.

The forward-backward effect, together with other asymmetry coefficients, represents an important tool in the analysis of symmetry breaking processes in nuclear reactions induced by slow and resonance neutrons generated by weak non-leptonic interaction between nucleons in the compound nucleus. In early researches, the authors had demonstrated the possibility of obtaining from experimental and theoretical data of asymmetry and spatial parity violation effects, the matrix element of the weak non-leptonic interaction.

INTRODUCTION

Theoretical and experimental investigations of asymmetry and parity breaking effects are of interest in nuclear reaction mechanisms and the structure of atomic nuclei, but more importantly, these researches can give new data on the existence of non-leptonic weak interaction between nucleons in a compound nucleus [1]. This new type of interaction comes in support of the universality of weak interaction hypothesis, first mentioned by Feynman and Gell-Mann [2].

The Frank Laboratory of Neutron Physics traditionally, from the middle of the 20th century, has investigated nuclear reactions with slow and resonance neutrons, and here, for the first time, the spatial parity non-conservation effect was measured in the capture of slow neutrons by Cadmium nuclei. The measured asymmetry of the emitted gamma quanta in the capture process was explained by the presence of the weak non-leptonic interaction [3].

The development of experimental techniques and progress in theoretical physics spurred the investigation of asymmetry and parity non-conservation effects in slow and resonance neutron-induced processes. It was also established that the weak non-leptonic process acts in the background of nuclear forces. Parity conserving nuclear forces are more than three orders of magnitude higher than weak interaction, and therefore experiments dedicated to evidence of parity breaking effects are very difficult.

In the present work, the forward-backward (FB) asymmetry effect in the (n,p) reaction with neutrons up to 600 eV was evaluated theoretically and modeled in a computer experiment. The FB effect is of interest because, together with other asymmetry and parity-breaking effects, it allows us to extract the matrix element of weak interaction using only theoretical and experimental data, without applying models of nucleons interaction in the compound nucleus [4].

ELEMENTS OF THEORY

Asymmetry FB effect was evaluated in the framework of the formalism of the mixing state of the compound nucleus with the same spin and opposite parities. In this approach, it is supposed that the asymmetry and parity non-conserving effect in neutron processes can be observed if the states of compound nucleus can be described by at least two resonances with the same spins and opposite parities [5,6].

In the simplest simple case, it is considered that the compound nucleus is described by two states, called S and P resonances, respectively. The S resonance is produced by the capture of s-neutrons with orbital momentum l=0, and the P resonance is obtained by the capture of p-neutrons with orbital momentum l=1. For (n,p) process the S and P amplitudes are respectively [5–7]:

$$f_{S} = -\frac{1}{2k}C(I, I_{z}, a_{n}, a_{zn}; J_{S}, J_{Sz})C(I', I'_{z}, a_{p}, a_{pz}; J_{S}, J_{Sz}) \times \frac{T_{S}^{n}T_{S}^{p^{*}}}{(E - E_{S}) + i\frac{\Gamma_{S}}{2}} Exp(-i\varphi_{S}), \quad (1)$$

$$f_{P} = -\frac{2\pi}{k} \sum_{\substack{j_{n}, j_{nz}, \nu_{n} \\ j_{p}, j_{pz}, \nu_{p}}} C(I, I_{z}, j_{n}, j_{nz}; J_{P}, J_{Pz}) C(I_{n}, \nu_{n}, a_{n}, a_{zn}; j_{n}, j_{nz}) C(I', I'_{z}, j_{p}, j_{pz}; J_{P}, J_{Pz}) \times$$

$$(2)$$

$$\times C(l_{p}, v_{p}, a_{p}, a_{pz}; j_{p}, j_{pz}) \frac{T_{P}^{n}(j_{n})T_{P}^{p^{*}}(j_{p})}{(E - E_{P}) + i\frac{\Gamma_{P}}{2}} Y_{\ln lv_{n}}^{*}(n_{n}^{*}) Y_{lpv_{p}}(n_{p}^{*}) Exp(-i\varphi_{P}),$$

protons with their projection respectively; l_n, v_n, l_p, v_p are the orbital momentum of the neutrons and protons with their projections; j_n, j_{nz}, j_p, j_{pz} are total momentum of protons and neutrons with their projections; J_S, J_{Sz}, J_P, J_{Pz} are the spins of S and P compound nucleus respectively with the corresponding projections; C are the Clebsch-Gordan coefficients; $T_{S,P}^{n,p}$ are the reduced amplitudes of neutron capture and proton emission with their complex conjugate; $\Gamma_{S,P}$ are the total widths in S and P states respectively; Y are the spherical functions; $\overrightarrow{n}_{n,p}$ are the unit direction vectors for neutron and proton respectively; $E_{S,P}$ are the

where $I, I_z, I', I_z, a_n, a_n, a_n, a_n$ are the spins of: target and residual nuclei, neutrons and

The f_s and f_p amplitudes are given by strong nuclear interaction and they are conserving the parity. Similar amplitudes can be written if weak non-leptonic interactions are considered. In the investigated case of FB effect, the incident neutrons are not polarized. In this case, parity breaking effects cannot be observed in the experiment. Further details on parity non-conservation effects can be found in references [4–7]. With the help of amplitudes,

energy of S and P resonances respectively; * represents the complex conjugate of a function.

differential cross section and angular correlation (W) can be obtained according to the expressions:

$$\frac{d\sigma}{d\Omega} = |f_1|^2 + |f_2|^2 + 2\operatorname{Re} f_1 f_2^* \sim W(\theta) , \qquad (3)$$

where θ is the polar angle.

Coefficient FB is defined as:

$$\alpha_{FB} = \frac{\frac{d\sigma}{d\Omega}(\theta = 0) - \frac{d\sigma}{d\Omega}(\theta = \pi)}{\frac{d\sigma}{d\Omega}(\theta = 0) + \frac{d\sigma}{d\Omega}(\theta = \pi)} \Rightarrow \alpha_{FB} = \frac{2\operatorname{Re} f_{S} f_{P}^{*}}{\left|f_{S}\right|^{2} + \left|f_{P}\right|^{2}}\Big|_{\theta = 0}.$$
(4)

From relation (3), the FB effect can be interpreted as the interference of the S and P waves in the compound nucleus. This aspect is very important because it enables all amplification mechanisms (kinematic, dynamic, structural) mentioned in [4–7]. For computer simulation, the distribution of the polar angle was obtained by the Direct Monte Carlo Method, using the differential cross section (3). The target in the first case was considered point-like and, in the second case rectangular with finite dimensions (length, width, height) [8]. Theoretical calculations and simulations were performed using the geometry from Fig. 1.

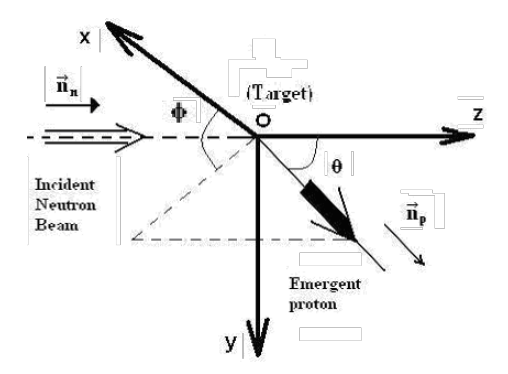


Fig. 1. Geometry of calculation and simulated experiment. Φ is the azimuth angle. Due to parity conservation azimuth angle is not appearing in the next relations.

RESULTS AND DISCUSSIONS

In the $^{35}Cl(n,p)^{35}S$ reaction with slow and resonance neutrons up to 600 eV, the theoretical FB effect was obtained by applying the Flambaum-Sushkov formalism, relation (1–4) and two-resonance approximation. Parameters of neutron resonances were taken from [9]. The expression for differential cross-section is:

$$\frac{d\sigma}{d\Omega}(E_{n},\theta) = \left(\frac{g_{S}\lambda_{n}^{2}}{4}\frac{\Gamma_{n}^{S}\Gamma_{n}^{S}}{[S]} + \frac{g_{P}\lambda_{n}^{2}}{4}\frac{\Gamma_{n}^{P}\Gamma_{n}^{P}}{[P]}\right)P_{0}(\cos\theta) + \frac{g_{S}\lambda_{n}^{2}}{4}\frac{(X_{n} - Y_{n})(X_{p} - Y_{p})\sqrt{\Gamma_{n}^{S}\Gamma_{n}^{S}\Gamma_{n}^{P}\Gamma_{n}^{P}}}{[S]\cdot[P]} \times AFB(E_{n})P_{1}(\cos\theta) + 1.4\frac{g_{P}\lambda_{n}^{2}}{4}\frac{\Gamma_{n}^{P}\cdot\Gamma_{n}^{P}}{[P]}(X_{n}Y_{n}X_{p}Y_{p})P_{2}(\cos\theta), \qquad (5)$$

$$AFB(E_{n}) = \left[(E_{n} - E_{S})(E_{n} - E_{S}) + \frac{\Gamma_{S}\Gamma_{P}}{4}\right]\cos(\Delta\phi_{SP}) - \left[(E_{n} - E_{S})\frac{\Gamma_{P}}{2} - (E_{n} - E_{P})\frac{\Gamma_{S}}{2}\right]\sin(\Delta\phi_{SP}), \qquad (5)$$

$$X_{n,p} = \pm\sqrt{\frac{\Gamma_{n,p}^{P}\left(\frac{1}{2}\right)}{\Gamma_{n,p}^{P}}}; Y_{n,p} = \pm\sqrt{\frac{\Gamma_{n,p}^{P}\left(\frac{3}{2}\right)}{\Gamma_{n,p}^{P}}}, \qquad X_{n,p}^{2} + Y_{n,p}^{2} = 1,$$

where $\Gamma_{n,p}^P\left(\frac{1}{2}\right)$, $\Gamma_{n,p}^P\left(\frac{3}{2}\right)$ are the neutron and proton partial widths; $X_{n,p}$, $Y_{n,p}$ are the reduced partial widths; $\Delta\phi_{SP}$ is the difference of phase in S and P states respectively; $P_{0,1,2}$ are the Legendre Polynomial of 0,1,2 orders, respectively.

$$\frac{d\sigma}{d\Omega} = A_0(E_n) \cdot P_0(\cos\theta) + A_1(E_n, \{X, Y\}) \cdot P_1(\cos\theta) + A_2(E_n, \{X, Y\}) \cdot P_2(\cos\theta) =
= A_0 + A_1 \cdot \left(\overrightarrow{n_n} \cdot \overrightarrow{n_p}\right) + \frac{1}{2}A_2 \cdot \left[3 \cdot \left(\overrightarrow{n_n} \cdot \overrightarrow{n_p}\right)^2 - 1\right],$$
(6)

where A_0 is the isotropic term; A_1 gives the FB effect; A_2 gives the anisotropy of angular distribution.

Applying the relation of definition (4), the FB effect is:

$$\alpha_{FB} = \frac{\left(X_n - Y_n\right)\left(X_p - Y_p\right)\sqrt{\Gamma_n^S \Gamma_p^P \Gamma_p^P \Gamma_p^P}}{\Gamma_n^S \Gamma_p^P \left[F\right] + \Gamma_p^P \Gamma_p^P \left[S\right]\left[1 + 1.4X_n Y_n X_p Y_p\right]} AFB(E_n). \tag{7}$$

From Fig. 2a and relation (4), it is clear that the presence of P_2 usually reduces the value of the FB effect. In the resonance (E_P =398 eV), the FB effect is zero and P_2 gives an anisotropy in the differential cross-section (Fig. 2b).

In Fig. 3a the cross-section of the $^{35}\text{Cl}(n,p)^{35}\text{S}$ reaction is represented. The thermal neutron calculated cross-section $\sigma(E_n=0.0253 \text{ eV})=0.453 \text{ b}$ is in agreement with experimental data [9]. For resonance energy $E_P=398 \text{ eV}$ the theoretical cross-section value also agrees with measured data and is around 80 mb. Considering the good description of the cross-section in Fig. 3b, the FB effect was evaluated. In Fig. 3b the presence and absence of P_2 , the second order Polynomial Legendre, were shown by curves 1,3 without and 2,4 with P_2 . From (7) the FB effect reaches the maximum values if $\pm X_n = \mp Y_n = \pm X_p = \mp Y_p = 1/\sqrt{2}$. Maximum FB effect is ± 0.31 . The \pm comes from the indetermination of the sign of the phase shift in the expression of reduced amplitudes T [5–7]. In the two-levels approximation the FB effect has

zero value in resonance and is changing its sign as was predicted in [5,6]. The zero value of the FB effect in resonance is confirmed experimentally in [4].

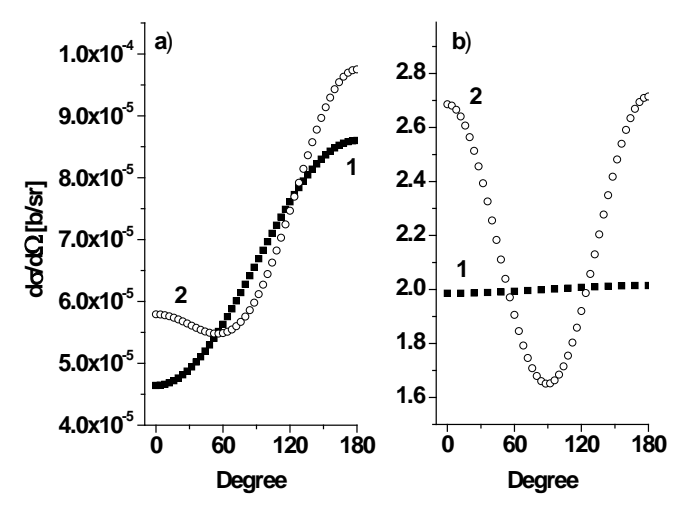


Fig. 2. Differential cross-section. a) Neutron energy $E_n = 365$ eV (α_{FB} has maximum value). $1 - \text{without } P_2(\cos\theta)$; $2 - \text{with } P_2(\cos\theta)$.

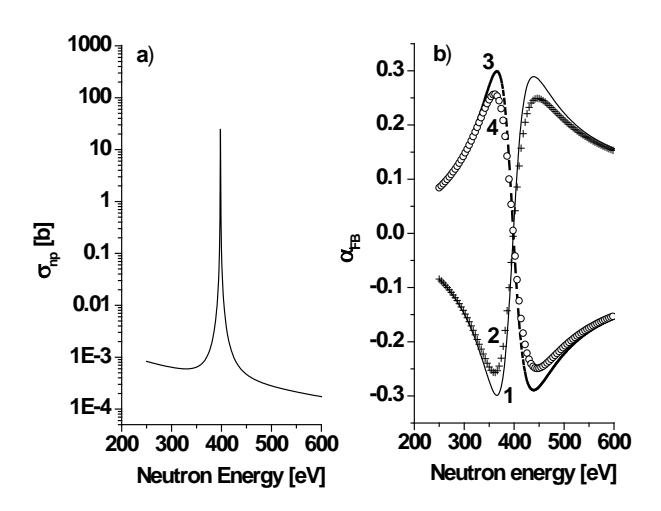


Fig. 3. a) Cross-section neutron energy dependence. b) Dependence of FB effect by neutrons energy: 1,3 without P_2 ; 2,4 with P_2 .

For the computer modeling of the FB effect, generation of polar and azimuth angles is necessary. For this reason, the angular distribution (6) will be expressed as function of $\cos\theta$. Then relation (6) becomes:

$$\frac{d\sigma}{d\Omega} \sim W(\Omega) = 1 + \alpha \cos(\theta) + \beta \cos^2(\theta) = 1 + \alpha \stackrel{\rightarrow}{n_n} \stackrel{\rightarrow}{n_p} + \beta \stackrel{\rightarrow}{(n_n \cdot n_p)^2}.$$
 (8)

Using the Direct Monte-Carlo Method, polar and azimuth angles are:

$$\theta = \pm ArcCos \left[\frac{-2 + \beta}{2(\alpha + \beta)} \left(1 \pm \sqrt{\left(\frac{-2 + \beta}{2(\alpha + \beta)} \right)^2 \pm \frac{2 + \alpha - 4r}{\alpha + \beta}} \right) \right],$$

$$\varphi = 2\pi r r'; r, r' \in [0, 1)$$
(9)

where r, r' are random numbers.

If β =0 then from (9) the FB effect is α_{FB} . Because the FB effect is conserving the spatial parity then it is not depending on azimuth angle. For this reason the azimuth angle has uniform distribution. In the modeled experiment the FB effect is defined as:

$$\alpha_{FB}^{sim} = \frac{N_F - N_B}{N_F + N_B},\tag{10}$$

where N_F and N_B are the events in the forward and backward directions respectively.

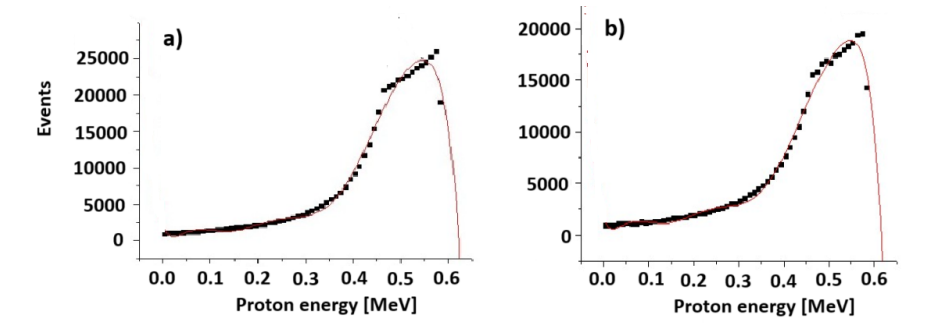


Fig. 4. Simulated proton spectra. Number of generated events N=10⁶. a) Forward; b) Backwards.

The forward events are all registered protons in the solid angle $\theta \in [0, \pi/2)$. For backward protons $\theta \in [\pi/2, \pi]$. For both cases, azimuth angle is $\varphi \in [0, 2\pi]$. Simple calculation shows that for a punctual target, the simulated FB effect is $\alpha_{FB}^{sim} = 0.5\alpha_{FB}$. If the target has finite dimensions, then the simulated effect can be obtained only by a Monte-Carlo modeling. Below are presented the results for the NaCl target with thickness 0.5 mg/cm². In

order to observe the FB effect in the experiment it is necessary that the thickness of the target be smaller than the mean free path of the protons in NaCl. Neutron attenuation in the target can be neglected, but proton loss was considered. The background created by different causes, such as neutron multi-scattering in the target and on the walls was not taken into account yet. The results are represented in Fig. 4.

Simulated forward and backward proton spectra are shown in Fig. 4a and Fig. 4b respectively. Neutron energy interval is from 300 to 400 eV, then the theoretical FB effect is $\alpha_{FB} = 0.22$ and simulated $\alpha_{FB}^{sim} = 0.15$. The percent of lost protons in the target is about 20%. At the given thickness, the theoretical value $\alpha_{FB} = 0.22$ is averaged over the (300, 400) eV neutron energy interval, and only directions with $\theta = 0$ and $\theta = \pi$ are considered. The simulated result $\alpha_{FB}^{sim} = 0.15$ is lower than theoretical one due to the average over energy, the average over the solid angle and lastly, due to the dimensions of the target and proton loss. If for a punctual target the simulated effect is half of the theoretical value, for a real target the ratio between the modeled and theoretical effect is about 0.7. Present results were obtained for the following energies, spins and parities of S and P resonances: $E_S = -180$ eV; $E_P = -398$ eV; $E_P =$

CONCLUSIONS

The FB effect in the 35 Cl(n,p) 35 S reaction induced by slow and resonance neutrons was investigated. Cross section, angular distribution and the FB coefficient were evaluated within the framework of the Flambaum-Sushkov theory using two-levels approximation. Theoretical results of angular correlations were used in the computer modeling of the FB effect taking into account the finite dimensions of the target and proton loss. The ratio between simulated and theoretical effects is about 0.7, which is an important result in the analysis of experiments.

REFERENCES

- 1. N. Tanner, Phys. Rev., Vol. 107, p. 1203 (1957).
- 2. R.P. Feynman, M. Gell-Mann, Phys. Rev., Vol. 109, p.193 (1957).
- Yu.G. Abov, P.A. Krupchitsky, Yu.A. Oratovsky, Phys. Lett., Vol. 12, Nr. 1, p. 25 (1964).
- Yu.M. Gledenov, R. Machrafi, A.I. Oprea, V.I. Salatski, P.V. Sedyshev, P.I. Szalanski, V.A. Vesna, I.S. Okunev, Nucl. Phys. A, Vol. 654, p. 943 (1999).
- 5. V.V. Flambaum, O.P. Sushkov, Nucl. Phys. A412, p. 3 (1984).
- 6. V.V. Flambaum, G.F. Gribakin, Prog. Part. Nucl. Phys. Vol. 35, p. 423 (1995)
- 7. A.I. Oprea, C. Oprea, Yu.M. Gledenov, P.V. Sedyshev, C. Pirvutoiu, D. Vladoiu, Romanian Reports in Physics, Vol. 63, Nr. 2, p. 357 (2011).
- 8. O. Sima, Monte-Carlo Simulation of Transport of Radiation, All Publishing House, Bucharest, Romania (1994) (in Romanian Language).
- S. Mughabghab, Atlas of Neutron Resonances and Thermal Cross Sections, Z=1-100, ISBN-13:978-0-444-52035-7, ISBN-10: 0-444-52035-X, Elsevier Science, (2006).

Measuring the B^{nat}(n,tot) Reaction as an International Standard

Ignacio DURÁN

¹IGFAE - Universidad de Santiago de Compostela (SPAIN)

INTRODUCTION

The final accuracy of the evaluations relies on the quality of the experimental datasets being used. But the quality of the experimental datasets relies on the quality of the standards used as reference. Historically, the principal international standards are a few constants at thermal point (the so called TNC table), being other Nuclear Data Standard values referred to. Big improvements have been done in the last decade, after the IAEA launched an international project for the "Maintenance of the Neutron Cross-Section Standards", adopting the upgraded version of the GMAP code from ENDF/B. The TNC, besides the specific neutron cross-sections of light elements (H, Li⁶ and B¹⁰), have a special treatment in the R-matrix procedure, and the final uncertainties in the whole matrix rely on the accuracy of these selected primary Standards. Present Nuclear Data Standards (IAEA NDS) are those collected in the paper by A.D. Carlson et al in 2017 [1], where it is explained how the TNC table together with the specific neutron cross sections of light elements (H, Li⁶ and B¹⁰), play a relevant role in the whole Nuclear Data Standards evaluation. Both sets have a special treatment in the R-matrix analysis so that the final uncertainties of the whole matrix rely on the accuracy of these primary standards.

Mention must be made of the fact that these TNC – which include (n,f), (n,γ) and (n,el) reactions – cannot be directly measured as "absolute", trailing so an USU (Unknown Systematic Uncertainty) that cannot be removed by statistical analysis [2]. New inputs are needed to increase the quality of this international effort and one of the most sensitive points is the standard value at thermal point of the $B^{10}(n,\alpha)$ reaction, which experimental uncertainty depends on the acknowledge of the flux of the used neutron source. So that, looking for an absolute Standard around thermal an near-epithermal energy region, the $B^{nat}(n,tot)$ cross section is well suited because it can be accurately obtained from a neutron transmission experiment, as will be explained here below, based on integrating the cross-section function over a wide energy interval. The high accuracy of this integration method relies in two assumptions: the $\sigma(E_n)$ function has a well-known mathematical shape in a wide range covering the integration limits; and the neutron source flux function, even unknown, remains stable during the experiment. The interest in measuring the $B^{nat}(n,tot)$ reaction as a way to improve the $B^{10}(n,\alpha)$ standard is discussed in this work. The involved (n,el) reactions define the uncertainty limit, nevertheless.

THE CROSS-SECTION BEHAVIOUR AT LOW ENERGIES

Let us define the thermal energy range from 20 meV to 60 meV (around the thermal point, at 25.3 meV, equivalent to a neutron velocity of 2200 m/s, taken as the Maxwellian mean value for neutrons in equilibrium with the target nuclei at 293.58 K (20.43 °C). Let us

call the near-epithermal range above this thermal range up to few eV. As a matter of fact, the behavior of both the $B^{10}(n,tot)$ and the $B^{10}(n,\alpha)$ cross sections in this energy region is extremely close to linear in log-log scale, staying like this up to above 5 eV (see [3] and references therein). Then, we can take as mathematical shape: $\sigma(E_n) = a \cdot E_n^b$.

Where, working in barn and eV, we have:

$$a = \sigma_0 / 0.0253^b = \sigma(1eV)$$
 and $b = \log (\sigma(E_1) / \sigma(E_2)) / \log (E_1/E_2)$,

being E_1 and E_2 any two values of the neutron energy inside this linear range $(E_2 > E_1)$.

Note that b = -0.5 for B¹⁰(n,tot), where the 1/v law is strictly followed at $E_n < 5$ eV, while differs from -0.5 as E_n increases, and, for other nuclei, as the atomic number increases.

Then

$$\sigma(E_{\rm n}) = \sigma_0 \cdot (E_{\rm n} / 0.0253)^b$$

and its exact integral in the E_1 to E_2 interval is easily obtained:

$$I_{(E2-E1)} = \sigma_0 \cdot (E_2^{(b+1)} - E_1^{(b+1)}) / (0.0253^b \cdot (b+1)),$$

becoming: $I_1 = I_{(60-20)} = \sigma_0 \cdot (0.06^{(b+1)} - 0.02^{(b+1)}) / (0.0253^b \cdot (b+1)).$

That is to say that the integral values in the thermal energy region are parametrized by two and only two parameters, as long as the shape of the cross section is linear in log-log scale.

B¹⁰(n.tot) AS AN IDEAL STANDARD

 $B^{10}(n,\alpha)$ detectors are very often used to make a direct measurement of the neutron fluence in an experimental setup. Therefore, it is necessary to know its cross section very accurately since any measurement referred to a standard is limited in accuracy to that of the standard.

Allan Carlson, in [4], when considering a cross-section value as a physical quantity, said that an idealized standard should have the following characteristics:

- It should be possible to use the nuclide in elemental form, be chemically inert and not radioactive.
- It should be easy to fabricate into various shapes.
- It should be readily available; not expensive.
- Monotopes are preferred.
- It should have few (or no) other channels that could cause interference with the reaction of interest.
- In the standards energy region, the cross section should be large with a minimal amount of structure.

It is worth noting that ${\bf B}^{10}+{\bf n}$ reactions are very close to fulfil these idealized requirements. Moreover:

✓ Their cross-section shape follows perfectly the 1/v law up to 5 eV, at least. So that, we can use its mathematical parametrisation, and its exact integral in the thermal energy region (20 to 60 meV) is then easily obtained.

- ✓ $B^{10}(n,\alpha)$ is IAEA standard from 25.3 meV to 1 MeV. At thermal point the standard value in the Carlson *et al.* NDS18 paper is 3844(31) b and so the integral in the thermal range (20 to 60 meV) is 127.1(1.0) b·eV. These uncertainties in the Standards are dominated by USU (0.8%), what is relatively high if one considers that we are dealing with a primary standard. In any case, the evaluation of the $B^{10}(n,\alpha)$ thermal value is tightly tied to the U5(n,f) value in such a way that any improvement in the $B^{10}(n,\alpha)$ accuracy will produce a decrease of the TNC's associated uncertainties.
- \checkmark B¹⁰(n, α) can be accurately deduced from B^{nat}(n,tot), as it is explained here below.

B¹⁰+n reactions at thermal and near-epithermal energies show only three channels: one is the elastic scattering, and the other two are neutron capture processes, that are followed, one by an alpha emission and the other by an alpha plus a gamma.

These two alpha channels can be evaluated as one only reaction, $B^{10}(n,\alpha)$, as their Q-values are close to each other (2.70 and 2.31 MeV, respectively) so that the detection efficiency of both alphas is very close. On the other hand, the elastic channel cross section is very low (around 2.2(0.5) b), interfering little with the alpha's channels.

Otherwise, natural Boron is composed of only two isotopes: $B^{10}(19.9\%)$ and $B^{11}(80.1\%)$, being the $B^{11}(n,tot)$ cross section dominated by the (n,el) one of 5.1(2) b without any contribution to the alpha's channels. All in all, the correction by the different elastic channels in a $B^{10}(n,tot)$ measurement should contribute with less than, let us say, 7(3) b, leading to an uncertainty component at thermal point below 0.08% when the (n,α) cross section is obtained from subtracting the (n,el) components from the (n,tot). This uncertainty increases as the cross section drops, being around 0.8% at 1 eV, nevertheless. Concerning the effect of impurities in the sample, their only effect at these energies should be in the (n,el) channel, what can be easily kept as negligible.

Taking into account these very specific behaviour of the $B^{10}+n$ reactions we can see that one transmission experiment to determine very accurately the $B^{nat}(n,tot)$ cross section will lead to a better knowledge of the $B^{10}(n,\alpha)$ cross section in the thermal range. Moreover, its cross section gives high values in the thermal range and its shape is experimentally well known, without significant deviation from the 1/v law up to above 5 eV.

When using natural Boron as measuring sample for the (n,α) reaction, its cross-section value at thermal point is directly related with the B^{10} one, by just the isotopic ratio, i.e., 0.199. There are in EXFOR four experiments giving $B^{nat}(n,\alpha)$ at thermal point, and their mean value is 762.6(2.0) b, which give us a corresponding value for $B^{10}(n,\alpha)$ of 3832(10) b, in perfect agreement with the IAEA Standard value.

In consequence, it is worth adopting B^{nat}(n,tot) in the thermal region as Standard, because it is still very close to the definition of an "idealized standard" and so a transmission experiment should provide an absolute measurement that can be done in several facilities all around the world. Obviously, performing experiments at different facilities will lead to a better knowledge of eventual systematic errors, reducing so USU.

SCHEME OF A POSSIBLE B^{nat}(n,tot) EXPERIMENT

The target is to improve previous experiments measuring the B^{nat}(n,tot) cross section in the thermal and near-epithermal energy range, by using few thin samples, and one analysis based on integral values. A filter box with capacity for several B^{nat} foils should allow

measuring the beam attenuation for several sample thickness, as well as to make more uniformly distributed the in-beam B^{10} mass.

A reliable flux monitor will be used to measure the transmission changes after inserting different samples in the box filter. Both the samples and the beam monitor must cover the whole beam profile. The distance from the samples to the flux monitor should be big enough to minimize the number of scattered neutrons arriving to the beam flux monitor.



Every detector to be used as beam monitor has its own detection efficiency, ε , which is known with a certain uncertainty, that can be not negligible. Nevertheless, this source of uncertainty can be overcome doing relative-attenuation measurements as described below. In the thin-sample approximation, for any sample thickness, x, the initial neutron flux, Φ , is attenuated:

$$\Phi' = \Phi \cdot \exp[-\mu \cdot x]$$
, with the attenuation coefficient being: $\mu = \sigma_t \cdot \rho \cdot N_A / A$,

where σ_t is the $B^{nat}(n,tot)$ cross section, ρ is the sample density, A the mass number, and N_A the Avogadro's number (multiplied by 10^{-28} to get σ_t in barn).

Let $R(E_n)$ be the counting rate in the beam flux monitor without any sample in the filter box, and $R'(E_n)$ the reduced one when a thin sample (of thickness x) is added. Obviously, these counting rates depends on the efficiency of the flux monitor as well as in the beam flux, but doing the quotient $R'(E_n) / R(E_n)$, both Φ and ϵ cancel and we have:

$$R'(E_n) / R(E_n) = \exp[-\mu \cdot x] = \exp[-\sigma_t(E_n) \cdot \rho \cdot x \cdot N_A / A] = \exp[-C \cdot \sigma_t(E_n)],$$

where C is a constant (self-explained), so that the quotient of the counting rates only depends on $\sigma_t(E_n)$. Inverting the ratio, we have:

$$R(E_n) / R'(E_n) = \exp[C \cdot \sigma_t(E_n)]$$
, and then:

$$\sigma_{t}(E_{n}) = (1 / C) \cdot \ln[R(E_{n}) / R'(E_{n})].$$

This $B^{nat}(n,tot)$ cross section becomes so an absolute measurement that, eventually, can reach uncertainties well below 1%. It can be proposed as an absolute reference which, therefore, should improve the $B^{10}(n,\alpha)$ standard, and so other standards consequently related to it. Should the counting-rates statistical uncertainty be small enough, the cross-section uncertainty is dominated by both the sample parameters and the accuracy of the E_n calibration.

It is worth mentioning that the fact of assuming the exact 1/v behaviour of the $B^{nat}(n,tot)$ cross section allows to extrapolate to the thermal point those points measured at higher energies, even well above the 20-60 meV thermal range, leading so to lower statistical uncertainties. Once adopted the exact 1/v behaviour for the $B^{nat}(n,\alpha)$ XS, it becomes easy to obtain integral values between any limits, E_1 and E_2 , that will depend only on the $\sigma_t(th)$ thermal value. Then, we have [in eV and barn]:

$$I_{(E2-E1)} = 2 \cdot \sigma_t(th) \cdot (\sqrt{E_2} - \sqrt{E_1}) \cdot \sqrt{0.0253}$$

and so, the cross section at thermal point becomes related to any integration interval:

$$\sigma_t(th) = I_{(E2-E1)} / (2 \cdot (\sqrt{E_2} - \sqrt{E_1}) \cdot \sqrt{0.0253})$$

and, inversely, once known the $\sigma_1(th)$, the thermal-range integral, I_1 , can be analytically obtained. It is important mentioning that this feature of the Boron cross section is not shared by the (n,f) cross section of heavier nuclei, whose exact 1/v behaviour is not accurately sustained

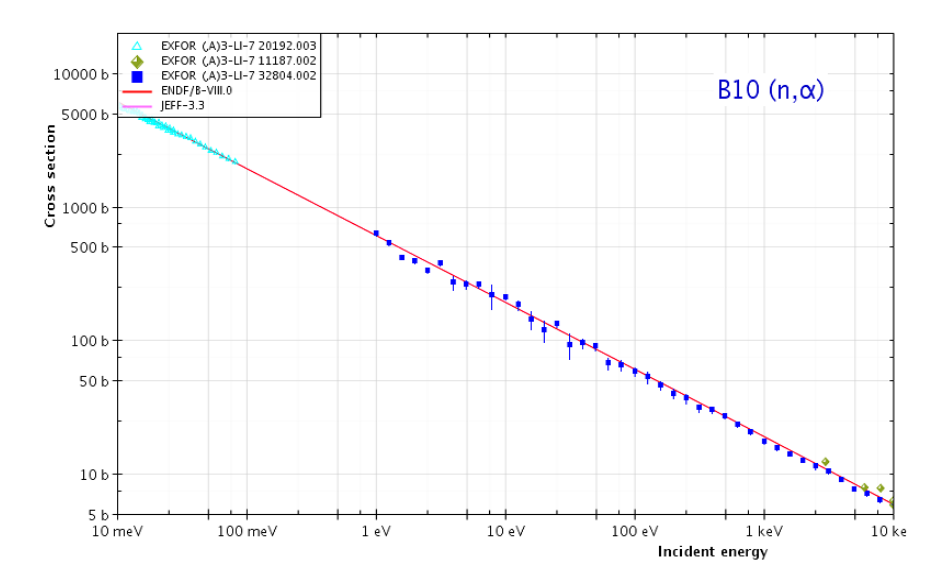


Fig. 1.- EXFOR-available high-resolution ToF datasets for the $B^{10}(n,\!\alpha)$ reaction.

The final goal is to improve the standard value of $B^{10}(n,\alpha)$ whose evaluated thermal value in the NDS-18 is 3844(31) b. Some evaluated libraries still show the former NDS-09 value of 3842.4 b. The only high-resolution experimental file in EXFOR (Prosdocimi 1967) reports a value of 3836(9) b, and the analytical value by integration in the thermal energy range assuming the 1/v behaviour give us a value of 3835(5) b. Therefore, it is of interest

improving the $B^{10}(n,\alpha)$ standard by reducing its uncertainty. The value obtained from (n,tot) - (n,el) should help to get a more precise knowledge of this standard, being the largest uncertainty component that of the $B^{10}(n,el)$ reaction (around 0.2 b).

In Fig. 1 are shown the few high-resolution experimental datasets retrieved from EXFOR for the $B^{10}(n,\alpha)$ reaction, and in Fig. 2 are those for the $B^{nat}(n,tot)$ reaction, for which there is only one evaluated library (note the big discrepancy above 1 eV).

CONCLUSIONS

The $B^{10}(n,\alpha)$ reaction is an IAEA Standard worth of being refined. This is a challenged issue when measured in a ToF experiment because the uncertainties coming from the neutron flux spectrum. The $B^{nat}(n,tot)$ reaction can be measured instead in a transmission experiment, leading to an indirect measurement of the $B^{10}(n,\alpha)$ channel with relatively low uncertainty, as long as the involved elastic channels have a low cross section. It can be very accurately measured as an absolute magnitude by using the ratios of cumulative thin samples, and based on integrating the cross-section function over a wide energy interval. In consequence, it is worth adopting $B^{nat}(n,tot)$, besides $B^{10}(n,\alpha)$, as Standard in the thermal region, because it is still very close to an "idealized standard", even though its isotopic admixture of B^{11} .

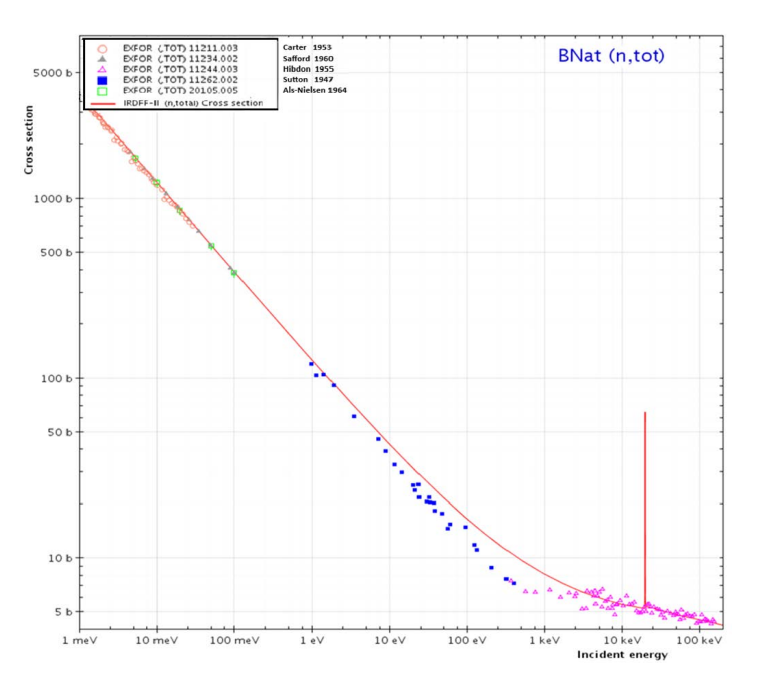


Fig. 2.- EXFOR-available high-resolution ToF datasets for the Bnat(n,tot) reaction. Note the lack of datafiles between 100 meV and 1 eV, as well as the lack of evaluated data other than IRDF.

The here proposed method is based on measuring ratios of different filter thickness, that are independent on both the flux monitor efficiency and the flux-function shape. Moreover, the XS value at thermal point can be deducted from integral values, even using integration limits relatively higher than the standard thermal point.

REFERENCES

- 1. A.D. Carlson, V.G. Pronyaev, R. Capote et *al.*, "Evaluation of Neutron Data Standards," Nucl. Data Sheets **148**, (2018)142–187.
- 2. R. Capote, S. Badikov, A.D. Carlson *et al.*, "Unrecognized Sources of Uncertainties (USU) in Experimental Nuclear Data," Nucl. Data Sheets **163**, (2020)191–227.
- 3. Jie Liu *et al.*, "Ratios of the cross sections for the ¹⁰B(n,α)⁷Li reaction to the ⁶Li(n,t)⁴He reaction", Eur. Phys. J. A (2023) 59:106.
- A.D. Carlson, "The neutron cross section standards, evaluations and applications" Metrologia 48(2012)S328.

Assessment of Toxic Elements in Atmospheric Deposition in Azerbaijan Using Moss Biomonitoring Methods

Sh.S. Nuhuyeva^{1*}, A.I. Madadzada^{2,4}, E.A. Mammadov³, M.V. Frontasyeva⁴

Corresponding author: Shahla Nuhuyeva (shahla.nuhuyeva@adau.edu.az)

Abstract. Information from existing studies on heavy metal concentrations in mosses is an invaluable resource for international negotiations on heavy metal pollution. Results from moss studies help investigate both spatial and temporal trends of heavy metals in atmospheric sediments. Besides, these studies allow the identification of places with high levels of atmospheric pollutants that spread over large distances and heavy metals emitted from local sources. For this purpose, air pollution in the Goygol, Gedabey and Dashkasan regions of Azerbaijan was studied by moss biomonitoring using the moss species Pleurozium Schreberi and Hylocomium splendens. The presence of 44 elements was determined by neutron activation analysis (NAA), atomic absorption spectroscopy (AAS) and Particle-induced X-ray emission (PIXE). The main element associations were identified using factor analysis. Four factors were determined. Research methods are based on the application of mosses as indicators, the amount of elemental pollutants in atmospheric sediments and their suitability in mosses. Besides, it reflects the general state of atmospheric pollution in the studied areas. Distributional maps were prepared to point out the regions most affected by pollution and to relate this to the known sources of contamination.

Beside the anthropogenic influences, the lithology and the composition of the soil also play an important role in the distribution of the elements.

Keywords: moss biomonitoring; heavy metals; atmospheric deposition; pollution sources; NAA; AAS; PIXE

1. Introduction

Air pollution poses significant risks to both the ecosystem and public health. Among pollutants, heavy metals and radionuclides are especially dangerous. Recently, biomonitoring – particularly utilizing mosses – has proven effective and reliable for environmental contamination studies. Mosses, due to their lack of roots and waxy cuticles, accumulate airborne pollutants directly from the atmosphere, making them ideal bioindicators. This passive accumulation capacity allows for the detection of even low

¹Azerbaijan State Agricultural University, 262 Ataturk Ave, AZ2000 Ganja, Azerbaijan

²Nuclear Research Department, Digital Development and Innovation Agency, 20th km of Baku-Shamakhi Highway AZ1069 Baku, Azerbaijan

³Azerbaijan Technological University, Sh.I. Khatai avenue Ganja, AZ2011, Azerbaijan ⁴Joint Institute for Nuclear Research, 6 Joliot-Curie, 141980 Dubna, Russia

concentrations of toxic elements over wide areas. In Europe and other parts of the world, moss biomonitoring has become a standard tool for long-term environmental surveillance. However, in the South Caucasus region, especially in Azerbaijan, such systematic approaches are still developing. Therefore, this study contributes not only to national environmental monitoring but also enhances international datasets on transboundary air pollution.

2. Methodology

2.1 Study area

The research was conducted in three western regions of Azerbaijan – Goygol, Dashkasan, and Gadabay – occupied by industrial and mining operations. These areas are part of the Lesser Caucasus mountain range and are known for their complex geological structures and rich mineral resources, including copper, molybdenum, and iron ores. The selected regions represent a mix of anthropogenic and natural influences, making them ideal for evaluating pollution levels from both industrial and geogenic sources. Dashkasan and Gadabay host active mining enterprises, ore processing plants, and associated industrial infrastructure. In contrast, Goygol, though less industrialized, is exposed to transboundary pollution and localized emissions from transportation and small-scale activities. The regions also vary in altitude and climatic conditions, which may affect the deposition and distribution patterns of atmospheric pollutants. The presence of forests and relatively undisturbed ecosystems in some parts further enhances the suitability of these sites for moss-based biomonitoring studies. This regional diversity allows for a comparative analysis of pollution patterns and a better understanding of how local topography, human activity, and geological background influence the accumulation of toxic elements in mosses.

2.2 Moss sampling

Within the framework of the study, two moss species were selected for biomonitoring:

- Pleurozium schreberi
- Hylocomium splendens

These species are widely distributed and are recognized as effective bioindicators due to their ability to passively accumulate airborne pollutants such as heavy metals and other toxic elements. Moss samples were collected from relatively undisturbed, forested areas, situated at varying distances from potential pollution sources. Selection criteria included adequate humidity, minimal direct human impact, and the presence of homogeneous moss cover.

Samples were collected using a standardized methodology across all regions. Mosses were carefully removed from 10×10 cm areas, placed into labeled polyethylene bags, and transported to the laboratory. In the lab, samples were cleaned of extraneous materials (soil particles, leaves, insects) and dried at 40° C to prepare them for elemental analysis, following established protocols used in international moss surveys.

The variety and quantity of samples collected across different locations provided a robust dataset for comparative analyses. This sampling strategy allowed for the identification of both localized and regional pollution patterns, enhancing the overall reliability of the moss biomonitoring approach used in this study.

Table 1. Moss sample distribution by region [1,5]

Region	Total	P. schreberi	H. splendens	Both species
Goygol	86	62	18	6
Dashkasan	50	35	10	5
Gadabay	31	24	6	1

2.3 Analytical techniques

To determine the concentration of toxic and trace elements accumulated in moss samples, a combination of Neutron Activation Analysis (NAA), Particle-Induced X-ray Emission (PIXE), and Atomic Absorption Spectroscopy (AAS) was employed. These complementary analytical techniques provide high accuracy and sensitivity across a wide range of elements.

Neutron activation analysis (NAA): NAA is a non-destructive analytical technique used to determine the concentrations of multiple elements simultaneously. It was carried out at the Joint Institute for Nuclear Research (JINR), Dubna, Russia. This method is particularly suitable for detecting rare earth elements, lanthanides, and radionuclides, and it does not require complex chemical preparation of samples.

Particle-induced X-ray emission (PIXE): PIXE analysis was applied to detect elements from Na to U with high sensitivity. It involves bombarding the samples with protons to induce the emission of characteristic X-rays, which are then measured to determine elemental composition. PIXE is particularly useful for light and medium atomic number elements and is valued for its speed and minimal sample destruction.

Atomic absorption spectroscopy (AAS): AAS was used for the quantification of heavy metals such as Pb, Cd, Zn, and Cu. This technique is based on the absorption of light by free atoms in the gaseous state and is highly selective and sensitive for specific metals.

All instruments were calibrated using certified reference materials (CRMs) to ensure data quality and consistency. The accuracy of the analytical results was verified through interlaboratory comparisons and the use of internal standards. Sample preparation (e.g., drying, homogenization, and, where necessary, digestion) followed international protocols established by the UNECE ICP Vegetation Programme [2–4].

3. Data analysis

To comprehensively interpret the complex dataset obtained from the moss biomonitoring study, advanced statistical and geospatial analysis techniques were applied. The primary objective was to identify the main sources of contamination, understand their spatial distribution patterns, and assess the relationships between different elements in the atmospheric deposition.

Multivariate (factor) analysis: Factor analysis was employed as a multivariate statistical tool to reduce the dimensionality of the data and to uncover underlying patterns and associations among the measured elements. This technique helps group elements that likely originate from common sources or processes, such as industrial emissions, geological background, or combustion products. By extracting factors, the study identified four main pollution source groups influencing the moss elemental composition across the studied

regions. The robustness of factor solutions was verified through criteria such as eigenvalues greater than one, factor loadings above 0.5, and varimax rotation to achieve better interpretability.

Correlation and cluster analysis: Additional correlation analyses were conducted to explore relationships between pairs or groups of elements, offering insights into co-occurrence patterns and potential common origins. Hierarchical cluster analysis further supported the classification of sampling sites based on their elemental composition profiles, highlighting zones with similar pollution signatures and allowing differentiation between anthropogenic and natural influences.

Geographic information systems (GIS): GIS technology was integrated to visualize the spatial distribution of elements and pollution factors across the Goygol, Dashkasan, and Gadabay regions. Geostatistical interpolation methods such as Kriging or Inverse Distance Weighting (IDW) were applied to generate continuous distribution maps from discrete moss sampling points. These maps facilitated the identification of pollution hotspots and spatial trends, as well as the assessment of the influence of topographic and land-use features on pollutant deposition.

Pollution indices: To quantify pollution levels and assess environmental risks, several pollution indices were calculated, including the Contamination Pollution Index (CPI), Enrichment Factor (EF), and Geo-accumulation Index (I_geo). These indices compare measured element concentrations against regional background values or reference standards, allowing for the evaluation of contamination severity and anthropogenic impact.

Quality assurance and statistical validity: All statistical analyses were performed using recognized software packages such as SPSS, R, and ArcGIS. The dataset was tested for normality, homogeneity of variances, and outliers to ensure valid results. Where necessary, data transformations (e.g., logarithmic) were applied. The significance level was set at p<0.05 for all inferential statistics.

This integrated analytical framework combining multivariate statistics and GIS-based spatial analysis provided a comprehensive understanding of pollution sources, their impact on atmospheric deposition, and the spatial variability of toxic elements across the study areas. Such insights are crucial for environmental monitoring, pollution mitigation strategies, and policy-making [6,7].

4. Results and discussion

The comprehensive biomonitoring study using moss species Pleurozium schreberi and Hylocomium splendens revealed significant spatial variability in the concentration of heavy metals and trace elements across the Goygol, Dashkasan, and Gadabay regions. The integration of multiple analytical techniques and advanced statistical methods allowed for a robust assessment of atmospheric deposition patterns and their potential sources.

4.1 Comparative elemental concentrations

Analysis showed that moss samples collected from Dashkasan and Gadabay exhibited generally higher concentrations of several toxic and trace elements compared to those from Goygol. This trend is consistent with the presence of more intense industrial and mining activities in these regions, including active ore extraction and processing facilities. Elevated levels of copper (Cu), molybdenum (Mo), tungsten (W), lead (Pb), and cadmium (Cd) in these

areas reflect significant anthropogenic input, likely linked to metallurgical processes and fossil fuel combustion (Figure 1).

Conversely, Goygol displayed relatively lower concentrations of these anthropogenic elements but showed detectable amounts of elements typically associated with natural geological background, such as sodium (Na), scandium (Sc), lanthanum (La), and thorium (Th). These findings suggest that in Goygol, geogenic factors alongside limited industrial influence shape the elemental composition of atmospheric deposition.

4.2 Factor analysis and source apportionment

Factor analysis extracted four primary pollution source groups explaining the variance in elemental composition:

- Industrial Emissions: Characterized by elevated Cu, Mo, W, Pb, and Cd, predominantly in Dashkasan and Gadabay.
- Metallurgical Activities: Associated with Mn, Zn, Ba, and Ni, reflecting ore processing and smelting operations.
- Diesel Combustion: Indicated by the presence of antimony (Sb) and bromine (Br), which are common in vehicle emissions and diesel fuel additives.
- Natural and Geological Sources: Particularly notable in Goygol, dominated by elements such as Na, Sc, La, Th, and contributions from oil and gas combustion products (V, Ni).

These factor groupings align well with known industrial infrastructure and local geological characteristics, supporting the reliability of the biomonitoring approach and statistical modeling.

4.3 Spatial distribution patterns via GIS mapping

GIS-based spatial interpolation techniques revealed distinct pollution hotspots near industrial zones in Dashkasan and Gadabay, with pronounced elemental enrichment correlating with active mining and metallurgical sites. In contrast, Goygol exhibited more diffuse spatial patterns, reflecting the influence of transboundary pollution and natural background levels.

Mapping of scandium distribution, as shown in Figure 1, highlights the geological influence, with higher concentrations in mineral-rich areas corresponding to known lithological formations. Such spatially explicit data provide valuable insights for targeted environmental management and pollution mitigation.

4.4 Pollution indices and environmental implications

The calculated Contamination Pollution Index (CPI), Enrichment Factor (EF), and Geo-accumulation Index (I_geo) collectively suggest low to moderate pollution levels in the study areas. However, localized moderate to high contamination was observed near industrial facilities, underscoring the need for continuous monitoring and regulatory oversight.

These indices confirm that while regional air quality remains generally acceptable, specific sites require attention due to anthropogenic impacts. The identification of such zones is critical for prioritizing remediation efforts and minimizing public health risks.

4.5 Implications for environmental monitoring and policy

The study demonstrates the efficacy of moss biomonitoring combined with advanced analytical and statistical tools in characterizing atmospheric pollution in Azerbaijan. The ability to differentiate between anthropogenic and natural sources, and to spatially resolve pollution patterns, provides a strong scientific basis for environmental policy formulation.

Furthermore, the results contribute to regional and international datasets, facilitating transboundary pollution assessments and compliance with European environmental standards. Adoption of this methodology in other industrialized and populated regions of Azerbaijan could enhance national air quality management and support sustainable development goals [8,9,10].

5. Conclusions

- Moss biomonitoring effectively detects toxic elements in Azerbaijan's atmospheric deposition.
- 2. Goygol shows significantly lower pollution compared to neighboring districts.
- 3. The study aligns with European moss biomonitoring standards, supporting its integration into the "European Moss Atlas."
- 4. Eight major pollution sources identified through factor analysis.
- 5. The methodology is extendable to other industrialized and populated areas in Azerbaijan.

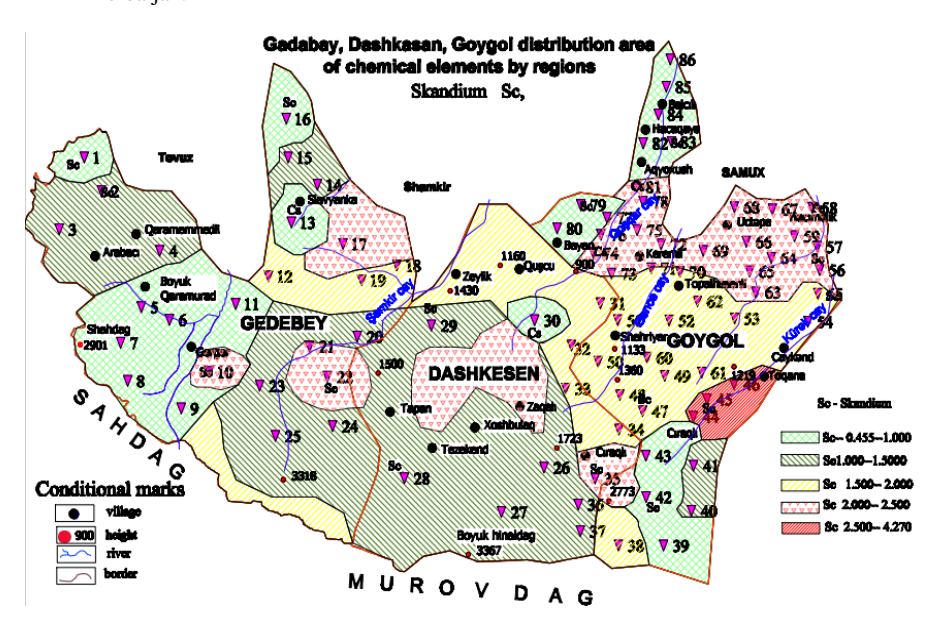


Figure 1. Distribution maps of scandium in the Dashkesan, Gadabay and Goygol regions of Azerbaijan

Acknowledgements

We thank colleagues for technical support and sample collection assistance from sector NAA FLNP JINR. Special gratitude to ISINN organizing committee for their support.

REFERENCES

- Madadzada A., Nuhuyeva Sh., Mammadov E., Frontasyeva M., Strelkova L. et al. Heavy Metal Atmospheric Deposition Study in Azerbaijan Based on Moss Technique and Neutron Activation Analysis. June 2022. Ecological Chemistry and Engineering S 29(2):143–153. DOI: 10.2478/eces-2022-0011. License CC BY-NC-ND 3.0.
- Markert B., Wappelhorst O., Weckert V., Herpin U., Siewers U., Friese K. et al. The use of bioindicators for monitoring the heavy-metal status of the environment. J. Radioanalytical Nuclear Chem. 1999; 240(2): 425-9.DOI: 10.1007/BF02349387.
- Markert B., Wuenschmann S., Fraenzle S., Wappelhorst O., Weckert V., Breulmann G. et al. On the road from environmental biomonitoring to human health aspects: Monitoring atmospheric heavy metal deposition by epiphytic/epigeic plants: present status and future needs. Int. J. Environ. Pollut. 2008; 32(4):486–498. DOI:10.1504/IJEP.2008.018412.
- Madadzada A., Badawy M., Hajiyeva S., Veliyeva Z., Hajiyev O. et al. Assessment of atmospheric deposition of major and trace elements using neutron activation analysis and GIS technology: Baku – Azerbaijan. March 2019 Microchemical Journal 147 DOI: 10.1016/j.microc.2019.03.061. https://doi.org/10.1016/j.microc.2019.03.061.
- Nuhuyeva Sh., Mammadov E. Research of the Content of Heavy Metals in the Atmospheric Precipitation of the Geygel, Dashkesan and Gedabek Districts of Azerbaijan. Bulletin of Science and Practice Scientific Journal 2021, Volume 7, Issue 6. https://www.bulletennauki.com. T.7. № 6. 2021 https://doi.org/10.33619/2414-2948/67
- 6. Al-Alam J., Chbani A., Faljoun Z., Millet M. The use of vegetation, bees, and snails as important tools for the biomonitoring of atmospheric pollution a review. Environ Sci. Pollut. Res. İnt. 2019; 26(10):9391-408. DOI:10.1007/s11356-019-04388-8
- 7. Available from: http://eco.gov.az.
- 8. Bibi, D.; T"ozsér, D.; Sipos, B.; Molnár, V.É.; Simon, E.; Tóthmérész, B. Complex Study of Air Pollution Based on Tree Species in Vienna. Air Qual. Atmos. Health 2024, 17, 417–424. [CrossRef].
- 9. Buse A., Norris D., Harmens H., Buker P., Ashenden T., Mills G. European Atlas: Heavy Metals in European Mosses: 2000/2001 Survey. UNECE ICP Vegetation. Centre for Ecology and Hydrology. 2003; 1–50. DOI: 10.1007/s10874-004-1257-0. Available from: https://www.researchgate.net/publication/226579890.
- Monaci, F.; Ancora, S.; Paoli, L.; Loppi, S.; Franzaring, J. Air Quality in Post-Mining Towns: Tracking Potentially Toxic Elements Using Tree Leaves. Environ. Geochem. Health 2023, 45, 843–859. [CrossRef] [PubMed].

Prompt Fission Neutron Spectra and Angular Distributions Measured in Narrow Windows of Fragment Masses and Total Kinetic Energies: a Puzzling Result

N. Carjan

Joint Institute for Nuclear Research, FLNR, 141980 Dubna, Moscow Region, Russia Horia Hulubei - National Institute for Nuclear Physics and Engineering, P.O.Box MG-6, RO-76900, Bucharest, Romania and LP2i Bordeaux, UMR 5797 CNRS - Bordeaux University, Gradignan, France

A. Göök

Department of Physics and Astronomy, Uppsala University, Uppsala, Sweeden

S. Oberstedt

Nuclear Data and Measurement Standards, JRC Directorate G, Nuclear Safety and Security, Geel, Belgium

A previous experiment performed at JRC-Geel on prompt fission neutrons (PFN) in correlation with fragments from spontaneous fission of 252 Cf was repeated using an improved setup and much better statistics. The experiment lasted 3 months and 68×10^6 coincident events were collected. In this new experiment, PFN spectra and angular distributions (in the laboratory system) are selected in a narrow window of fragment masses and total kinetic energies around A_L = 109 and TKE=184 MeV and A_L = 98 and TKE=173.5 MeV. In this way we have isolated (as good as possible) certain fission paths which make comparisons with theoretical models easier.

Clear deviations from a Maxwellian spectrum were found from 0.5 to 6 MeV. They consist in structures, more pronounced around the most probable energy (\approx 1 MeV). Concerning the angular distribution, deviations from a smooth curve are observed in the form of fine structures. The most prominent are around (0 $^{\circ}$), (90 $^{\circ}$) and (180 $^{\circ}$).

Even inclusive angular distributions show oscillations (at a smaller scale), since the sample of events over which the average is calculated is not large enough to completely wash out the structures present in the individual distributions.

At first look, these identified structures in the data are not compatible with the traditional hypothesis that PFN are evaporated from fully accelerated fragments, because this hypothesis predicts smooth distributions. An alternative hypothesis, in which PFN are emitted during the separation of the fission fragments at scission, is discussed since it is known to predict non-smooth PFN distributions due to the proximity of the fragments at the moment of emission.

I. INTRODUCTION

The emission of prompt fission neutrons (PFN) is essential in producing nuclear energy, since it makes the chain reaction of fissile nuclei possible [1]. Without the existence of PFN, nuclear fission would not have benefited of so much publicity in the media and of so many experimental

and theoretical investigations. It is, therefore, not surprising that the study of PFN plays an important role in the fundamental understanding of the fission process and for its applications.

In the last decade, using reactions in inverse kinematics at GSI (Darmstadt) [2, 3] and at GANIL (Caen) [4–6] perfect identification of the fission fragments in Z and A has been achieved. At GSI the fission fragments have been measured using a dedicated detector system (SOFIA). The obtained distributions of the fragment charge and mass have a resolution (FWHM) of 0.35 and 0.7 units respectively. At GANIL, the VAMOS spectrometer was used to identify the fission fragments. The obtained resolutions (FWHM) are below 0.8 mass unit and $\Delta Z/Z = 0.015$.

At present precise data are needed to elucidate hot fission topics such as the role of the octupole deformation in the pre-formation of the fission fragments [7–10], the generation of the angular momentum and the prompt γ -rays [11] or the mechanism for emission of prompt neutrons [12–14]. They could be obtained by new measurements in coincidence with the above mentioned, perfectly separated fission fragments and, if possible, for well-defined total kinetic energies (TKE). An example would be measurements of PFN angular distributions with respect to the fission axis, PFN kinetic energy spectra and PFN multiplicities.

Such selected data would facilitate the comparison with calculations by restricting the number of fission paths. Dynamical calculations of the fission process often correspond to a given fission path at a time. To compare with experimental data one has to integrate over all possible fission paths, which is rarely possible. Moreover, non-inclusive data are expected to reveal new features that are washed out when averaging over many fission paths.

The ideal experiment mentioned above has no chances to be performed soon since it requires an extremely large statistics and a very complex experimental setup. Instead, in the present study, precise PFN data for ²⁵²Cf(sf), obtained at JRC-Geel in coincidence with fission fragments having well defined masses and TKE's, will be presented. In this way, a narrow bunch of fission paths is selected experimentally.

II. WHAT DO WE KNOW ABOUT THE PFN EMISSION MECHANISM

The main properties of the fission neutrons (their multiplicity as well as their angular and energy distributions) have been initially measured in the frame of the Manhattan project [15, 16], re-measured in the 1950's [17, 18] and more precisely measured in the 1980's [19]. Much needed historical reminders were published recently [20, 21].

These properties are:

- 1) an almost Maxwellian distribution of the fission neutron energies and
- 2) an angular distribution with respect to the light fragment direction asymmetrically peaked at 0° and 180° (i.e., $v(0^{\circ})/v(180^{\circ}) > 1$).

These observed properties led to the explanation that fission neutrons are evaporated from *moving fission fragments* (this was the terminology at that time). Nowadays, to make the calculations simpler, *fully accelerated fragments* are used. The fact that Weisskopf's nuclear evaporation theory [22] existed at that time may have influenced this choice. As a result, what we observe is a kinematic anisotropy in the laboratory system that originates from an (almost) isotropic center of mass (c.m.) emission, the Maxwellian spectrum simply reflecting the fragments' temperature.

Strange enough, nobody has claimed this explanation. Today it is referred to as "Los Alamos" or "Madland-Nix" model, although this work was published 30 years later [23] .

The emission is, therefore, supposed to occur long after the division of the fissioning system into two fragments: it takes $\approx 10^{-20}$ sec to reach 90% of TKE and $\approx 10^{-18}$ sec to

evaporate a neutron if the temperature is ≈ 1 MeV. Comparing to a typical nuclear (Fermi energy) time-scale ($\approx 10^{-22}$ sec) these are long times. We could have expected another type of emission (e.g., dynamical) to occur before. Moreover, deviations from a standard evaporation spectrum [23–25] or from an isotropic emission in the c.m. [26, 27] have been constantly observed but, in spite of this, the evaporation hypothesis has not been questioned. On one side, its simplicity was a strong argument in keeping it. On the other side, there was apparently no other way to explain the strong correlation between the direction of emission of PFN and the fission axis, besides the kinematic anisotropy.

The first challenge of the evaporation hypothesis came only 10 years ago when it was shown [28] that a neutron emission during the neck rupture can likewise explain the observed PFN characteristics: not only the direction of emission (mainly along the fission axis) but also the spectrum and the multiplicity. So there are, at present, two opposite mechanisms that explain the same data.

The present study represents a second challenge to the evaporation hypothesis; this time coming from the experimental side. As it will be shown, our exclusive PFN distributions exhibit fine structures. This is not compatible with the traditional hypothesis that PFN are evaporated from fully accelerated fragments.

III. A NEW EXPERIMENT FOR ²⁵²CF(SF)

An older study of ²⁵²Cf(sf) [29] was repeated using a novel setup. In Ref. [29] there was only one liquid scintillator neutron detector placed along the normal to the target. To limit the energy loss in the target, fission events with large angles between the fission axis and the neutron detector were rejected, leading to a limitation of the effective solid angle. In the new experiment six neutron detectors, with an azimuthal angular distance of 60 degree, were placed around the chamber allowing measurements with good mass resolution at any angle with respect to the fission axis. The use of a position-sensitive ionization chamber allows the event-by-event determination of the angle between the fission axis and the neutron detected in any of the neutron detectors.

In this way the angle between the detected neutron and the target normal can be decoupled. This innovation has several advantages over the standard Frisch-grid ionization chamber (FGIC) setup. First of all, it allows us to extend the range that the PFN angular distribution can be measured to also include events with very large angles between the fission axis and the detected neutron. In addition the resolution is greatly improved. The angular resolution of the position sensitive chamber is 7 degree (FHMW) with respect to an arbitrary axis in space, while with a standard FGIC only the cosine of the fission axis angle with the target normal is determined with $\approx 5\%$ resolution (FWHM). In the present experiment the resolution of the PFN angular distributions are limited by the size of the neutron detectors only.

The experiment was performed at the European Commission Joint Research Centre in Geel, BE. An illustration of the setup can be found in Fig. 1. A position-sensitive twin FGIC served as fission-fragment detector [30]. The fission detector is capable of simultaneously determining the fission-fragment mass and TKE via the double-kinetic-energy (2E)-technique and the orientation of the fission axis in 3D space. A $^{252}\mathrm{Cf}$ source consisting of a 5 mm diameter circular spot deposited on a 250 nm thick nickel backing and fission strength of $\sim\!800$ fissions per second was placed on the common cathode of the FGIC. The ionization chamber exhibits an intrinsic energy resolution better than 0.6 MeV. Accounting for energy loss in the target and backing, the total kinetic energy (TKE) resolution is approximately 1.5

MeV [31]. Methane gas (CH4), with a purity of 99.9995, was utilized as the counting gas. Pulse height defect in the counting gas was corrected by adjusting parameters to align with evaluated average light and heavy fragment masses and mean TKE [32]. Mass calibration was confirmed by measuring the fragment-mass distribution in coincidence with several isomeric γ -decay lines in an array of cerium-doped LaBr₃ detectors. The variation in the average masses of the light and heavy pre-neutron emission fragments was less than 0.25 u. The pre-neutron emission mass resolution was determined to be 4.9 u (FWHM) [33].



Fig.1. The experimental setup from behind the neutron detector array.

For neutron detection six proton-recoil scintillators of the type EJ-301 were used. The scintillation detectors were of cylindrical shape, with diameters of 101.2 mm and heights of 50.8 mm. Pulse-shape discrimination was used to select neutrons in the mixed field of neutrons and γ -rays. A minimum energy deposition was imposed corresponding to neutron energy of 0.5 MeV. The neutron detectors were placed in a circle at a nominal distance of 605 mm from the ^{252}Cf source. The exact distance of each detector was measured with an accuracy of 0.2 mm. Each detector axis made an angle of 22.5° with the target normal and was equidistantly spread out in the azimuthal angle. The neutron energies were determined using time-of-flight, the combined timing resolution of the FGIC and neutron detector was 1 ns (FWHM). The energy-dependent neutron detection efficiency was determined from the ratio

of the observed spectrum, without any selection of fission fragment mass and TKE, to the ENDF/B.VII-1 [34] evaluation of the 252 Cf(sf) PFNS.

The measurement lasted about three months, and a total of about 10^8 fragment neutron coincidences were collected. The determination of the angular distribution of the prompt neutrons, relative to the direction of motion of the fragments, was determined as described in ref. [30]. Only those events are included in the analysis, if the fission axis is within a cone with an opening angle smaller than 72.5^0 relative to the target normal. The fission fragment detection efficiency was determined by measuring the isotropic angular distribution of fission fragments around each neutron detector axis without requiring any coincidence. The angular resolution of the fission axis was 7^0 (FWHM). Accounting for the opening angle of the neutron detectors an angular resolution of 10^0 (FWHM) was obtained.

IV. PFN SPECTRA AND ANGULAR DISTRIBUTIONS IN COINCIDENCE WITH WELL DEFINED FISSION FRAGMENTS

The results of the new improved experiment are shown in Figs.2–3.

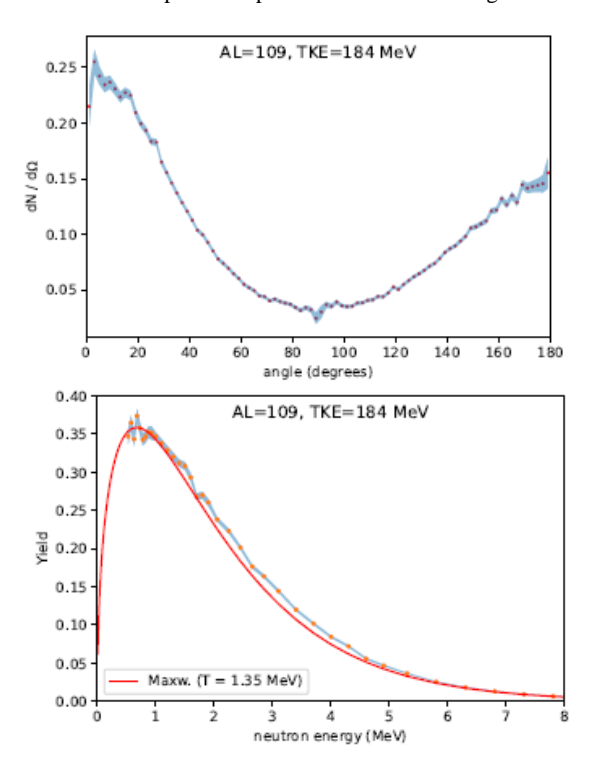


Fig.2. Measured angular distribution (upper picture) and energy spectrum (lower picture) of PFN for a given mass ratio (A_L =109) and the corresponding total kinetic energy (TKE=184 MeV) in the reaction 252 Cf(sf).

In Fig.2 the fragments are selected in windows around the most probable fragment mass, $A_L = 109 \pm 0.5$, and the corresponding most probable TKE = (184 \pm 1) MeV. The statistics is, therefore, the highest among all fragmentations.

The uncertainty is marked by the blue ribbon. In the angular distribution presented in the left frame, most of the fine structures are statistically significant. The most prominent are around (0^0) , (90^0) and (180^0) but slower oscillations around the smooth curve appear also between 20–60 degrees and 120–160 degrees. If the former structures coincide with the least statistical accuracy, the latter cover a domain with negligible errors.

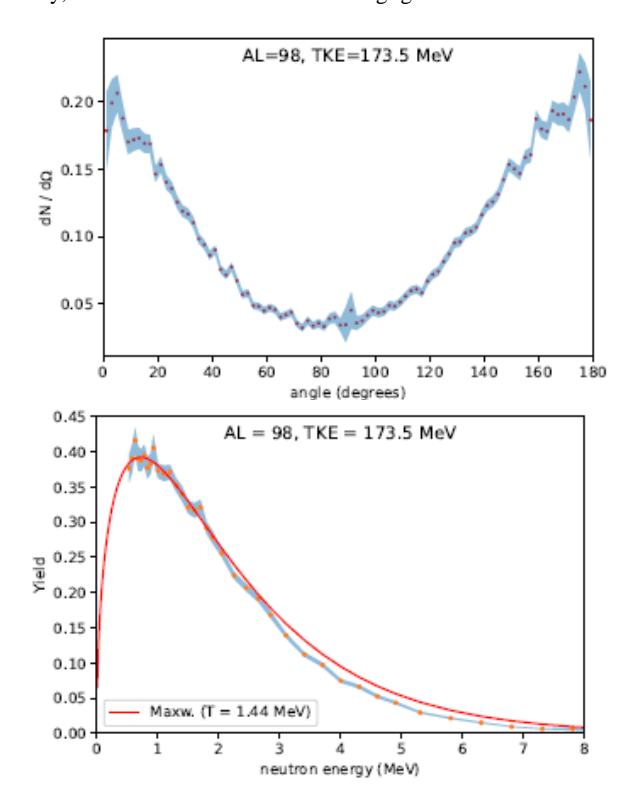


Fig.3. Measured angular distribution (upper picture) and energy spectrum (lower picture) of PFN for a given mass ratio (A_L =98) and the corresponding total kinetic energy (TKE=173.5 MeV) in the reaction 252 Cf(sf).

The 2nd fragmentation (98/154) presented in Fig.3 is the more asymmetric. The neutrons emitted in the direction of the heavy fragment have a slightly higher yield. It is worth noticing the similarities between the structures in both cases, i.e., $A_L = 98$ and 109.

In the corresponding PFN spectra (right frames of the same figures) deviations from Maxwellian were found from 0.5 to 6 MeV. The most striking are the wiggles around the

most probable energy (\approx 1 MeV) that are also similar in the two cases. The temperature values (T) were fitted to the data in order to provide a smooth background for comparison.

Not much room for doubts is left: in all distributions, there are similar deviations from the smooth curves, which are not expected if all neutrons were evaporated. Although many different evaporation codes have been extensively used during the last half-century to estimate PFN spectra and angular distributions, these new features disclosed by our data have not been foreseen.

Summarizing, structures that cannot be explained by statistical fluctuations have been observed for the first time in this kind of measurement. This has been made possible by the use of an innovative technique to determine angular distributions of prompt particles in fission. The technique allows us to combine a large solid angle of acceptance with a high angular resolution. This technique also allows us to combine it with a selectivity in both mass and total kinetic energy. Measurement of such a high number of correlated fission observable on an event wise basis is to our knowledge a first time achievement.

In the next section we will present an alternative mechanism for the emission of prompt neutrons during fission, which leads to non-smooth distributions.

V. AN ALTERNATIVE MECHANISM

Concerning the alternative to the evaporation from fully accelerated fragments, there has been only one hypothesis extensively discussed, namely the dynamical emission during scission.

The accepted mechanism for scission neutron (SN) emission is the non-adiabatic coupling between the neutron degree of freedom and the rapidly changing neutron-nucleus potential [35, 36]. It takes place during the scission process i.e., from the neck rupture at finite radius, r_{min} , to the absorption of the neck stubs by the fragments when they are separated by a distance d_{min} along the z-axes.

This idea was recently developed quantitatively in the frame of a dynamical quantum-mechanical microscopic model. In the following we will call it DSM (dynamical scission model). Time dependence was introduced through the time-dependent Schrödinger equation (TDSE) with a time-dependent potential (TDP) [37, 38].

This allows a short but finite transition time, ΔT , to be considered. Realistic values for it are around 10^{-22} sec. The neutrons present in the fissioning nucleus just before scission evolve in time and quickly find themselves in a post-scission potential, where they are described by wave packets with some components in the continuum (hence partially released). These unbound parts of the neutron wave packets $|\Psi_{em}\rangle$ will leave the nucleus and can be used to estimate SN observables.

An example of calculated PFN angular distributions is represented in Fig. 4. They display weak oscillations (from 50^0 to 150^0) that are the sign of scattering of neutrons on the just born fragments [12]. The maxima and minima are typical for a non-monotonic deflection function.

To obtain the kinetic energy spectrum for a fixed mass asymmetry, one has to sum the single spectra over all occupied states and all Ω values [39]. It is a finite weighted sum of individual quasi-maxwellian distributions with different mean values and widths. For this reason the result cannot be smooth.

Fig.5 shows this total scission-neutron spectrum calculated for 236 U and the corresponding PFN spectrum measured in the reaction 235 U(n,f) [41]. Two typical evaporation

spectra [42] characterized by nuclear temperatures Temp = 1.0 and 0.9 MeV are also plotted for comparison. The evaporation spectra and the SN histogram are normalized to the data.

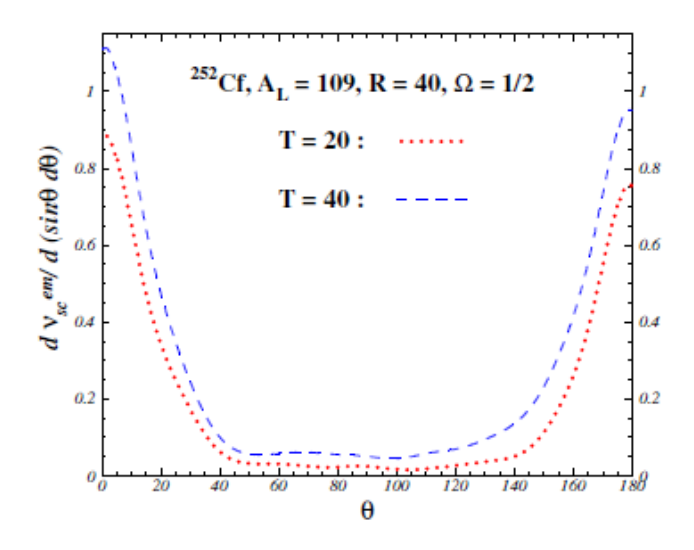


Fig.4. The angular distribution with respect to the fission axis calculated for SN, on a sphere of radius 40 fm, in the reaction 252 Cf(sf) for the most probable mass ratio (A_L =109). Jnly the subset of neutron states with Ω =1/2 was used. The time T is in units of 10^{-22} .

Important deviations from a smooth maxwellian spectrum are predicted as seen in the linear scale representation (the upper part of the figure). They look surprisingly the same and appear at the same energies as the wiggles in the measured spectrum from Figs. 2–3.

Although all SN are emitted by the same mechanism, their energies can be very different depending on the single-particle state they originate from. The average kinetic energies span a large interval from 1 MeV to more than 10 MeV with decreasing probabilities as in the PFN experimental spectrum.

A closer look at the high energy tail in the logarithmic scale representation of the spectrum shows the data lying between scission and evaporated neutrons. From this one could speculate that the scission neutron yield amounts to approximately half of PFN yield.

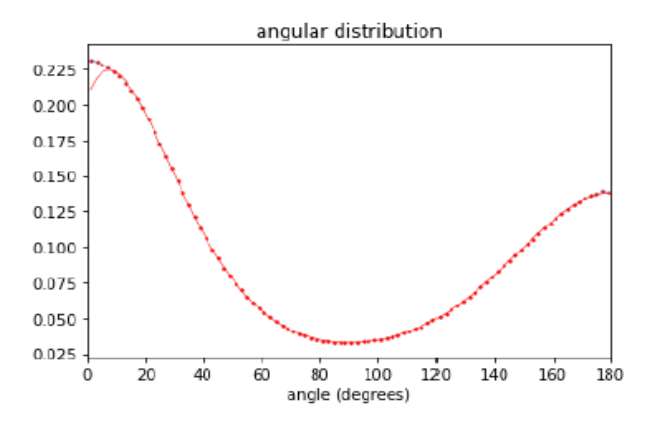
VI. $^{252}\mathrm{CF}$ ANGULAR DISTRIBUTION WITHOUT ANY SELECTION IN FRAGMENT MASS OR TKE

In the introduction, we said that inclusive data cannot reveal the PFN distributions in detail since such details are washed out when these distributions are averaged over all fission events. Now we will show that it is true only to a certain extent.

In the upper part of Fig. 6 is represented the measured angular distribution for all fragment masses and TKE's and its polynomial fit. The order of the polynomial (7) was chosen to lead to the minimum γ^2 per degree of freedom. The residual of the polynomial fit

(in the down part of Fig. 6) shows oscillations in the region from 20^0 to 160^0 . They are at 1% level but they are statistically significant.

Interestingly, even with a relatively high-order polynomial, we see oscillations. It says that there are always oscillations, even in the inclusive PFN data. They constitute reminiscences of the structures presented in Figs. 2–3, where measurements in coincidences with well defined fission fragments are displayed.



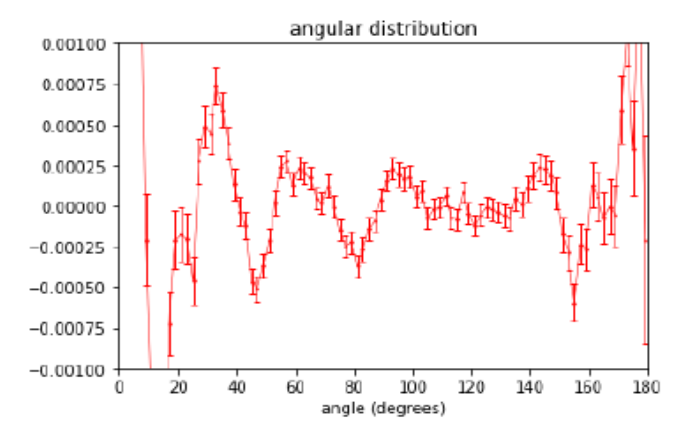


Fig.5. Inclusive PFN angular distribution and its polynomial fit (upper picture) and the residual of the polynomial fit (bottom picture).

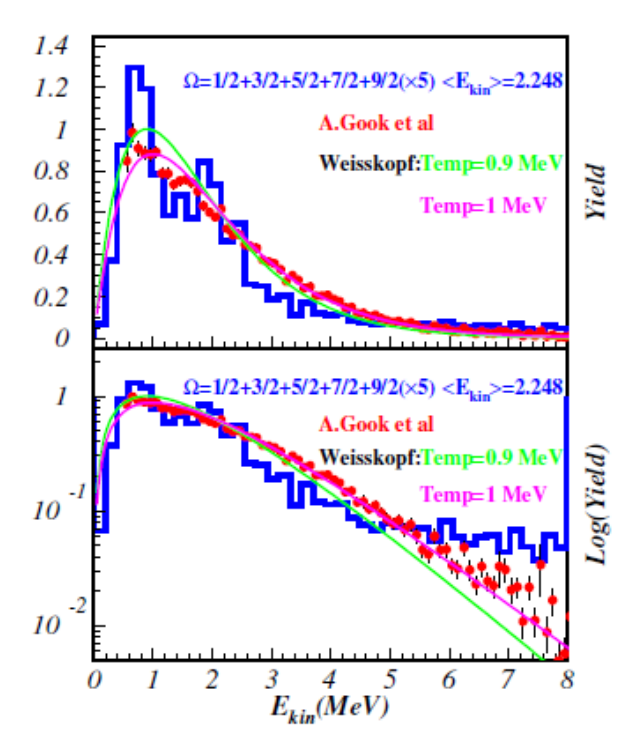


Fig.6. The calculated kinetic energy spectrum for the most probable mass division (defined by the light fragment mass A_L =96) (histogram), experimental data from the reaction 235 U(n,f) (points) and two typical evaporation spectra characterized by nuclear temperatures Temp= 1.0 and 0.9 MeV (lines); taken from [39].

VII. CONCLUSIONS AND FURTHER DEVELOPMENTS

We have found statistically significant structures in the angular and energy distributions of PFNs. These structures are not consistent with the notion that all PFNs are evaporated from the fragments long after the scission moment. Similar structures are found in calculations of the emission of scission neutrons. Still, we believe that more work is necessary in order to assess whether or not they have the same origin.

The amplitude of the predicted fluctuation is larger than those observed in our measured data since in our model calculations no mass resolution has been taken into account at this stage. In addition, in the lower part of Fig. 6 is shown that from the high-energy part of the PFN spectrum one may estimate that a considerable part of the emitted neutrons are evaporated from fully accelerated fragments. This estimate agrees with the result in Ref. [13] that, in ²⁴⁰Pu, SN multiplicity is about half of the total PFN multiplicity. Therefore both mass resolution and evaporated neutrons do lead to an attenuation of the observed structure.

One can, of course, not exclude that "finer corrections" to the traditional approach may eventually reproduce the fluctuations evident in the data but until then, the present results will continue to challenge the generally accepted evaporation hypothesis. Moreover, DSM explains the structure on its own, predicting the origin of a considerable fraction of observed neutrons closed to scission.

From the experimental perspective, several potential improvements and aspects may be considered. While it is possible to strive for better mass resolution, the current setup is already near the limit imposed by neutron emission on the 2E-technique. Because the two masses are determined from their measured energies using energy and momentum conservation, and since these are post-neutron energies they require recoil corrections, which leads to unavoidable contributions to the mass resolution. An improved mass resolution might be achieved by employing coincident measurements of the two fragment velocities, avoiding recoil correction. However, this would significantly reduce efficiency.

The current angular resolution, at approximately $9-10^0$ (FWHM), is constrained by the opening angle of the detectors. A potential improvement could bring the resolution closer to that of an ionization chamber 7^0 (FWHM) by increasing the distance between the detectors from 60 cm to 120 cm. This adjustment, however, would come with a loss in efficiency. Moving the detectors farther away would also benefit the neutron energy resolution. To further enhance the energy spectrum, the neutron detection threshold could be lowered by using alternative detector types.

Repeating the experiment for thermal neutron-induced fission of ²³⁵U or ²³⁹Pu would be advantageous. Large statistical accuracy could be obtained, because of the large thermal neutron cross-section, at facilities that can provide high thermal neutron flux. The lower average number of neutrons emitted in ²³⁵U(n,f) would also benefit the mass resolution that can be obtained with the 2E technique, since the recoil correction is smaller.

From the theoretical perspective, further calculations are needed, especially for $^{252}\text{Cf}(sf)$. Furthermore, further investigation of the approximations contained within the current DSM calculations is needed. Self-consistent calculations (e.g., [14]) should be extended to larger grids and longer times, in order to allow them to estimate scission neutrons angular distributions and spectra.

VIII. ACKNOWLEDGEMENTS

Work partially supported by Euratom research and training programme under grant agreement No 847594 (ARIEL). We are grateful to Patrick Talou for his constant interest in this work and pertinent discussions.

REFERENCES

- 1. H. Weigmann, in The Nuclear Fission Process, Ed. C. Wagemans (CRC Press, Boca Raton, USA, 1991), Ch. 4, p.63.
- Martin, J.-F., Taieb, J., Chatillon, A., Bèlier, G., Boutoux, G., Ebran, A., Gorbinet, T., Grente, L., Laurent, B., Pellereau, E., Alvarez-Pol, H., Audouin, L., Aumann, T., Ayyad, Y., Benlliure, J., Casarejos, E., Cortina Gil, D., Caamaño, M., Farget, F., Fernández-Domínguez, B., Heinz, A., Jurado, B., Kelić-Heil, A., Kurz, N., Nociforo, C., Paradela, C., Pietri, S., Ramos, D., Rodríguez-Sánchez, J.-L., Rodríguez-Tajes, C., Rossi, D., Schmidt, K.-H., Simon, H., Tassan-Got, L., Vargas, J., Voss, B., and Weick, H. The European Physical Journal A 51(12), 1–8 (2015).

- Chatillon, A., Taieb, J., Martin, J.-F., Pellereau, E., Boutoux, G., Gorbinet, T., Grente, L., Bèlier, G., Laurent, B., Alvarez-Pol, H., Ayyad, Y., Benlliure, J., Caamaño, M., Audouin, L., Casarejos, E., Cortina-Gil, D., Farget, F., Fernández Domínguez, B., Heinz, A., Jurado, B., Kelić-Heil, A., Kurz, N., Lindberg, S., Loeher, B., Nociforo, C., Paradela, C., Pietri, S., Ramos, D., Rodriguez-Sanchez, J.-L., Rodriguez-Tajes, C., Rossi, D., Schmidt, K.-H., Simon, H., Tassan-Got, L., Toernqvist, H., Vargas, J., Voss, B., Weick, B., and Yan, Y. EPJWeb of Conf. 111, 08001 (2016).
- Rodriguez-Tajes, C., Farget, F., Derkx, X., Caamaño, M., Delaune, O., Schmidt, K.-H., Clèment, E., Dijon, A., Heinz, A., Roger, T., Audouin, L., Benlliure, J., Casarejos, E., Cortina, D., Dorè, D., Fernández-Domínguez, B., Jacquot, B., Jurado, B., Navin, A., Paradela, C., Ramos, D., Romain, P., Salsac, M. D., and Schmitt, C. Phys. Rev. C 89, 024614 Feb (2014).
- Caamaño, M., Delaune, O., Farget, F., Derkx, X., Schmidt, K.-H., Audouin, L., Bacri, C.-O., Barreau, G., Benlliure, J., Casarejos, E., Chbihi, A., Fernández Domínguez, B., Gaudefroy, L., Golabek, C., Jurado, B., Lemasson, A., Navin, A., Rejmund, M., Roger, T., Shrivastava, A., and Schmitt, C. Phys. Rev. C 88, 024605 Aug (2013).
- Caamaño, M., Farget, F., Delaune, O., Schmidt, K.-H., Schmitt, C., Audouin, L., Bacri, C.-O., Benlliure, J., Casarejos, E., Derkx, X., Fernández-Domínguez, B., Gaudefroy, L., Golabek, C., Jurado, B., Lemasson, A., Ramos, D., Rodríguez-Tajes, C., Roger, T., and Shrivastava, A. Phys. Rev. C 92, 034606 Sep (2015).
- 7. N. Carjan, F.A. Ivanyuk, Yu. Oganessian, Nucl. Phys. A 968 (2017) 53-64.
- 8. G. Scamps, C. Simenel, Nature 564, 382 (2018).
- K. Mahata, C. Schmitt, Shilpi Gupta, A. Shrivastava, G. Scamps, K.-H. Schmidt, Phys. Lett. B 825, 136859 (2022).
- 10. G. Scamps, C. Simenel, Phys. Rev. C 100, 041602(R) (2019).
- 11. Wilson, J.N., Thisse, D., Lebois, M. et al. Angular momentum generation in nuclear fission. Nature 590, 566–570 (2021).
- 12. N. Carjan, M. Rizea, and P. Talou, EPJ Web Conf. 146, 04002 (2017).
- 13. N. Carjan, I. Stetcu, M. Rizea, A. Bulgac, EPJ Web Conf., 256 (2021) 00004.
- 14. I. Abdurrahman, M. Kafker, A. Bulgac, I. Stetcu, Phys. Rev. Lett. 132, 242501 (2024).
- 15. F. Bloch, H. Staub, U.S. Atomic Energy Commission Document AECD-3158, 1943.
- 16. R.R. Wilson, 1945, published in Phys. Rev. 77 (1947) 189.
- 17. J.S. Fraser, Phys. Rev. 88 (1952) 536.
- 18. J. Terrell, Phys. Rev. 113 (1959) 527.
- H.-H. Knitter, U. Brosa, C. Butz-Jorgensen, in The Nuclear Fission Process, Ed. C. Wagemans (CRC Press, Boca Raton, USA, 1991), Ch. 11, p.497.
- 20. M.B. Chadwick, Nucl. Technol. (2021) 207:S24-61.
- 21. M.B. Chadwick, R. Capote, Frontiers in Physics (2023) 11:1105593.
- 22. V.F. Weisskopf, Phys. Rev. 52 (1937) 295.
- 23. D.G. Madland, J. R. Nix, Nucl. Sci. Eng. 81 (1982) 213.
- 24. O. Litaize, O. Serot, Phys. Rev. C 82 (2010) 054616.
- 25. P. Talou et al., Phys. Rev. C 83 (2011) 064612.
- 26. K. Skarsvag, K. Bergheim, Nucl. Phys. 45 (1963) 72.
- A.S. Vorobyev, O.A. Scherbakov et al., Proceedings XVII International Seminar on Interaction of Neutrons with Nuclei, Dubna, May 27-29, 2009, p.60, Dubna 2010.
- 28. N. Carjan, M. Rizea, Phys. Lett. B 747 (2015) 178.
- 29. A. Göök, F.-J. Hambsch, M. Vidali, Phys. Rev. C90, 064611 (2014).

- 30. A. Göök, W. Geerts, F.-J. Hambsch, S. Oberstedt, M. Vidali, Sh. Zeynalov, Nucl. Instr. and Meth. A 830 (2016) 366.
- 31. A. Göök, F.-J.Hambsch, S. Oberstedt, M. Vidali, Phys. Rev. C 98 044615 (2018).
- 32. F. Gönnenwein, in The Nuclear Fission Process Ed. C. Wagemans (CRC Press, Boca Raton, USA, 1991), Ch. X, p.50.
- 33. Travar et al., Phys. Lett. B 817 (2021) 136293.
- 34. M.B. Chadwick et al., Nuclear Data Sheets 112 (2011) 2887.
- 35. R.W. Fuller, Phys. Rev. 126 (1962) 684.
- 36. I. Halpern, in First Symposium on Physics and Chemistry of Fission, Vol. II, IAEA, Vienna, 1965, p. 369.
- 37. N. Carjan, M. Rizea, Int. J. Mod. Phys. E 21 (2012) 1250031.
- 38. M. Rizea, N. Carjan, Nucl. Phys. A 909 (2013) 50.
- 39. N. Carjan, M. Rizea, Phys. Rev. C 99 (2019) 034613.
- 40. N. Carjan, M. Rizea, Int. J. Modern Phys. E 28 (2019) 1950103.
- 41. A. Göök, F.-J. Hambsch, and S. Oberstedt, EPJ Web Conf. 16, 00004 (2018).
- 42. J.M. Blatt and V.F. Weisskopf, Theoretical Nuclear Physics (John Wiley, New York, 1958), p. 368.

Upgrade plan of intra-nuclear cascade model for ADS simulation studies

Rong Wang^{1,2,*}, Han Zhang^{1,2}, Han-Jie Cai^{1,2}, Xun-Chao Zhang^{1,2}, Huan Jia^{1,2}, and Yuan He^{1,2}

¹Institute of Modern Physics, Chinese Academy of Sciences, Lanzhou 730000, China ²School of Nuclear Science and Technology, University of Chinese Academy of Sciences, Beijing 100049, China

*rwang@impcas.ac.cn

In this paper, we evaluate the intra-nuclear cascade model through double differential cross sections and propose the ideas for further improvements. High-energy nuclear reaction models are vital for ADS studies, as existing nuclear data are insufficient for describing reactions above approximately 30 MeV. Systematic deviations are identified between intra-nuclear cascade model predictions and experimental data in terms of the differential cross sections for nuclear spallation reactions across various nuclear targets. The observed minor deviations at high energies may originate from the unaccounted contributions of the scatterings on nucleon-nucleon short-range correlations. The neutron efficiency for an ADS burner depends on the neutron energy, and the emitted particle energy spectra, encoded in differential cross sections, are crucial for accurate simulation studies of ADS systems. Future plan is discussed for improving the model descriptions of double differential cross sections in medium-to-high energy region, which is expected to enhance the accuracy of our full-energy range particle transport Monte Carlo simulation software for ADS research and design.

I. MOTIVATIONS OF HIGH-ENERGY NUCLEAR REACTION MODELS FOR ADS

The Accelerator-driven sub-critical nuclear reactor system (ADS) is an efficient approach to generating sustainable nuclear fission energy for the future. It simultaneously manages the nuclear waste problem while utilizing depleted uranium for electricity production [1, 2]. Scientists in China are currently building an experimental facility in Huizhou, Guangdong province, for ADS principle validation and research [3]. To advance the understanding of sub-critical reactors and develop an efficient nuclear waste transmutation method, careful and accurate Monte Carlo (MC) simulations are essential. For ADS research and future operation, simulation software is a powerful tool, providing a guidance for estimating beam requirements to achieve the targeted reactor power.

Developing an effective ADS simulation software requires precise descriptions of various nuclear reactions. However, evaluated nuclear reaction data at energies above 30 MeV are scarce [4–7], and the accuracy of neutron-induced fission cross-sections and inelastic processes is severely inadequate. Independent fission yield data are critically lacking or imprecise. Moreover, above incident energies of ~ 200 MeV, the complexity of open channels increases significantly for nuclear databases.

Owing to the lack of nuclear data, reaction models are indispensable at high energies to fully describe particle interaction and transport within ADS MC software. In the mediumto-high energy range, particle evaporation, induced fission [8–10], and intra-nuclear cascade (INC) collisions [11–13] dominate. Particle evaporation and nuclear fission primarily govern

slow and low-energy particle emissions, whereas the intra-nuclear cascade process dominates prompt and high-energy particle emissions.

Our current ADS simulation studies reveal that the external source efficiency of highenergy neutrons for driving nuclear transmutation exceeds that of low-energy neutrons a lot. Therefore, accurate descriptions of high-energy nuclear reactions and the high-energy neutron spectrum are critical for ADS simulations. Another key finding is that different MC simulation software, or even different versions of the same software, exhibit substantial discrepancies (exceeding 10%) in predicting high-energy neutron flux.

Given these factors, this study primarily focuses on high-energy neutron emissions and the underlying INC model for spallation processes, as the initial step of model improvement for our ADS software development. In Sec. II, we briefly review the Li`ege Intra-Nuclear Cascade (INCL) model [11–13], used in our ADS simulations for high-energy nuclear reaction description. In Sec. III, we highlight minor deviations observed between model predictions and experimental data in the high-energy neutron spectrum, regarding double differential cross sections. In Sec. IV, we outline our future plans for improving model descriptions of emission nucleon energy spectrum. Finally, a concise summary is provided in Sec. V.

II. INTRA-NUCLEAR CASCADE MODEL

Nuclear reactions in the medium-to-high energy region proceed through two stages: the first stage is dominated by hard nucleon-nucleon collisions and emits fast particles, followed by the de-excitation process of a partially thermalized nuclear remnant (evaporation, fission, multi-fragmentation, etc.). Consequently, common MC simulation tools for describing these reactions result from the coupling an intra-nuclear cascade model for the first stage to an statistical evaporation-fission model for the second stage. The INCL model, refined over nearly four decades, has demonstrated strong predictive power in describing a wide range of experimental observations. These include total reaction cross sections, differential cross sections, neutron multiplicity, and residue mass distributions for nucleon-, pion-, and light ion-induced nuclear reactions from approximately 200 MeV to 15 GeV [11–18]. Recent INCL developments focus on extending its scope to higher energies by incorporating more degrees of freedom for cascade collisions, such as K, η , and ω mesons, Λ and Σ baryons, and multiplion production process [16–18].

The INCL model is a semi-classical model in which an avalanche of independent binary collisions is initiated by a high-energy projectile [11–13]. Initially, nucleons in the target are assigned the random positions and momenta based on realistic nuclear density distributions in phase space. The incident particle is positioned near the target surface with a random impact parameter. All nucleons then propagate within the mean-field nuclear potential well, traveling along straight-line trajectories until two particles trigger a scattering event, or until a particle encounters the nuclear surface. Scattering occurs if the relative distance is less than the square root of the total cross section between the particles. At the nuclear surface, nucleons may be transmitted or reflected with defined probabilities. A key feature of the INCL model is its self-consistent determination of the cascade stopping time – defined as the time point when the remnant nucleus shows signs of thermalization and the cascade stage gives way to the de-excitation stage [11–13]. Other features of INCL include the realistic target density distributions and minimal free parameters.

Rather than using a quantum molecular dynamics model [19, 20] or the Boltzmann-Uehling-Uhlenbeck model [21, 22], we employ the INCL model in our ADS simulation

software for describing high-energy nuclear reactions. This choice stems from INCL's significantly faster computational speed compared to the quantum models. Although INCL operates within a semi-classical framework, it incorporates key quantum aspects, such as Pauli blocking in collisions, quantum mechanical transmission at the nuclear surface, and a smoothly varying nuclear mean field. This integration likely explains INCL's ability to accurately describe certain reaction channels even at energies as low as a few tens of MeV. Note that the INCL model is coupled to the ABLA de-excitation model when necessary. The ABLA model accounts for statistical nucleon emission, gamma emission, fission, and multifragmentation processes.

III. MINOR DEVIATIONS BETWEEN MODEL AND EXPERIMENT FOR DIFFERENTIAL CROSS SECTIONS

Although the INCL model generally describes high-energy nuclear reactions well, this section details our verification of the model for neutron emission processes induced by projectiles with energies above 200 MeV. Via careful model evaluations, we aim to understand the remaining minor systematic uncertainties within the model and look for potential optimizations and upgrades. Our focus is on the details of neutron energy spectra across the whole range.

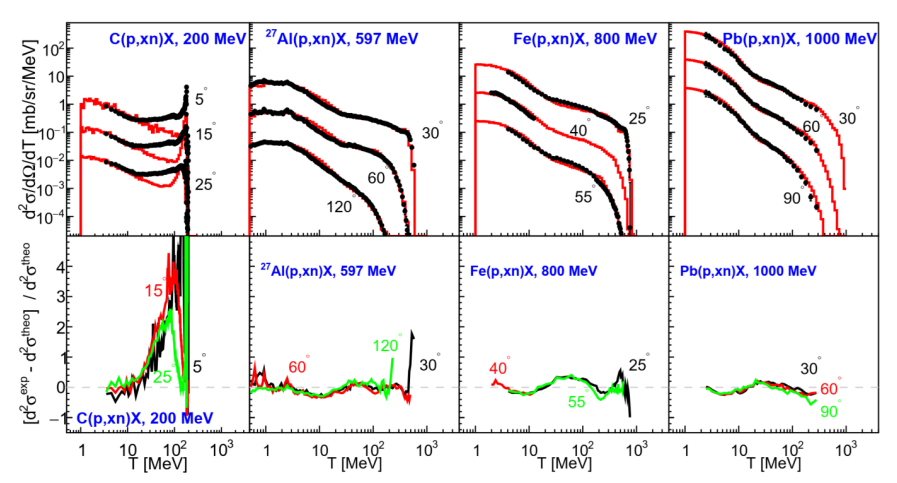


FIG. 1. The top panels show the comparisons of double differential cross sections $d^2\sigma/d\Omega/dT$ between the experimental data [23–26] and the INCL model predictions, for carbon, aluminum, iron and lead targets, at incident energies from 200 MeV to 1000 MeV; The bottom panels show accordingly the relative deviations between the experimental measurements and the INCL model predictions. The reaction channels and incident energies are labeled in each panel.

Figure 1 compares the INCL model predictions of double differential cross sections $d^2\sigma/d\Omega/dT$ as a function of emitted neutron kinetic energy T against the experimental data, for carbon, aluminum, iron, and lead targets at incident energies from 200 MeV to 1000 MeV

[23–26]. The relative deviations between experimental measurements and INCL predictions are also presented. Figure 2 similarly presents the double differential cross sections and relative deviations (experiment relative to model) at higher incident energies (1200 MeV to 3000 MeV) [26–28].

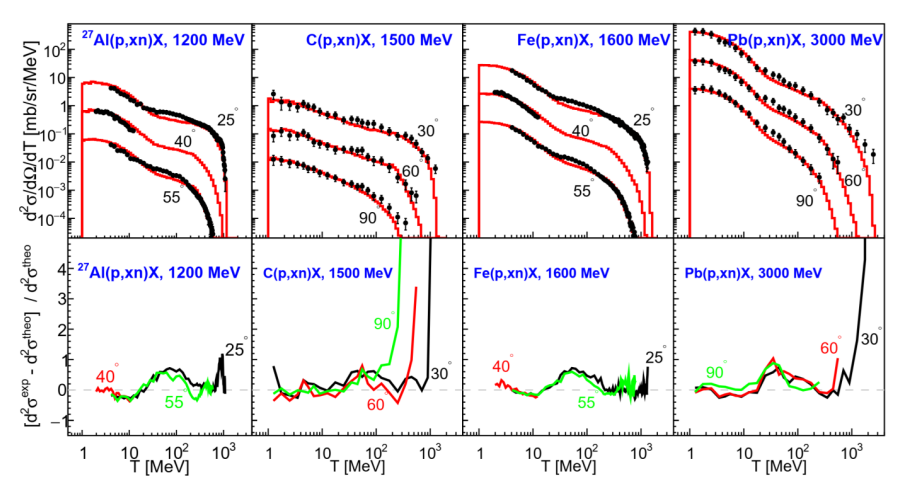


FIG. 2. The top panels show the comparisons of double differential cross sections $d^2\sigma/d\Omega/dT$ between the experimental data [26–28] and the INCL model predictions, for carbon, aluminum, iron and lead targets, at incident energies from 1200 MeV to 3000 MeV; The bottom panels show accordingly the relative deviations between the experimental measurements and the INCL model predictions. The reaction channels and incident energies are labeled in each panel.

Figures 1 and 2 reveal consistent systematic deviations between model and data [23–28]. Experimental differential cross sections exceed INCL predictions at emission energies T around 100 MeV, while falling slightly below model predictions around 10 MeV. For some data sets, a rapid increase in relative deviation occurs near the quasi-elastic peak. Although the absolute deviation is small at the high-energy tail, the near-zero value of cross section at the tail results in the large relative deviations. Additionally, fluctuations in the relative deviation at high-energy tail may stem from the experimental energy resolution limitations, which tend to increase the differential cross section around the maximum emission energy.

Figure 3 compares the INCL predictions of $d^2\sigma/d\Omega/dT$ versus emitted neutron kinetic energy T with the experimental data for W(16 O, xn)X) and Pb(16 O, xn)X) reactions at 400 MeV/u [29]. Relative deviations between model and data are also present in the figure. These 16 O-induced spallation data were measured at the Heavy Ion Research Facility in Lanzhou (HIRFL), operated by Institute of Modern Physics, Chinese Academy of Sciences. Interestingly, the deviation patterns between model and data for light-ion-induced spallation reactions resemble those for proton-induced reactions. A prominent feature is that the experimental differential cross sections exceed the INCL predictions in the emission energy region from \sim 20 MeV to \sim 200 MeV.

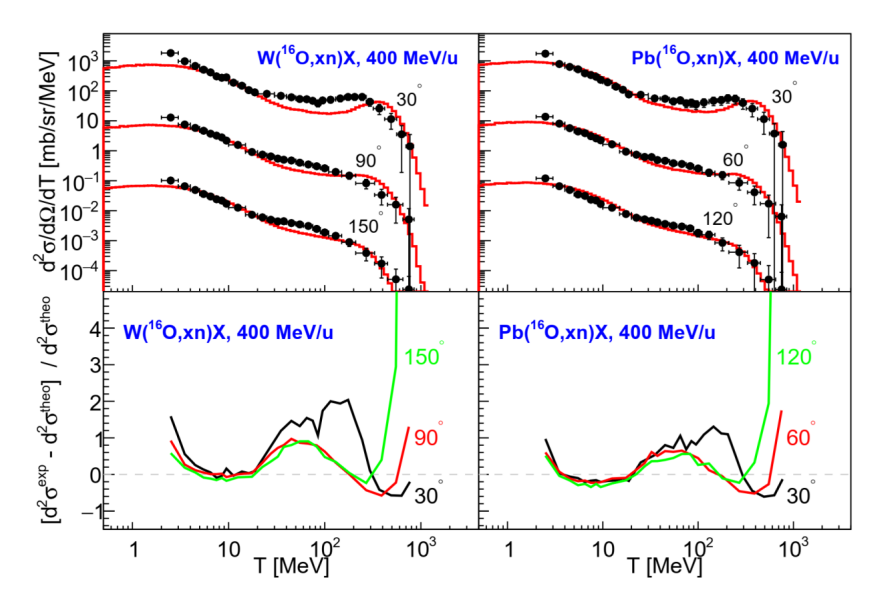


FIG. 3. The top panels show the comparisons of double differential cross sections $d^2\sigma/d\Omega/dT$ between the experimental data [29] and the INCL model predictions, for tungsten and lead targets; The incident particle is the light ion 16O with the kinematic energy of 400 MeV/u; The bottom panels show accordingly the relative deviations between the experimental measurements and the INCL model predictions. The reaction channels and incident energies are labeled in each panel.

Figure 4 compares the INCL predictions of $d^2\sigma/d\Omega/dT$ versus T with experimental data [24, 30], for proton-induced spallation on a depleted uranium target at incident energy around 600 MeV. Results from two independent experimental groups are shown. Notably, this similar deviation pattern appears in only one data set, while the other data agrees well with INCL predictions. The discrepancy between the two experimental measurements is noteworthy. We observe differences in the uranium target thickness and neutron-photon separation methods used between the two experiments. Further experimental measurements are needed to investigate this inconsistency.

The following section explains the likely cause of this consistent deviation pattern in the emitted neutron energy spectrum and proposes a plan to address it.

IV. PLAN FOR FUTURE IMPROVEMENTS OF INTRA-NUCLEAR CASCADE MODEL

Analysis in the previous section reveals a universal deviation pattern between model predictions and experimental data across different nuclear targets at high incident energies. This suggests the deviation may originate from a fundamental nuclear structure not yet incorporated in the INCL model. Reviewing recent high-energy nuclear experiments, we note nucleon-nucleon short-range correlations (NN SRC) – a universal microscopic dynamical

structure beyond the mean-field description – have been identified in numerous experiments over the past two decades [31–40].

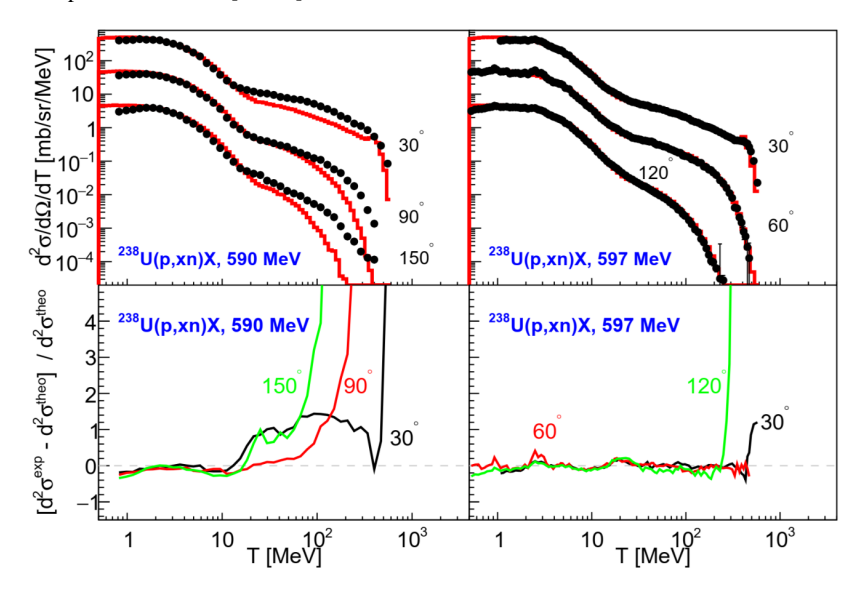


FIG. 4. The top panels show the comparisons of double differential cross sections $d^2\sigma/d\Omega/dT$ between the experimental data [24, 30] and the INCL model predictions, for depleted Uranium target at energies of 590 and 597 MeV; The bottom panels show accordingly the relative deviations between the experimental measurements and the INCL model predictions. The reaction channels and incident energies are labeled in each panel.

NN SRC refers to short-lived high-density configuration driven by intermediate- and short-range nuclear forces. Its primary features are: a short distance (< 1 fm, approaching the repulsive core) between the correlated nucleons in coordinate space, a high relative momentum (> k_F) in momentum space [41–46]. Experimental evidence for NN SRC comes mainly from exclusive and inclusive measurements. In exclusive processes, high-energy projectiles strike NN SRC and produce two back-to-back high-momentum nucleons [31–36]. In inclusive electron scattering, the scaling in the Bjorken variable $x_B \sim 2$ region signals the universal and short-distance structure of NN SRC probed by the high-momentum electron [37–40]. NN SRC is now a well-established cluster structure beyond the independent nucleons, exhibiting more or less universal properties across different nuclear targets.

Striking one nucleon within an NN SRC pair with a high-energy projectile causes the correlated partner nucleon to recoil at high energy due to the short-distance nuclear force within SRC. One recent measurement [36] indicates the mean emission momentum of the recoiling partner is ~ 500 MeV/c, corresponding to ~ 125 MeV kinetic energy. Significantly, the INCL model predictions underestimate the experimental neutron yields around 100 MeV. Incorporating these recoiling SRC partner neutrons would undoubtedly reduce the model-data

deviation. Furthermore, energy conservation implies that the increased high-energy neutron production ($\sim 100~\text{MeV}$) reduces the low-energy neutron yields ($\sim 10~\text{MeV}$) during the intranuclear cascade collision stage.

Our objective is to enhance ADS simulation software accuracy, providing a reliable tool for ADS design and research. Based on the above analysis, to mitigate deviations between nuclear reaction models and data, we plan to implement NN SRC pairs within the INC model.

V. SUMMARY

Validation studies of INCL model regarding double differential cross sections have revealed minor, yet universal, deviations from the experimental data. The recent precise data measured at HIRFL, Lanzhou, China [29] are also taken for evaluating the INCL model. One finds that INCL model under-predicts emitted neutron yields around 100 MeV compared to experiments.

We propose that the observed spectrum deviation can be resolved by accounting for the scattering on NN SRC pairs. Although NN SRC pairs are far less numerous than independent nucleons, their existence is firmly established by many high-energy experiments. Our qualitative analysis indicates the mean recoil energy of SRC partner nucleons (~ 125 MeV) closely matches the cross section deficit observed in INCL calculations around 100 MeV. Hence, one of our plans for improving the nuclear reaction model is implementing the NN SRC in the INC model. Additional upgrade plans include implementing many-body quantum correlations and nuclear medium effects to enhance INC model descriptions in low-energy region. These upgrades will significantly advance our in-development ADS MC simulation software.

ACKNOWLEDGMENTS

We thank Dr. Davide Mancusi and Dr. Jean-Christophe David for providing us with the source code of the INCL++ model. This research was supported by Large Research Infrastructures - China initiative Accelerator Driven System (Grant NO. 2017-000052-75-01-000590).

References

- 1. S. Andriamonje et al., Phys. Lett. B 348, 697 (1995).
- 2. H. Arnould et al., Phys. Lett. B 458, 167 (1999).
- 3. Y. He, H. Jia, H.-J. Cai, Z. Wang, W. Dou, J. Wu, Y. Chen, G. Huang, C. Y. J. Wong, and H. Zhao, JACoW IPAC2023, FRYG2 (2023).
- Ge, Zhigang, Xu, Ruirui, Wu, Haicheng, Zhang, Yue, Chen, Guochang, Jin, Yongli, Shu, Nengchuan, Chen, Yongjing, Tao, Xi, Tian, Yuan, Liu, Ping, Qian, Jing, Wang, Jimin, Zhang, Huanyu, Liu, Lile, and Huang, Xiaolong, EPJ Web Conf. 239, 09001 (2020).
- 5. D.A. Brown et al., Nucl. Data Sheets 148, 1 (2018).
- A.J. Koning, D. Rochman, J.C. Sublet, N. Dzysiuk, M. Fleming, and S. van der Marck, Nucl. Data Sheets 155, 1 (2019).
- 7. O. Iwamoto et al., J. Nucl. Sci. Tech. 60, 1 (2023).

- A. Kelic, M.V. Ricciardi, and K.-H. Schmidt, in Joint ICTP-IAEA Advanced Workshop on Model Codes for Spallation Reactions (2009) arXiv:0906.4193 [nucl-th].
- D. Mancusi, R.J. Charity, and J. Cugnon, Phys. Rev. C 82, 044610 (2010), arXiv:1007.0963 [nucl-th].
- N. Buyukcizmeci, R. Ogul, and A. S. Botvina, Eur. Phys. J. A 25, 57 (2005), arXiv:nucl-th/0506017.
- 11. A. Boudard, J. Cugnon, S. Leray, and C. Volant, Phys. Rev. C 66, 044615 (2002).
- 12. A. Boudard, J. Cugnon, J.-C. David, S. Leray, and D. Mancusi, Phys. Rev. C 87, 014606 (2013), arXiv:1210.3498 [nucl-th].
- D. Mancusi, A. Boudard, J. Cugnon, J.-C. David, P. Kaitaniemi, and S. Leray, Phys. Rev. C 90, 054602 (2014), arXiv:1407.7755 [nucl-th].
- 14. J. Cugnon, Nucl. Phys. A 462, 751 (1987).
- 15. J. Cugnon, C. Volant, and S. Vuillier, Nucl. Phys. A 620, 475 (1997).
- 16. S. Pedoux and J. Cugnon, Nucl. Phys. A 866, 16 (2011).
- 17. J.C. David, A. Boudard, J. Cugnon, J. Hirtz, S. Leray, D. Mancusi, and J. L. Rodriguez-Sanchez, Eur. Phys. J. Plus 133, 253 (2018), arXiv:1802.04731 [nucl-ex].
- J. Hirtz, J. C. David, A. Boudard, J. Cugnon, S. Leray, I. Leya, J.L. Rodr'iguez-S'anchez, and G. Schnabel, Phys. Rev. C 101, 014608 (2020), arXiv:1909.02246 [nucl-th].
- 19. S.A. Bass et al., Prog. Part. Nucl. Phys. 41, 255 (1998), arXiv:nucl-th/9803035.
- 20. Z.-Q. Feng and G.-M. Jin, Phys. Rev. C 80, 037601(2009), arXiv:0909.1089 [nucl-th].
- O. Buss, T. Gaitanos, K. Gallmeister, H. van Hees, M. Kaskulov, O. Lalakulich, A. B. Larionov, T. Leitner, J. Weil, and U. Mosel, Phys. Rept. 512, 1 (2012), arXiv:1106.1344 [hep-ph].
- 22. B. Li, A. T. Sustich, B. Zhang, and C.M. Ko, Int. J. Mod. Phys. E 10, 267 (2001).
- 23. Y. Iwamoto, M. Hagiwara, T. Matsumoto, A. Masuda, H. Iwase, H. Yashima, T. Shima, A. Tamii, and T. Nakamura, Nuclear Instruments and Methods in Physics Research Section A: Accelerators, Spectrometers, Detectors and Associated Equipment 690, 10 (2012).
- W.B. Amian, R.C. Byrd, D.A. Clark, C.A. Goulding, M.M. Meier, G.L. Morgan, and C.E. Moss, Nucl. Sci. Eng. 115, 1 (1993).
- 25. Y.V. Trebukhovsky et al., Phys. Atom. Nucl. 68, 3 (2005).
- 26. S. Leray et al., Phys. Rev. C 65, 044621 (2002), arXiv:nucl-ex/0112003.
- 27. K. Ishibashi et al., J. Nucl. Sci. Technol. 34, 529 (1997).
- T. Nakamoto, K. Ishibashi, N. Matsufuji, N. Shigyo, K. Maehata, S. Ichirou Meigo, H. Takada, S. Chiba, M. Numajiri, T. Nakamura, and Y. Watanabe, Journal of Nuclear Science and Technology 32, 827 (1995), https://doi.org/10.1080/18811248.1995.9731784.
- 29. T.G. S. F. Chen Zhi Qiang, Han Rui, Scientia Sinica, Physica, Mechanica Astronomica 50, 052007 (2020).
- S. Cierjacks, Y. Hino, S.D. Howe, F. Raupp, and L. Buth, in Nuclear Data for Science and Technology, edited by K. H. B"ockhoff (Springer Netherlands, Dordrecht, (1983) pp. 383–386.
- 31. A. Tang et al., Phys. Rev. Lett. 90, 042301 (2003), arXiv:nucl-ex/0206003.
- 32. E. Piasetzky, M. Sargsian, L. Frankfurt, M. Strikman, and J.W. Watson, Phys. Rev. Lett. 97, 162504 (2006), arXiv:nucl-th/0604012.
- 33. R. Subedi et al., Science 320, 1476 (2008), arXiv:0908.1514 [nucl-ex].

- 34. M. Duer et al. (CLAS), Nature 560, 617 (2018).
- M. Duer et al. (CLAS), Phys. Rev. Lett. 122, 172502(2019), arXiv:1810.05343 [nuclex].
- 36. A. Schmidt et al. (CLAS), Nature 578, 540 (2020), arXiv:2004.11221 [nucl-ex].
- 37. K.S. Egiyan et al. (CLAS), Phys. Rev. Lett. 96, 082501 (2006), arXiv:nucl-ex/0508026.
- 38. N. Fomin et al., Phys. Rev. Lett. 108, 092502 (2012), arXiv:1107.3583 [nucl-ex].
- 39. B. Schmookler et al. (CLAS), Nature 566, 354 (2019), arXiv:2004.12065 [nucl-ex].
- 40. S. Li et al., Nature 609, 41 (2022), arXiv:2210.04189 [nucl-ex].
- 41. L.L. Frankfurt and M. I. Strikman, Phys. Rept. 160, 235 (1988).
- 42. M.M. Sargsian, T.V. Abrahamyan, M.I. Strikman, and L.L. Frankfurt, Phys. Rev. C 71, 044615 (2005), arXiv:nucl-th/0501018.
- 43. O. Hen, G.A. Miller, E. Piasetzky, and L.B. Weinstein, Rev. Mod. Phys. 89, 045002 (2017), arXiv:1611.09748 [nucl-ex].
- 44. J. Arrington, D.W. Higinbotham, G. Rosner, and M. Sargsian, Prog. Part. Nucl. Phys. 67, 898 (2012), arXiv:1104.1196 [nucl-ex].
- 45. N. Fomin, D. Higinbotham, M. Sargsian, and P. Solvignon, Ann. Rev. Nucl. Part. Sci. 67, 129 (2017), arXiv:1708.08581 [nucl-th].
- J. Arrington, N. Fomin, and A. Schmidt, Ann. Rev. Nucl. Part. Sci. 72, 307 (2022), arXiv:2203.02608 [nucl-ex].

Научное издание

FUNDAMENTAL INTERACTIONS & NEUTRONS, NUCLEAR STRUCTURE, ULTRACOLD NEUTRONS, RELATED TOPICS

XXXI International Seminar on Interaction of Neutrons with Nuclei

Proceedings of the Seminar

ФУНДАМЕНТАЛЬНЫЕ ВЗАИМОДЕЙСТВИЯ И НЕЙТРОНЫ, СТРУКТУРА ЯДРА, УЛЬТРАХОЛОДНЫЕ НЕЙТРОНЫ, СВЯЗАННЫЕ ТЕМЫ

ХХХІ Международный семинар по взаимодействию нейтронов с ядрами

Труды семинара

Ответственная за подготовку сборника к печати Л. В. Мицына.

Сборник отпечатан с файла, предоставленного оргкомитетом.

E3-2025-52

Подписано в печать 16.10.2025 Формат 60×90/16. Бумага офсетная. Печать цифровая Усл. печ. л. 9,27. Уч.-изд. л. 5,88. Тираж 50 экз. Заказ № 61178

Издательский отдел Объединенного института ядерных исследований 141980, г. Дубна, Московская обл., ул. Жолио-Кюри, 6. E-mail: publish@jinr.ru www.jinr.ru/publish/